

***PHOTON FACTORY
ACTIVITY REPORT***

1984/85

3

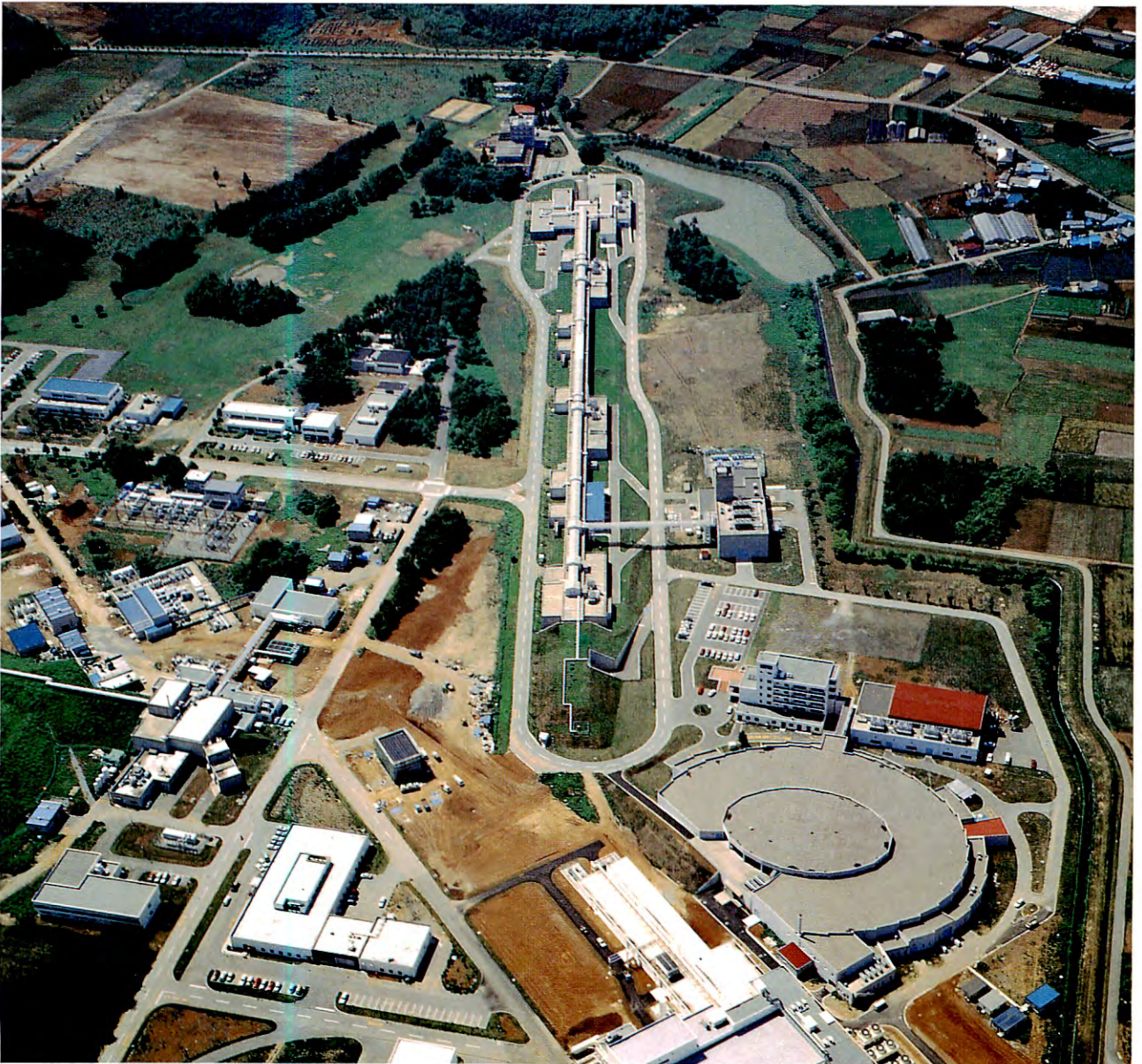


NATIONAL LABORATORY FOR HIGH ENERGY PHYSICS, KEK

PHOTON FACTORY

ACTIVITY REPORT

1984/85



Editorial Board

ANAMI Shozo

KITAMURA Hideo

KAMIYA Yukihide

NAKAJIMA Tetsuo*

(*Chief editor)

KEK Progress Report 85-1

©National Laboratory for High Energy Physics, 1986

KEK Reports are available from

Technical Information Office

National Laboratory for High Energy Physics

Oho-machi, Tsukuba-gun

Ibaraki-Ken, 305

JAPAN

Phone: 0298-64-1171

Telex: 3652-534 (Domestic)

(0) 3652-534 (International)

Cable: KEKOH0

You can jump to the article by clicking its title.

Table of Contents

	<u>page</u>	<u>serial page number</u>
I. Preface	I-1	1
II. Organization and Operation		
1. Organization	II-1	3
2. Operation	II-3	5
III. Injector Linac Division		
1. Introduction	III-1	9
2. Electron Linac		
2.1 Operational status of microwave source	III-2	10
2.2 Beam characteristics and measurements	III-3	11
2.3 Development	III-4	12
3. Positron Generator		
3.1 Injection system	III-11	19
3.2 Beam transport system	III-12	20
3.3 Accelerator guides	III-16	24
3.4 Microwave source	III-17	25
3.5 Control	III-18	26
3.6 Test operation	III-19	27
IV. Light Source Division		
1. Introduction	IV-1	31
2. Storage Ring		
2.1 General	IV-1	31
2.2 Measurement of betatron functions	IV-3	33
2.3 Beam instabilities	IV-5	35
2.4 Improvements of vacuum system	IV-9	39
2.5 Abnormal pressure rise at the rf cavity station	IV-12	42
2.6 Control	VI-13	43
2.7 Beam monitor in the storage ring	IV-16	46
2.8 Superconducting vertical wiggler	IV-19	49
2.9 Beam channel	IV-20	50
V. Instrumentation Division		
1. Beam Lines	V-1	57
2. Optics	V-7	63
3. Summary of X-ray Beam Lines and Optics	V-10	66
4. Characteristics of Soft X-ray and VUV Beam Lines and Optics	V-11	67
5. List of Apparatuses	V-14	70
VI. Users' Short Reports		
Contents	VI-1	73
Reports	VI-13	85
Author Index	VI-195	267
VII. List of New Experimental Proposals		
1. Proposals Accepted by Program Assessment Committee	VII-1	275
2. Proposals Accepted for Charged Beam Time Assessment	VII-11	285
VIII. List of Published Papers		
Published Papers in 1984	VIII-1	287
Published Papers in 1985	VIII-2	288

I. PREFACE

This volume covers the third-year activities of the Photon Factory, as it was opened as a national synchrotron radiation facility producing abundant photons from ultraviolet through hard x-rays. The number of users from all over the universities and governmental institutes already overflowed from our computer memory limit of 1000 registrations at the end of 1984, and about 250 experiments proposed are being carried out in 1985. Such busy programs of experiment have been neatly performed with stable machine operation achieved by the accelerator crew.

The total operation time limited by the budget of FY 1985 was 2600 hrs, increasing by 400 hrs from that of the previous fiscal year. This increase led to accelerator operation in a two-week mode; the storage ring is operated continuously for 240 hrs per two weeks from Wednesday morning through Saturday morning of the next week. About two thirds of the operation hours were devoted to users' experiments, and the rest was spent for tune-up of the machine and accelerator studies.

The linear accelerator, serving as the injector of the Photon Factory Ring and 6 GeV Accumulation Ring of TRISTAN, has been operated more stably by improving the whole system including assembly of the high power klystrons.

Positrons are essential to the colliding beam facility, TRISTAN. They are also benefit to the Photon Factory; positron beams do not trap positive ions or positively charged fine particles as do electron beams, and a good beam stability of the ring can be achieved by positron storage. For these purposes, the final assembling of the positron linac was completed by the end of March, and the first positron beam with a current of 2.3 mA was successfully accelerated to the energy of 250 MeV. Acceleration up to the energy of 2.5 GeV and test operation of the PF Storage Ring with positrons is scheduled at the end of 1985.

The light source, 2.5 GeV electron storage ring has been running stably through the year without any significant accidents. A very nice record was established that the operation time consumed by machine failure was only 0.7 % of the total. Various types of instabilities were overcome, and a beam life time as long as 13 hrs at a storage current of 150 mA was achieved even with operation of the vertical wiggler at a field strength of 5 T. As the next stage of development, efforts have been made to increase the stored current, and the ring was operated successfully at 450 mA with a beam lifetime of 200 minutes when the electron energy was 2.05 GeV.

Various experiments as reported in this volume were carried out in the 25 stations on the 9 beam lines. The wiggler was opened for general users from the fall run 1984 in operation compatible with experiments at the rest of beam lines. Operation time of the wiggler amounted to 61 % of the total time of the ring operation. The wiggler beam line has been very busy,

throughout the year, with experiments of X-ray topography, structure analysis under high-pressure ambience (2×10^5 atmospheres), angiography, and protein crystallography. The 120-pole permanent magnet undulator was also powerful in trace impurity analysis of light elements, X-ray microscopy, atomic and molecular photoionization. All these experiments have demonstrated importance of insertion devices.

Participation from industry is enhanced in 1985. During FY 1984, 1125 station-hours in total were devoted to 36 experiments for the following items; 2 for lithography, 2 for photo-reaction crystal growth, 5 for crystalline imperfection, 6 for impurity analysis, 13 for catalysis and amorphous materials by EXAFS, and 8 for miscellaneous. In FY 1985, 22 applications have been received by the end of October and the sum total amounted to 1059 station-hours.

The joint research programs between KEK and industry were also enlarged; 5 programs were executed in 1984. Now, 8 programs are running on various subjects such as characterization of semiconductor crystals and devices. KEK's partners are Nippon Electric, Hitachi, Mitsubishi, Fujitsu, Toshiba, Sanyo, and so on.

The experiment in the PF started with 8 beam lines having branch lines since it was opened to users. Now, new beam lines, BL-7, BL-8, and BL-27 have been constructed in collaboration with the Research Centre for Spectro-Chemistry of Faculty of Science, University of Tokyo, Hitachi Works' group, and KEK/HITACHI joint research group for development and evaluation of optical elements, respectively. Four beam lines are under construction; BL-6 and BL-16 by KEK, BL-9 and BL-17 by Nippon Electric and Fujitsu, respectively. In FY 1986, two beamlines, BL-5 and BL-19, are expected to be approved for KEK. The Photon Factory ring has 28 bending magnets and 24 of them are ready for extracting radiation. Now, 18 beam ports will be occupied at the end of FY 1986.

The third annual users' meeting was held with 250 participants in November 1985. 133 papers were presented in the Poster Sessions. Future plan such as improvement in emittance was the subject of hot discussion.

To keep close communication between the in-house staff and users, the journal "Photon Factory News" has been published five times a year with about 40 pages for each issue.

We would like to acknowledge kind cooperation of visitors from outstanding laboratories abroad. They are Dr. Alastair MacDowell from Daresbury Laboratory, and Prof. H. Winick from SSRL. Their interactions with our staff were very beneficial and fruitful.

On behalf of all the PF staff members and users, I would record here our warmest acknowledgements to Prof. Sasaki, the former director, for his great contributions to the Photon Factory. Professor Sasaki recognized importance of synchrotron radiation very early and built a UV

ring in the Institute of Nuclear Study in 1974. This is one of the oldest dedicated machines in the world to my best knowledge. He joined the PF in 1980 and continued his enthusiastic endeavour

to bring the PF to completion until his retirement at the end of March, 1985. Our activities today are owing to his outstanding leadership.

A handwritten signature in black ink that reads "Junichi Chikawa". The script is fluid and cursive, with the first letters of "Junichi" and "Chikawa" being capitalized and prominent.

Jun-ichi Chikawa
Director

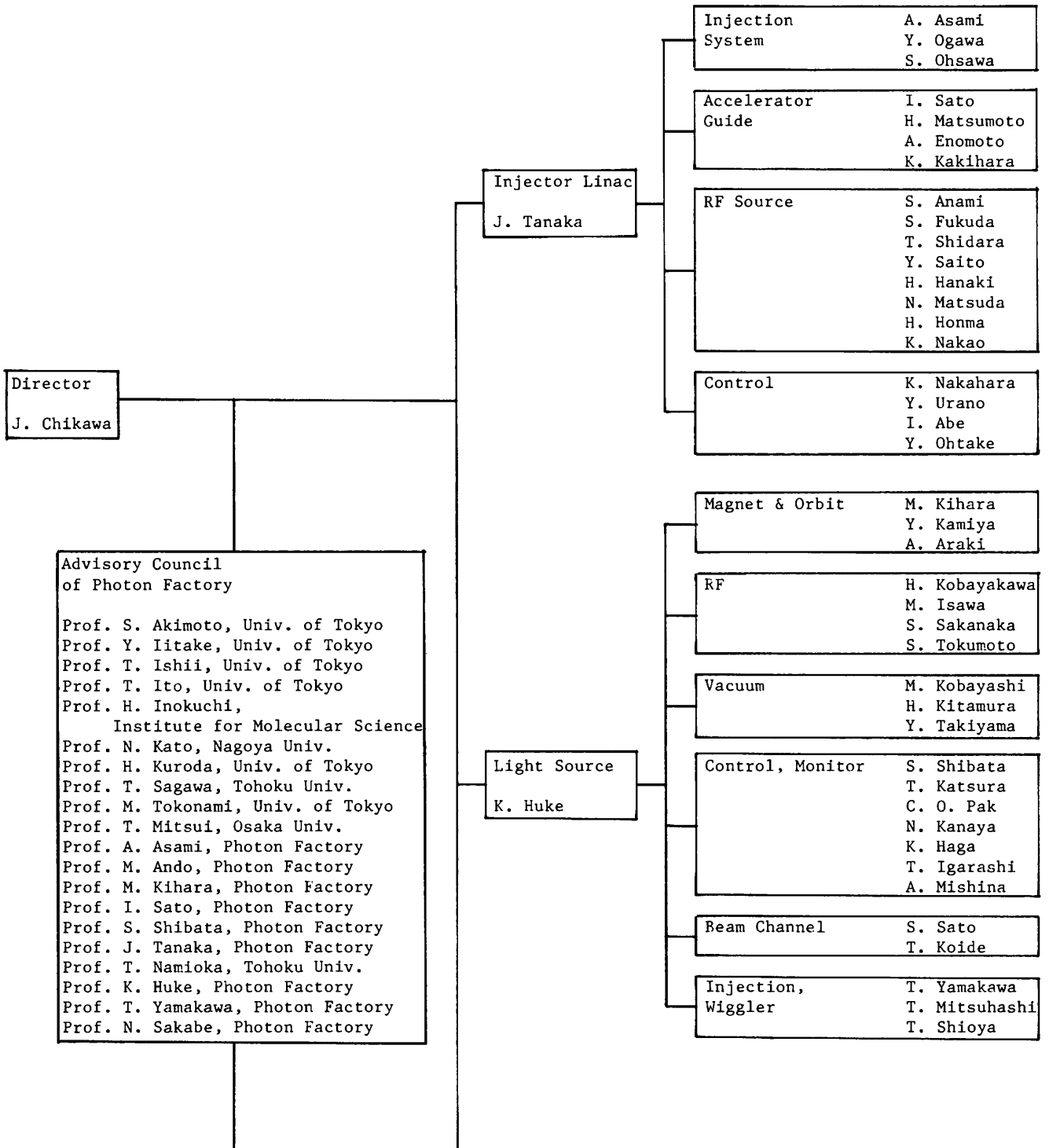
II. ORGANIZATION AND OPERATION

1 Organization

The functional organization and structure of three Departments in Photon Factory, i.e., Injector Linac, Light Source and Instrumentation Department is shown in Fig. 1, along with members of Advisory Council of Photon Factory and

Photon Factory Program Assessment Committee (PAC) as of August in 1985. One of changes is that at the expiration of the term of ex-Director in Photon Factory, Prof. Chikawa arrived at its post in April of 1985. There has been a slight gradual increase in members of subdivision in each Department.

Fig. 1 Organization and members of the Photon Factory



(continued)

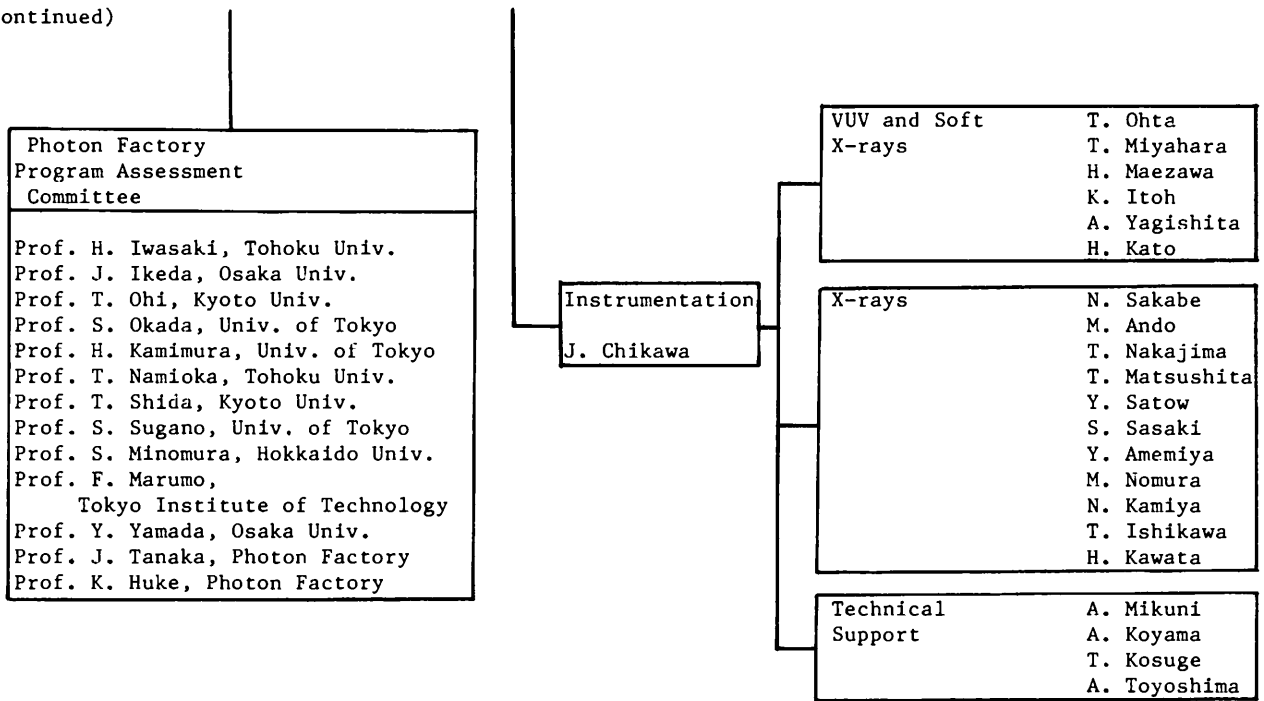


Table 1 Change of running proposals

	Scientific proposals
1983	101
1984	189
1985	255 (as of August, 1985)

Scientific proposals submitted by users, which were reviewed and rated by PAC, based largely on reports obtained from outside non-PAC referees, are constantly increasing from year to year as in Table 1. The PAC meets twice yearly, generally in March and September. Deadlines for receipt of proposals for full consideration at the forthcoming PAC meeting are the middle of January and the middle of July in each year. The allocation of experiment time for approved proposal is valid for twenty-four months.

Since 1983, users meeting jointly with PF staffs have been held annually toward the end of fall in every year. As is called by the name of "Photon Factory Symposium", one of main purposes is that users should present progress reports on their own running proposals in this one year independently of completion or incompleteness of them. The 3rd Photon Factory Symposium was held this year (1985) on November 3-rd and 4-th. Approximately 250 persons with 130 reports almost in progress were in attendance in spite of ideal weather for an outing in two consecutive holidays. In addition to users' reports presented in two poster sessions which were followed by discussion sessions guided by the chairpersons, there were held three hot panel discussions on stabilization of light source, near future project in view of present PF utilization, vision of earthly synchrotron radiation etc. The program for the Symposium and the authors' abstracts in Japanese are available in every time as a special issue stored in PF

bureau.

Photon Factory Symposium, that meets once a year as Star Festival, has produced many valuable remarks and orientations in all aspects of PF operation, improvement, development, and plans of PF for future. Almost concurrently with arrangements for Photon Factory Symposium, a periodical "Photon Factory News (ISSN 0288-691X)" written in Japanese has started and played a part to cultivate the germ of the cooperation spirit between users and PF staffs. It has been issued bimonthly up to #5, vol.3 in back number as of October, 1985, fulfilling an important role both nominally and virtually. From now on, events of PF whether large or small will be chronologically etched on "Photon Factory News".



Symbolic cover mark of Photon Factory News

2. OPERATION

Generally there have been three dedicated runnings to experimental groups a year, i.e., spring cycle, fall cycle and winter cycle. Until this winter cycle, Photon Factory had been operated in weekly running mode as reported in Activity Report 1982/83. Details of ever changing operation time are depicted in Fig. 2.

Since spring cycle in 1985 FY over 2600 hrs per year as in Fig. 2 Photon Factory has been operated in both modes, that is, a 96 hour, five-day week mode and two 240 hour, eleven-day week mode as shown in Table 2.

Figure 3 shows the plan of the experimental hall in Photon Factory, adding the new beam lines and the placement of their experimental stations which are mostly under construction and examination now.

Table 2 Operating schedule

A 96 hour, five-day week schedule

	Sun.	Mon.	Tues.	Wed.	Thur.	Fri.	Sat.
A	*	*	*	U	U	U	M
B	*	*	T	U	U	M	*
C	*	*	U	U	U	M	*

Two 240 hour, eleven-day week schedule

	Sun.	Mon.	Tues.	Wed.	Thur.	Fri.	Sat.	Sun.	Mon.	Tues.	Wed.	Thur.	Fri.	Sat.
A	*	*	*	*	M	U	U	U	U	M	U	U	U	M
B	*	*	*	T	U	U	U	U	M	U	U	U	M	*
C	*	*	*	M	U	U	U	U	M	U	U	U	M	*

A : 1:00 a.m. - 9:00 a.m.
 B : 9:00 a.m. - 5:00 p.m.
 C : 5:00 p.m. - 1:00 a.m.
 M : Machine study, U : Users beam time
 T : Tuning

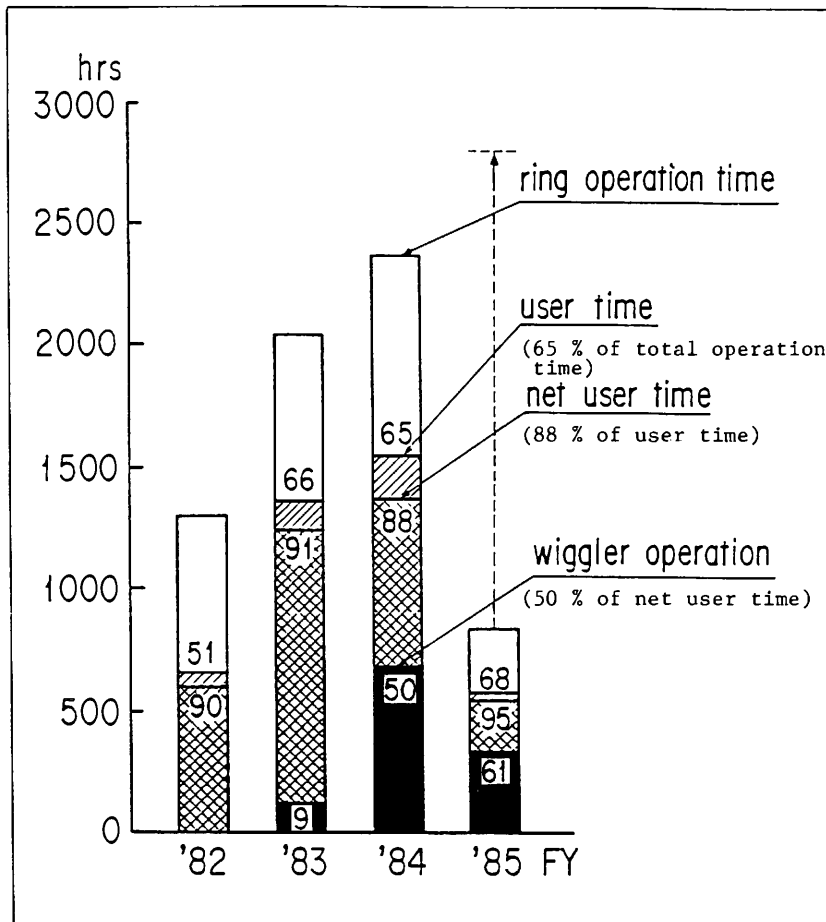


Fig. 2 Statistics on ring operation time of Photon Factory from compilations kindly furnished by Prof. K. Huke.

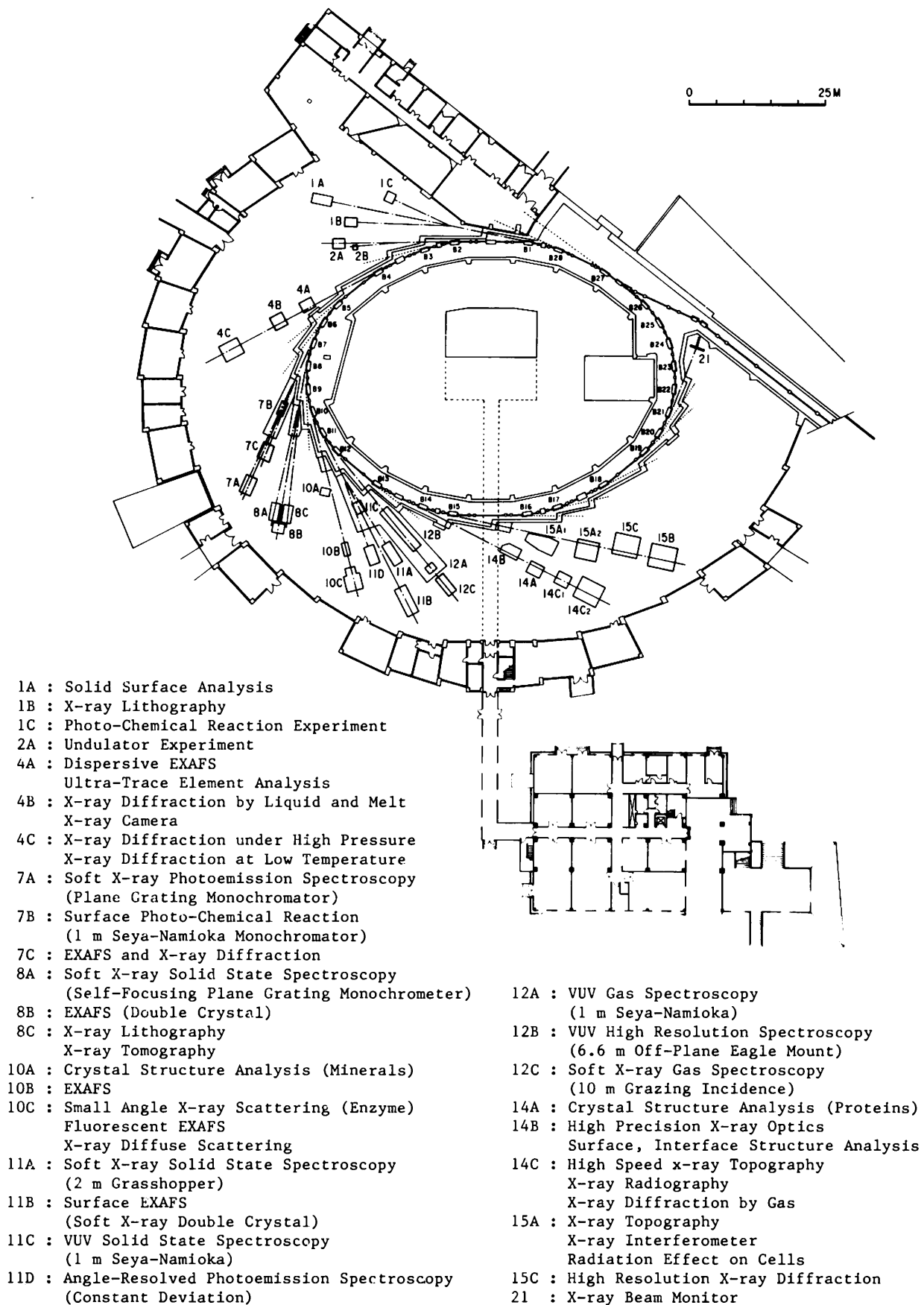
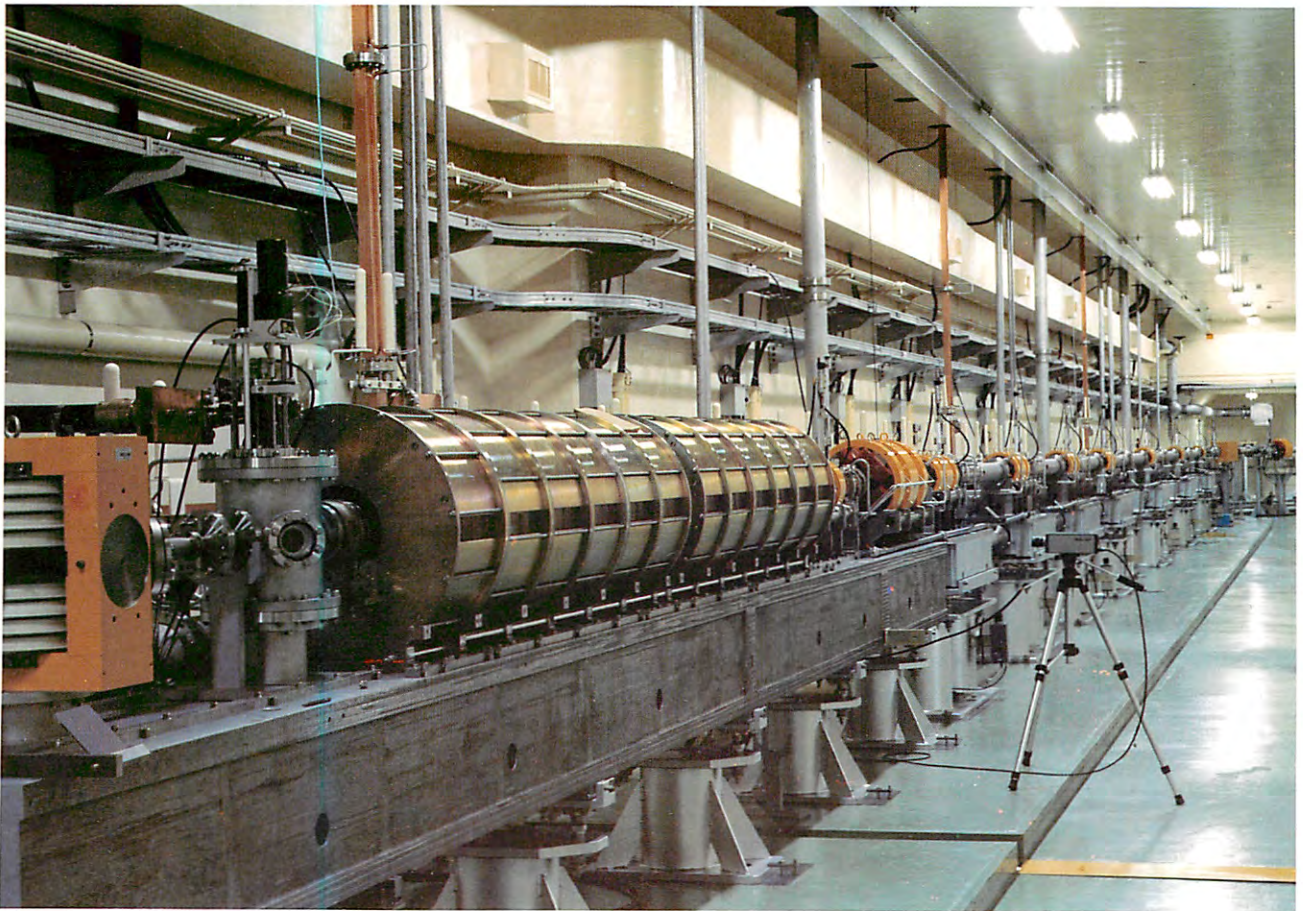


Fig. 3 Plan of the storage ring and the experimental hall.

III. Injector Linac Division



Positron accelerator part of the positron generator.

A positron production target and a pulsed solenoid coil are installed in the vacuum vessel on the left, and followed by an accelerator guide covered with strong solenoid coils.

1. Introduction

The 2.5 GeV injector linac has been reliably operated and has stably provided 2.5 GeV electron beams for the PF 2.5 GeV storage ring and the TRISTAN Accumulation Ring (AR) during FY 1984.

As a beam lifetime of the PF ring was increased over 10 h, a frequency of the injection to the PF ring has been reduced to a few times per day. In the remaining times between the PF injections, the linac beams have been injected into the AR, in which the most part of accelerated and stored beams has been used for calibration of numerous detectors for the TRISTAN experiments and for machine study of the AR. Consequently, the injection frequency for the AR was very high; typically it was a few times per hour.

During FY 1984, total operation time of the linac including accelerator study time of the linac itself was over 2,500 h (Table 1.1). As an increase of the operation time has gradually loaded on the linac staff, substantial improvements to facilitate the operation and the maintenance had to be made.

In the ordinary beam injection into the PF ring, the long pulse beam (0.2 - 0.8 μ s, 30 - 50 mA and 1 pps) is provided for the multibunch mode operation; on the other hand, the short pulse beam for the AR (1.5 ns, 100 mA and 1 - 10 pps) synchronized with rf of the AR is required for the single-bunch mode operation. These two operational modes are quite different for the injector linac. Switchover between them must be made as promptly, easily and reliably as possible. To meet the requirements, the electron gun system and the synchronized trigger control system have been improved.

Internal arcing of the high power klystrons, which has been the most serious problem for the linac since the initial operation, is getting better by improvements of the cathode assembly and the production process of the klystron. With this progress, the fault rate of the klystrons has been reduced from 3 times/h*41 klys. to 2 times/h*41klys. during FY 1984.

Study of the high-power rf windows has been remarkably advanced. A newly installed rf ceramic window is liable to break, especially at rapid rise of the rf power, due to a multipactor effect. To reduce the breakdown rate, enough high-power rf conditioning is necessary. A properly deposited TiN thin film (\sim 50 Å thick) was fairly effective to suppress the multipactoring on the ceramic window surface. However, the break such as puncture and fracture of the windows due to the multipactoring depends on microstructure of the high alumina ceramics as well.

The studies of the high-power rf windows (rf and mechanical structure, ceramic materials, multipactor suppression films, etc.) are now continued with every possible effort.

Fiscal year 1984 is the last year of the 3 years program of the positron generator construction. In the linac department, the construction of the positron generator was well advanced inspite of other heavy routine jobs such as scheduled operation and maintenance of the PF linac. The accelerator guides, focussing, vacuum, beam transport and control systems were all installed at their positions, and the final assembling of the whole system was completed by the end of March.

The first electron beam acceleration test was performed in April 1984, and the first positron beam was successfully accelerated to the energy of 250 MeV in July. At the initial positron generation the primary electron beam was 200 MeV, 1.6 A and 10 ns, and the accelerated positron beam current was 2.3 mA.

In August, the positron beam current was increased up to 2.8 mA, which corresponded to the conversion efficiency of 0.17 %. Acceleration of the positron beam up to the energy of 2.5 GeV and injection into the AR is expected in October.

Table 1.1 Summary of linac operation time.

PF Linac		Positron Generator	
Period	Operation Time (h)	Period	Operation Time (h)
Period II, FY 1984			
Oct. 2 - Dec. 22, 1984	984		
Dec. 23, 1984 - Jan. 15, 1985	shutdown		
Period III, FY 1984			
Jan. 16 - Mar. 16, 1985	720	Apr. 13 - Apr. 18	30
Mar. 17 - May 7	shutdown		
Period I, FY 1985			
May 8 - Jul. 6, 1985	864	Jul. 19 - Jul. 26	120
Jul. 7 - Sep. 30	shutdown	Aug. 7	
SUM	2,568	SUM	150
Total (PF linac + Positron generator)		2,718 h	

2. Electron linac

2.1 Operational status of microwave source

In the period from August 1984 to July 1985, the microwave system had been run stably with the total operation time of 2,600 hours (including high power processing of main klystrons and accelerator guides). The microwave drive system composed of the main booster amplifier and 5 sub-booster amplifiers had operated satisfactorily. The modulators for the high power klystrons had operated stably except for a few small troubles. The major troubles of the microwave source in this period were also the high power klystron failures.

Fourteen klystron assemblies were replaced with new ones. The details are as follows. Three of them were replaced because of the troubles of high power pulse-transformer assemblies (two troubles due to the filament transformer and one due to water leak). Three klystrons were replaced due to their instabilities and one of them was installed again in the klystron gallery after being tested at the assembly hall. There were 8 failed klystrons. The main causes of them were internal arcing (7 tubes) and window breakdown.

Table 2.1 shows the operational performance of tubes during the past 4 years up to July 1985. Seventy-two tubes have been used since 1982. Twenty-eight tubes failed in these periods and their MTBF was 13,400 hours. The mean age of living tubes was 6,200 hours and the mean age of failed tubes was 3,600 hours.

Table 2.1 Cumulative usage hours during the past 4 years.

Period	Total Tubes	Failed Tubes		Living Tubes		MTBF (h)
		No.	Mean Age	No.	Mean Age	
1982/4-1983/3	53	11	1,300	42	2,900	13,500
1983/4-1984/3	63	20	2,300	43	4,200	11,200
1984/4-1985/3	70	25	3,100	45	5,800	13,600
1985/4-1985/7	72	28	3,600	44	6,200	13,400

Table 2.2 shows the more detailed analysis about the operational status corresponding to individual production years. This table also shows that the main causes of the tube failures were internal arcing and window puncture. Also there is such a tendency that the MTBF increases gradually year by year owing to improvements.

Table 2.2 Status corresponding to the year of production. "Standby" tubes are those waiting for retesting. "Unused" tubes are those which have not been used in the klystron gallery at all.

Year	No. of Total Tubes	Living Tubes					Fault rate per day	Voltage (kV)	Failed Tubes				Mean Age (h) Failed Tubes	Mean Age (h) Living Tubes	MTBF (h)
		No. of Working Tubes	No. of Standby Tubes	No. of Nonworking Tubes	Positron	No. of Total Tubes			Arcing	Window	Others				
1979	4	0	0	0	0	—	—	4	2	1	1	3,902	—	3,902	
1980	20	7	1	0	0	1.1	238	12	6	5	1	3,502	8,709	9,307	
1981	20	11	1	0	0	0.7	240	8	4	2	2	3,676	8,901	17,028	
1982	9	4	1	0	0	1.2	233	4	4	0	0	3,412	6,247	11,221	
1983	13	11	0	0	2	1.0	241	0	0	0	0	—	4,513	—	
1984	13	7	0	2	4	0.4	245	0	0	0	0	—	1,454	—	

An important factor on the linac operation is the klystron fault rate, because many faults lead to interruption of beam injection into the PF ring or the TRISTAN Accumulation Ring. Table 2.2 shows also the fault rate corresponding to each of the production years. Table 2.3 shows the fault rate and the applied voltage from October 1982 to July 1985. It indicates a tendency that the fault rate decreases year by year.

Table 2.3 Operational status (fault rate).

Year	Period Month	Fault rate (per day per 41 tubes)	Average of applied
			voltage (kV)
1982	10 - 12	3.5	236
1983	1 - 3	4.4	238
	5 - 7	4.6	239
1984	10 - 12	3.3	241
	1 - 3	2.6	243
	5 - 7	2.4	242
1985	10 - 12	2.6	241
	1 - 3	2.1	239
	5 - 7	1.5	241

Some efforts to improve the tube have been continued at the manufacturer. One of the main improvements was made for processing of production. Vacuum firing of the gun assembly by induction heating were performed sufficiently for outgassing by using oil-free pumps. The thermal shield of the gun heater led drastically to the improvement of the heater power-emission characteristics. A double vacuum baking vessel was also developed at the manufacturer, and klystrons which were produced in the vessel will be delivered in the near future.

2.2 Beam characteristics and measurements

Beam emittance measurements

Beam emittance is one of the most fundamental quantities in accelerators. The emittance measurement was performed in the following method. The beam radius at a fixed point of the linac varies as a hyperbolic function of field strength of upstream focussing magnets. The emittance is given as a function of the minimum radius and the gradient of asymptote of the hyperbola.

In this method it is required to measure only a beam current spacial distribution at one position with a beam profile monitor: a ceramic screen. With mirrors and lenses the image of the beam profile was focussed on a photodiode array as shown in Fig. 2.1. The array consists of 35 silicon diodes; each of them is horizontally separated by 1 mm with a vertical length of 5 mm. The output signals from the array are processed with a 64-channel sample-and-hold circuit and a multiplexer, and are observed on an oscilloscope. A typical example of the multiplexer output is shown in Fig. 2.2; the beam current is distributed over an area of ~ 3 mm in diameter at FWHM. The beam current dependence of the output voltage of the sample-and-hold circuit was tested and confirmed to be linear within a few percent. A result of the measurement is shown in Fig. 2.3. From this curve the emittance is obtained to be $1.2\pi \times 10^{-2}$ MeV/c·cm at a beam current of 50 mA.

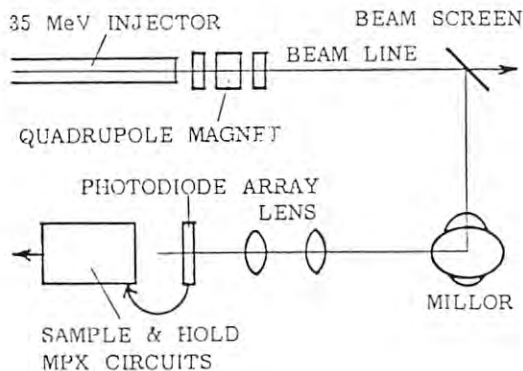


Fig. 2.1 Layout of the emittance measurement apparatus.

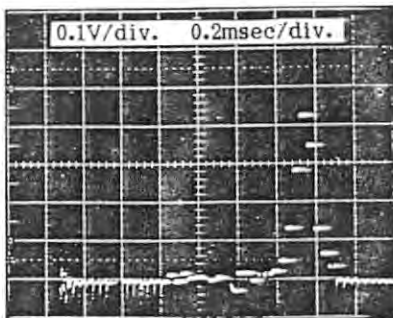


Fig. 2.2 Example of the photodiode array output.

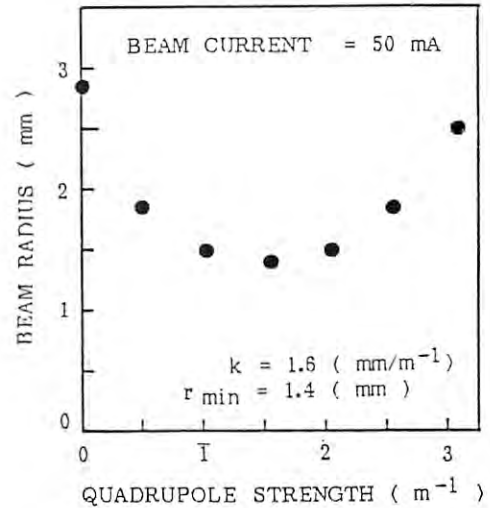


Fig. 2.3 Beam radii measured against the field strength of the quadrupole magnet.

Stability test of short pulse beam triggering

Stability of the trigger timing for a short pulse beam was tested by observing the beam injected into the TRISTAN Accumulation Ring (AR). In order to check the influence of the optical fiber cable length, a trigger signal was transmitted from an rf synchronizer to a gun pulser using a long cable (180 m) instead of a short one (30 m) used in the usual operation. The phase of the 509 MHz signal from the AR was varied with respect to the rf phase in the accelerating cavities of the AR. To test the phase stability against the beam trigger timing, the beam was injected and stored in the AR at each of several phase angles.

Characteristics of the beam bunch stored in the AR were studied by observing bunch monitor signals on an oscilloscope. Figure 2.4 shows the signal of a single bunch beam injected into the AR at a certain acceleration phase angle. Over the phase angle variation 140 degrees around this phase angle, no significant change of the signal waveform was observed in neighboring buckets. Therefore it can be concluded that even in case of the long optical fiber (180 m) the change in the beam trigger timing is tolerable over a range of 140 degrees in the 509 MHz rf phase to achieve a single bunch beam in the AR.

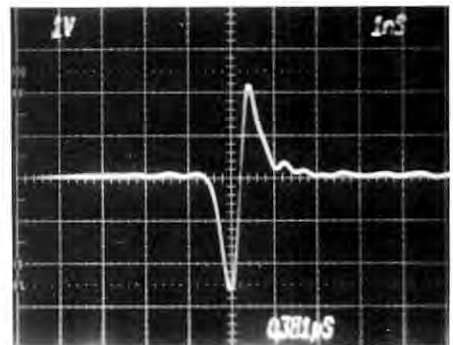


Fig. 2.4 Bunch monitor output of a single bunch beam in the AR.

2.3 Development

Signal transmission system for a short-pulse beam monitor

A short pulse beam of 1.5 ns width is accelerated up to 2.5 GeV with the PF linac, and is injected into the AR. In this operation it is necessary to observe the waveform and amplitude of signals from beam current monitors. When a long coaxial cable is used, distortion of the signal becomes considerable owing to large attenuation of signals and its frequency dependence. Therefore, the long-distance transmission of the monitor signal to the main control room was made using a graded-index type of optical fiber of silica with a core diameter of 50 μm .

The system is composed of three components: a sensor to detect the beam current, an optical fiber, and a pair of E/O and O/E converter. As a beam current monitor, either of a wall-current detection type or a current transformer type is available. The output signal is transmitted via a semirigid coaxial cable (SFZE 50-4-P) to an E/O in the klystron gallery. The optical fiber cables are laid down between the klystron gallery and the main control room.

The performance of the system was tested first with a pulse generator on the waveform distortion and the linearity. The result was satisfactory. Then the system was tested with actual electron beams. A typical example of the results is shown in Fig. 2.5. Figure 2.5(a) shows the waveform of the output signal of a wall-current monitor, observed in the klystron gallery through a 7 m long semirigid coaxial cable; this monitor is installed in the first sector of the linac. The observed pulse has a width (FWHM: Full Width at Half Maximum) less than 2 ns, where the peak current of the beam is about 100 mA. The optical fiber used is 200 m long. The signal observed in the main control room is shown in Fig. 2.5(b); the pulse is a little wider than that in Fig. 2.5(a), and a small ringing can be seen at the tail. Except these, the signal observed in the control room reasonably represents the input waveform.

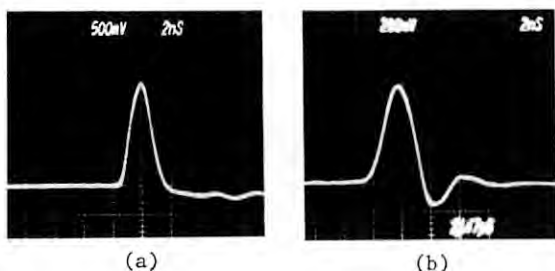


Fig. 2.5 Signals from a wall current monitor installed at the sector #1.
(a) Output waveform observed at the klystron gallery.
(b) Waveform after transmission through the optical fiber.

Another test was also made by using a 550 m long fiber. The detector used was a ferrite core monitor installed nearly at the end of the linac. Figure 2.6(a) shows the input signal of the E/O converter, and Fig. 2.6(b) is the output signal from the O/E converter. In this stage the ringing was made much smaller than that in the previous example (Fig. 2.5(b)) by fine tuning of the circuit. High frequency components observed in Fig. 2.6(a) were smoothed out and not seen at the output (Fig. 2.6(b)), but the input signal on the whole seems to be well represented by the output signal.

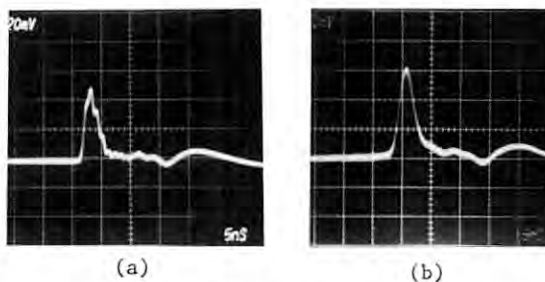


Fig. 2.6 Signals from a beam current monitor installed at the end of the linac.
(a) Output waveform observed at the klystron gallery.
(b) Waveform after transmission through the optical fiber.

Beam diagnostic system

A beam diagnostic system was developed in collaboration with a visitor from the Institute of High Energy Physics in Beijing. Figure 2.7 shows a block diagram of the system. TV video signals from a screen monitor are digitized by a waveform digitizer synchronously with a beam trigger. These digital data are transferred to a personal computer FM-11 through the GPIB and are analyzed to obtain a structure of the beam profile. An example of the beam profile obtained by this system is shown in Fig. 2.8.

An improved version of this system will be used for making it easy to adjust the beam focussing and steering system.

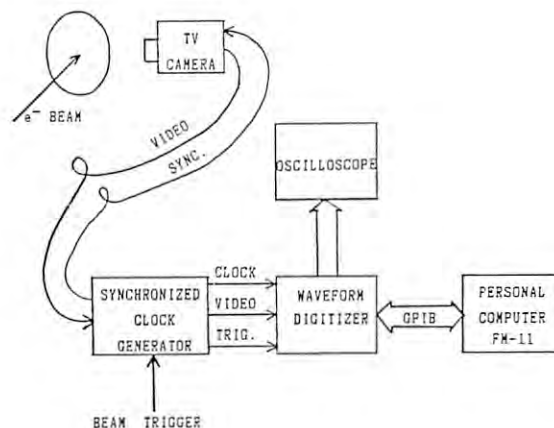


Fig. 2.7 Block diagram of the beam diagnostic system.

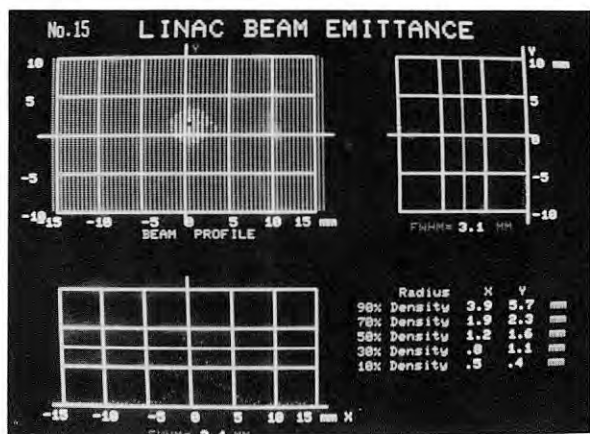


Fig. 2.8 An example of a beam profile obtained by the beam diagnostic system.

Rf windows

The failure of rf windows, which are used in the high power klystrons (MELCO PV-3030A) and in the waveguide system of the PF linac, has been a serious problem for the last five years. Up to the present, 11 klystrons were replaced by new ones because of the window breakdown such as punctures and cracks. Also 22 of the waveguide windows were failed due to the same kind of breakdown and they were replaced by new windows.

(1) Observation of punctures

The rf window is composed of a high purity Al_2O_3 ceramic disk (3.5 mm thick, 92 mm in diameter) and a pillbox housing. The failure of window is mostly caused by the puncture through the ceramic disk from one side to the other. Figure 2.9 shows one of photographs of the ceramic disks broken by the punctures. The broken windows are slightly colored yellow. It is due to the electron bombardment, which will be described later. The typical puncture is shown in Fig. 2.10. From this photograph it can be seen that Al_2O_3 and binding matrix around the holes are melted. It is considered that the extremely localized heating took place on the surface, and it caused to make a puncture.

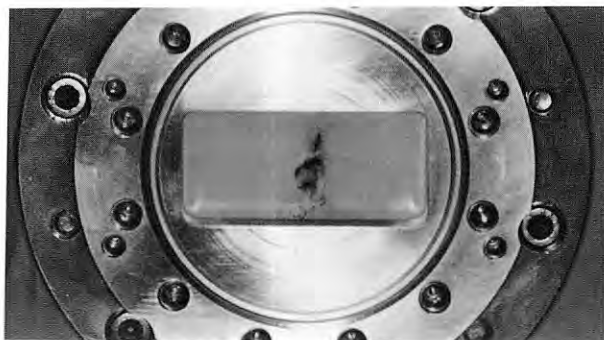


Fig. 2.9 Broken ceramic disk and a pill-box housing.



Fig. 2.10 Microscopic photograph of the puncture.

Figure 2.11 is a cross-sectional microscopic photograph of the puncture, and shows that the puncture has the branches, which is like a Lichtenberg's pattern. From these observations, it can be concluded that the puncture is initially generated on the surface by thermal heating, and then grows up through the ceramic disk to the other surface with branching out. Voids and grainboundaries of the ceramic disk material are observed with a microscope as shown in Fig. 2.12. The preparation process of the samples for microscopic observation is the following:

Surface polishing to obtain a smooth surface by removing a surface thin layer of about $50 \mu\text{m}$ in depth with diamond paste.

Etching by phosphoric acid for 10 minutes to several hours according to the thickness of the grainboundaries.

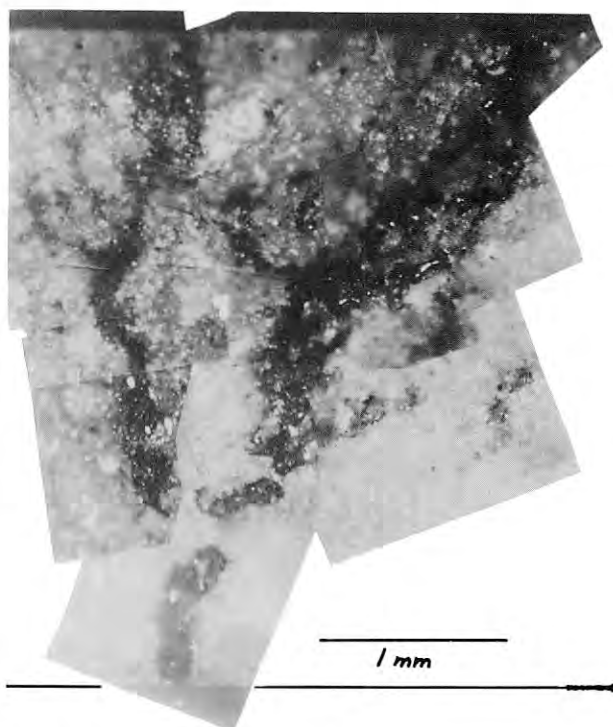


Fig. 2.11 Cross-section of the punctured ceramic disk.

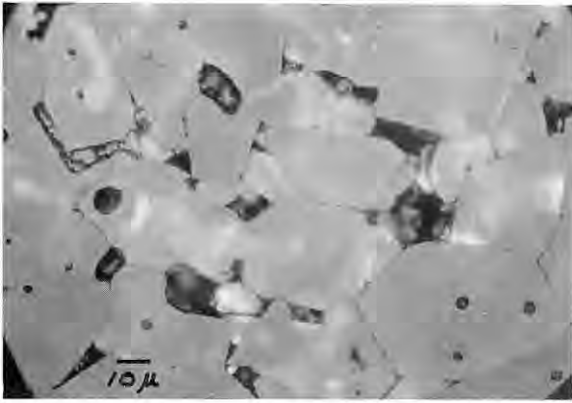


Fig. 2.12 Voids and grainboundaries in the ceramic disk.

These bulk singularities are considered as dielectrical weakness, and the puncture would propagate along them and make branches in the bulk. They seem to be also the starting point of the puncture at the surface as well as the route for the puncture propagation, and it seems that the ceramic disk of higher density is more resistive to the puncture. In fact, when the ceramic disk with lower porosity than that shown in Fig. 2.12 is used, the window is not so often broken.

(2) Luminescence of the Al_2O_3 disk

To investigate the generating mechanism of the puncture, some experiments on the surface phenomenon of the ceramic windows under the high power operation have been carried out. Figure 2.13 shows the schematic drawing of the experimental apparatus. The maximum output power from the klystron is 30 MW with the pulse width of 2 μs . The waveguide is terminated by a water load (VARIAN). The rf window to be tested is inserted between the klystron and the water load.

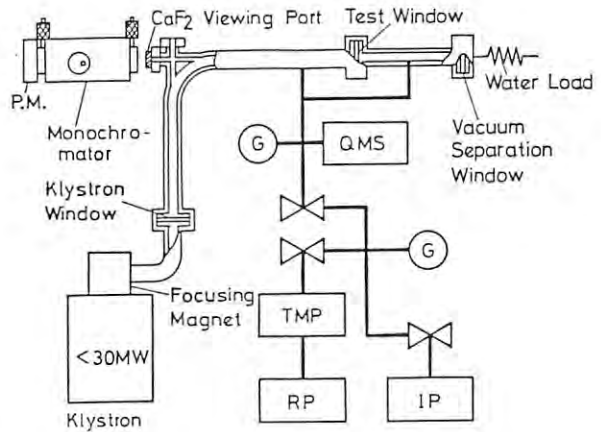


Fig. 2.13 Schematics of the waveguide system.

The waveguide system is evacuated by a turbomolecular pump and an ion pump and the ultimate pressure is less than 10^{-7} Torr. For the outgasing observation a quadrupole mass spectrometer is set to the pumping system. The conditioning of the rf window and the waveguides is carried out. This is a surface cleaning process with rf power, in which adsorbed gases on the metal and ceramic surfaces are desorbed. The pressure is always kept less than 10^{-6} Torr during the conditioning in which the rf power is gradually increased. With the residual gas measurement, it was found that the desorbed gas species were H_2 , CO, CO_2 and some hydrocarbons when the rf power is turned on. Under the conditioning with the rf power less than 1 MW, degasing is mostly finished. When the rf power more than about 1 MW is fed to the system, the optical emission from the ceramic disk accompanying with a small amount of outgasing is observed. For further investigation of the optical emission process, the spectrum analysis

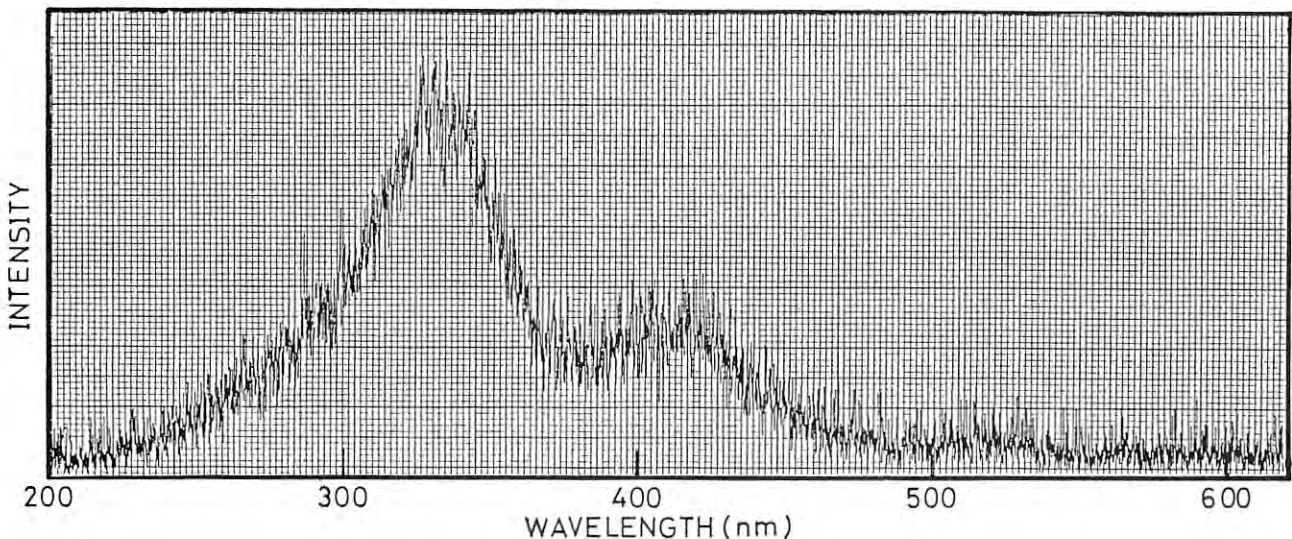


Fig. 2.14 Optical emission spectrum of Al_2O_3 ceramic disk with applied microwave power of 5.1 MW.

using a monochromator has been carried out. A CaF_2 viewing port, which is transparent for the wavelength from UV to several μm , is mounted on the E-bent waveguide. Figure 2.14 shows the optical emission spectra which was typically observed. The broad peaks at about 330, 410 and 515 nm with the half width of 70 - 100 nm were found, while there was no line spectrum. Figure 2.15 shows a life-time of the optical emission at the wavelength of 330 nm. This is the output signal of the photomultiplier which is attached behind the monochromator exit slit. From this signal observation, it was found that the optical emission has the longer life-time of several milliseconds. The optical emission with such a broad half-width and a longer life-time can be explained by a luminescence of Al_2O_3 ceramic disk surface caused by electron bombardment. In fact, the spectra are similar to the cathodoluminescence spectra of this specimen which was measured with a specially modified scanning-electron-microscope equipped with a monochromator. Thus, it can be concluded that the observed optical emission is not owing to the ionized or excited gas molecules adjacent to the surface, but the luminescence of Al_2O_3 due to the electron bombardment.

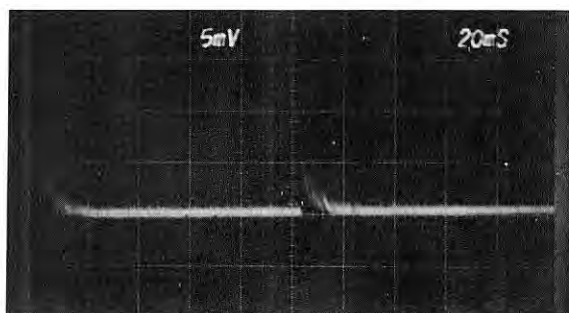


Fig. 2.15 Decay of optical emission intensity of 330 nm peak with microwave power of 5.1 MW in the repetition of 10 pulses per second.

(3) Suppression of multipactor

The electron bombardment due to multipactor on the ceramic surface should damage or degenerate the ceramic disk, and also heat up the surface to cause a puncture and cracks. In fact, it is observed that the ceramic disk removed from the waveguide system after the long-time high power operation is slightly colored yellow with the pattern similar to that of optical emission, and in this area there are shiny stains which is found to be melted. Generally, Al_2O_3 has a large value of secondary electron emission coefficient. Thus, the electron bombardment due to multipactor is considered to be enhanced by secondary emitted electrons from Al_2O_3 which will again impinge on other parts of the surface by reversing rf electrical field. This is called multipactor. As is

well known, some metal compounds such as TiN have lower values of secondary electron emission coefficient. Therefore, when they are deposited on the ceramic window surfaces, they are expected to suppress the secondary electron emission and the multipactor. The TiN coating with thickness of 50 Å on the ceramic window has been tested.

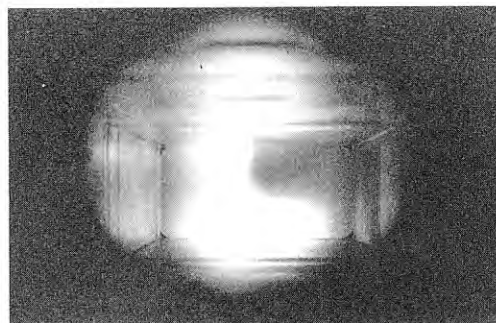


Fig. 2.16 Luminescence pattern of the ceramic disk. A quarter area (upper right side) of the disk surface is coated by TiN film.

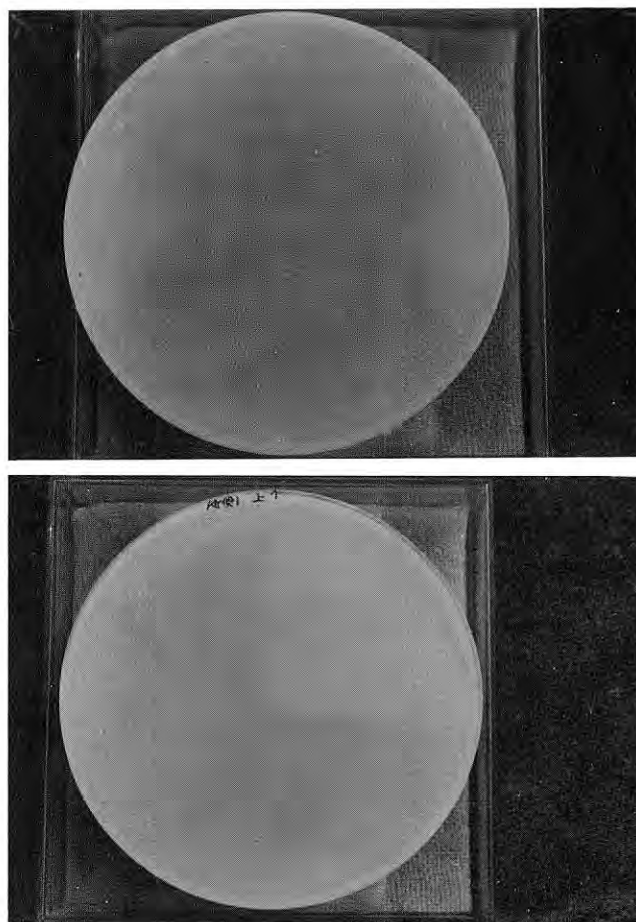


Fig. 2.17 Ceramic disk after high power operation.
Above: Whole area was uncoated.
Bottom: A quarter area of the surface was coated.

The intensity of the luminescence for this coated window is lower than that for uncoated windows by 30 dB, and no heating is measured. Figure 2.16 shows the luminescence pattern for the window, only a quarter of whose ceramic window surface was coated by TiN film. The difference of the luminescence intensity between the coated and uncoated area is noticeable. Also the difference of the electron bombardment effect on the ceramic disk surface can be seen in Fig. 2.17. In the coated area, there is neither yellow coloring nor shiny stains. Thus, it can be concluded that the TiN coating on the ceramic window suppresses the multipactor.

(4) Sputter coating apparatus

To prepare the TiN coated ceramic disks for the waveguide windows, a DC magnetron sputtering apparatus has been designed and constructed. To obtain the well-controlled TiN film suitable for the rf window performance, it is necessary to characterize the fundamental properties of the film. The system is designed so as to make it feasible to observe in-situ the surface in the initial stage of the film growth and to analyze the contents of the film without breaking the vacuum. A schematic drawing of the apparatus is shown in Fig. 2.18. The whole system is bakeable to obtain the ultra high vacuum (UHV), and is evacuated with a turbo-molecular pump, a Ti sublimation pump and an ion pump. The ceramic disk is thermally cleaned by a radiation heater.

The characterization of ceramic surface and the coated film is carried out with an Auger electron spectroscopy (AES) and an Ar ion gun. The AES system can be separated by the gate valve during sputtering in which pressure is about 10^{-3} Torr. The plasma can be characterized by a Langmuir probe, a quadru-pole mass spectrometer and a monochromator. The thickness of the film is monitored by a quartz oscillator. The bias potential of the ceramic disk can be applied by the grid mesh located between a shutter and the disk. After sputter coating, the system is again reached to the UHV of 10^{-9} Torr and the AES system can be operated. Figure 2.19 is an example of AES results observed for the TiN film coated on the ceramic disk. The small peak of carbon compared with the large peaks of Ti+N and Ti indicates that the TiN film containing less contamination can be produced with this sputtering system.

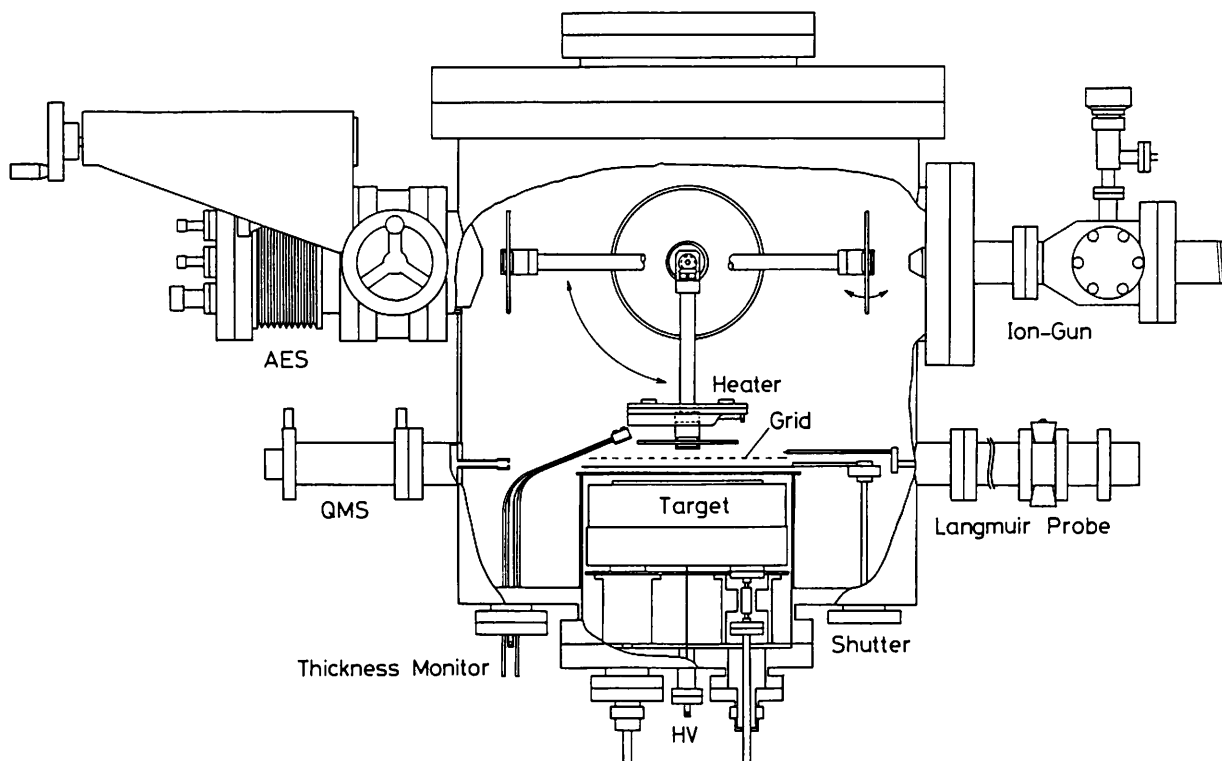


Fig. 2.18 Schematic drawing of DC magnetron sputter apparatus.
AES: Auger electron spectroscopy; QMS: quadru-pole mass spectrometer.

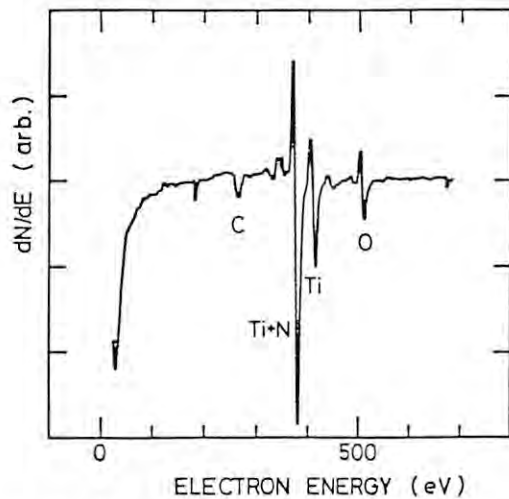


Fig. 2.19 AES spectrum of TiN film on the ceramic disk.

Resonant ring

It has been desired to construct an apparatus that enables to test microwave components with very high power. Because the failure rate of rf windows is very high in the PF linac, it is required to obtain rf power at least four times as high as that in normal operation to develop more reliable rf windows. This means that 120 MW or more high power is necessary. At present, 30 MW at maximum per klystron is available (a 150 MW klystron was developed under the Japan-U.S.A. collaboration, but it is not yet of practical use). To achieve a higher power in a waveguide system for a given klystron output power, a traveling wave resonator, so-called resonant ring, was adopted.

A schematic diagram of the practical resonant ring is shown in Fig. 2.20. The resonant ring consists of the following components: an input directional coupler, a phase

shifter, monitoring directional couplers, viewing ports and waveguides. This design is based on the SLAC resonant ring, and the formulations described below were developed by Dr. W.R. Fowkes (private communication).

The operational principle of the resonant ring can be illustrated as follows with the aid of Fig. 2.20. The incident wave from the klystron is divided into terminals (c) and (d) at the input directional coupler. The wave fed from (d) into the ring propagates around the ring circuit and reaches the coupler terminal (b). Then this wave is also divided into (c) and (d). If the electrical length of the ring circuit is tuned to obtain resonant condition by the phase shifter, the fields will be added in phase at the coupler, and the field in the ring circuit will build up to be larger than that in the waveguide from the klystron. Using the notation described in Fig. 2.20, a ring voltage gain for the properly adjusted ring circuit may be described as

$$|M|_{\max} = \frac{C}{1-T\sqrt{1-C^2}} \quad (1)$$

For a given attenuation, an optimum coupling factor is given by

$$C_{\text{opt}} = \sqrt{1-T^2} \quad \left(\frac{\partial |M|_{\max}}{\partial C} = 0 \right) \quad (2)$$

By substituting eq. (2) into eq. (1), the optimum ring voltage gain is obtained to be

$$M_{\text{opt}} = \frac{1}{\sqrt{1-T^2}} = \frac{1}{C_{\text{opt}}} \quad (3)$$

If such an effect is taken into account as the reflection from ring circuit components, eq. (1) should be changed as follows:

$$|M|_{\max} = \frac{C(1-T\sqrt{(1-C^2)(1-\Gamma^2)})}{1-2T\sqrt{(1-C^2)(1-\Gamma^2)}+(1-C^2)T^2} \quad (4)$$

Approximately, the input reflection coefficient Γ_{IN} seen from the generator is

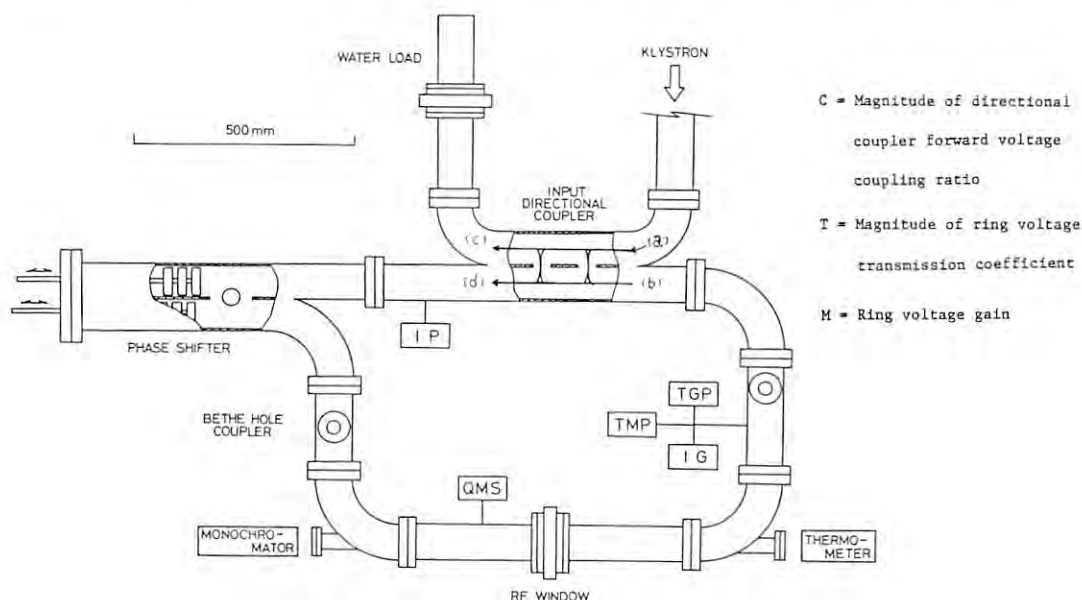


Fig. 2.20 Schematic diagram of the resonant ring system.

$$\Gamma_{IN} \approx \frac{C^2 \Gamma}{1 - 2T\sqrt{(1-C^2)(1-\Gamma^2)} + (1-C^2)T^2} \quad (5)$$

This shows that Γ_{IN} may become appreciable even though the reflection coefficient (Γ) in the ring is small. To reduce the reflection a matching tuner is also required in the ring circuit.

In order to optimize the operation of the resonant ring for testing components with various characteristics, it is favorable to use a variable input directional coupler. However, its operation is not easy under a high power condition. Therefore, a fixed coupler (10dB, $C = 0.32$) was adopted instead of a variable type. The attenuation of the ring circuit is estimated to be 0.16 dB ($T = 0.98$); consequently, the ring voltage gain 4.6 is obtained from eq. (1). With the optimum coupling coefficient for this attenuation (i.e., 14.4 dB, $C = 0.19$), the optimum ring voltage gain 5.2 can be derived from eq. (3).

To obtain a resonant condition the electrical length of the ring circuit is adjusted by the phase shifter, which consists of a 3dB hybrid coupler and two short plungers simultaneously movable. The insertion loss and VSWR should be as low as possible; these should be less than 0.05 dB and 1.1, respectively. Also this phase shifter must be operated up to 120 MW without breakdown.

To monitor the inside rf power, 80 dB Bethe hole couplers were used.

An evacuating system for ultra high vacuum was also designed to make it possible to measure the pressure dependence of the breakdown power for the microwave components.

The waveguide parts and the vacuum components for the resonant ring have been assembled, and the entire system was checked for vacuum leak. A photograph of this system is shown in Fig. 2.21. Rf measurements were made for the individual components before assembling the ring. The coupling of the input directional coupler was 10.75 dB, which was slightly smaller than the designed value. After assembling the ring, low level rf measurements were made. The measured Q_L and the attenuation of the ring circuit, which included an effect of the reflection in the ring,

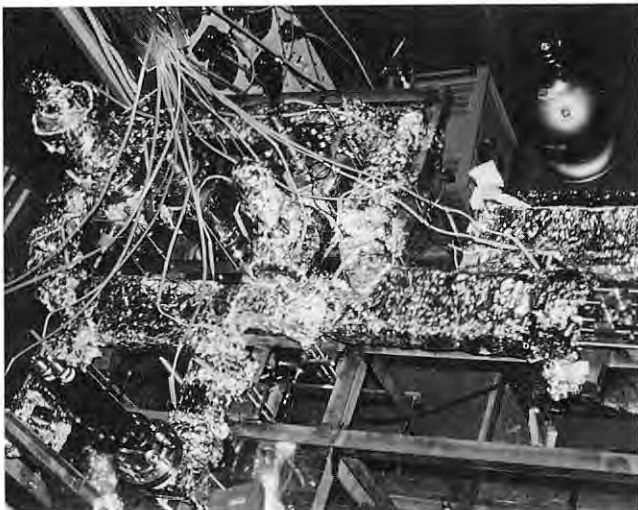


Fig. 2.21 Photograph of the resonant ring.

were 2500 and 0.19 dB, respectively. The measured input reflection coefficient Γ_{IN} was 0.5. These measurements show that at least 9 times of the input power will build up in the ring circuit.

After evacuation the ring was baked to reach vacuum pressure about 4×10^{-9} Torr. Figure 2.22 shows the result of the initial high power test of the resonant ring; about 19 times of the input power built up in the ring circuit, which was in good agreement with expected value.

A high power test of rf windows is scheduled after careful conditioning of this resonant ring.

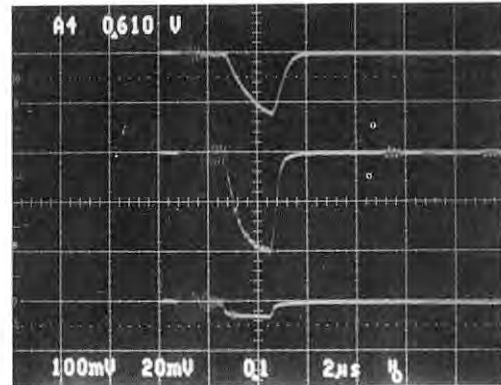


Fig. 2.22 Results of the initial high power test of the resonant ring.

Upper: Backward power in the ring circuit (16 MW).

Middle: Forward power in the ring circuit (210 MW).

Lower: Input power (11 MW).

3. Positron generator

3.1 Injection system

Construction of the injection system has been continued by the end of FY 1984. A pre-buncher, a buncher and beam transport elements have been manufactured in accordance with the design described in a previous Activity Report. The design of the vacuum system around the gun was carefully made to obtain ultra-high vacuum, which necessitated a small modification of the beam transport system. The rf waveguide system for the buncher and prebuncher was newly designed, particularly for made a high power variable attenuator and a phase shifter.

Electron gun

The gun itself is of the same type as that used in the PF linac. However, the final beam current expected for the gun is 10 - 15 A to produce a positron current of ~ 10 mA. To obtain such a high current it is necessary to keep a clean ultra-high vacuum around the cathode. Therefore, vacuum pumps for the gun were reinforced, and the associated vacuum components were designed to be bakable. In addition, a differential pumping method was applied to prevent vacuum deterioration due to the downstream beam duct of the gun. The vacuum system around the gun is shown in Fig. 3.1.

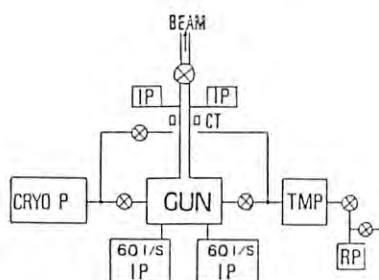


Fig. 3.1 Vacuum system for the electron gun.

Another equipment which is important to produce a high current from the gun is a grid pulser. For the initial beam test it is more convenient to use a beam pulse wider than the normal one; thus 10 ns was chosen for this. Figure 3.2 shows the circuit diagram of this

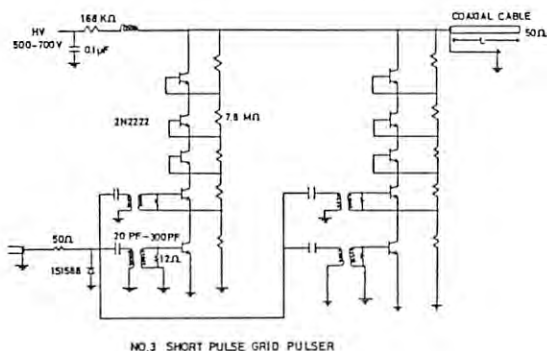


Fig. 3.2 Grid pulser.

pulser; electric charge stored in a coaxial cable is discharged by switching avalanche transistors connected in parallel. With this pulser a beam current of 4 - 5 A can be obtained.

Rf waveguide system

In the waveguide system for the prebuncher and buncher, there must be variable rf attenuators and rf phase shifters. In most of linacs including the PF linac, high power attenuators and phase shifters are usually operated with pressurized SF₆ gas to prevent rf breakdown. In the present case, however, those were designed to be used in vacuum and manufactured in use of conventional 3 dB hybrid power dividers. In the new system any pressurizing equipment such as rf windows and an external evacuating unit become unnecessary, and maintenance is expected to be much simpler. No trouble has been experienced with this system in the test operation. The attenuator and phase shifter for the prebuncher are operated in atmospheric pressure because the rf power is low. Figure 3.3 shows this waveguide system.

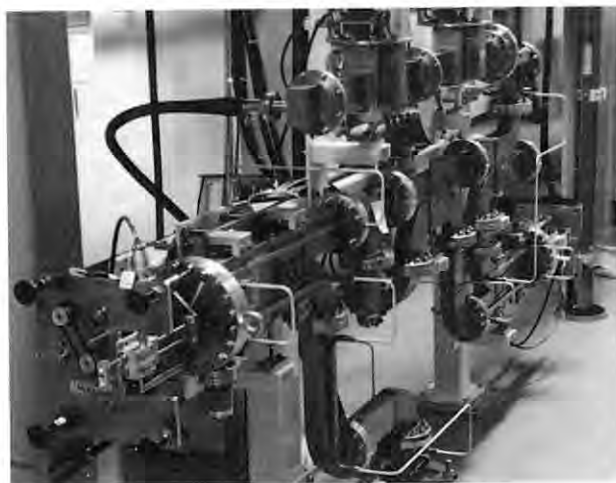


Fig. 3.3 Waveguide system for the buncher and prebuncher.

Performance

In this generator only a short pulse beam is necessary for injection into the AR. However, a grid pulser and associated circuits, which are able to generate a rather longer pulse beam, are also provided for convenience of tuning of the generator. In the test operation both of these beam pulses were examined, but the result is described here only about the test performed with a short beam pulse of 10 ns width.

Figure 3.4 shows a beam pulse measured with a ferrite core monitor installed just downstream from the gun. Although monitors of this type were developed for a long pulse beam, it is available for a short pulse beam when it was calibrated at the short pulse width. The electron gun current in this case is 3.4 A. A wall-current monitor is installed between the first and second accelerator guides, and a beam pulse observed with this detector is shown in Fig. 3.5, where the peak current is 2 A.

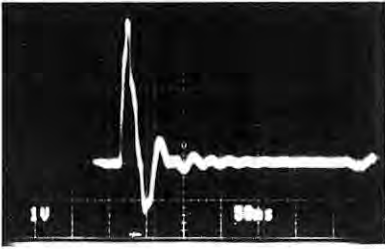


Fig. 3.4 Current injected from the gun (observed with a ferrite core monitor).

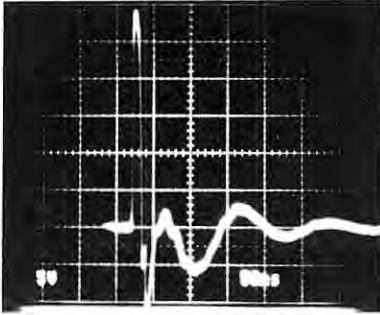


Fig. 3.5 Accelerated beam (observed with a wall-current monitor).

Another wall-current monitor, which was installed in the middle of the second acceleration unit, indicated the accelerated current was also 2 A. Therefore, almost all the beam are successfully accelerated without appreciable beam loss after the first accelerator guide of the first unit.

Thus the injection was satisfactorily performed and the test operations were quite successful at the present stage. However, the obtained current is still far lower than the final target value, so that an effort is proceeding to increase the emission current from the gun. To obtain the more intense beam a subharmonic buncher will be added.

3.2 Beam transport system

In the positron generator, a high current electron beam accelerated up to an energy of about 200 MeV strikes a tantalum radiator. The positrons emitted from the radiator is focussed and accelerated to 250 MeV in the remaining linac. Parameters relevant to the beam transport system are listed in Tables 3.1 - 3.3.

Electron focussing system

A low $\beta(v/c \ll 1)$ and high-current electron beam emitted from the gun rapidly disperses due to the strong space-charge force. In this region, therefore, a strong uniform solenoid is required to focus the beam into the accelerator aperture. The field strength of 300 G is required to obtain the beam radius of 7 mm; that is given by the formula:

$$B_z = \frac{0.369}{b} \left(\frac{I}{(\gamma^2 - 1)^{1/2}} \right)^{1/2} \text{ (G) ,}$$

where I: beam current (A), b: beam radius(m).

The electron beam with velocity of $\beta \sim 1$, which is bunched and accelerated to about 5 MeV by the buncher, is focussed by five sets of quadrupole triplets; calculation shows that if the quadrupole multiplets are distributed suitably, the electron beam is focussed symmetrically in both horizontal and vertical planes as shown in Fig. 3.6.

Table 3.1 Electron beam parameters.

Emittance	$5 \times 10^{-3} \pi \cdot \text{MeV}/c \cdot \text{cm}$
Gun high voltage	100 - 150 keV
Gun current	10 A max
Electron energy	$\sim 200 \text{ MeV}$
Energy gain	$\sim 10 \text{ MeV/m}$

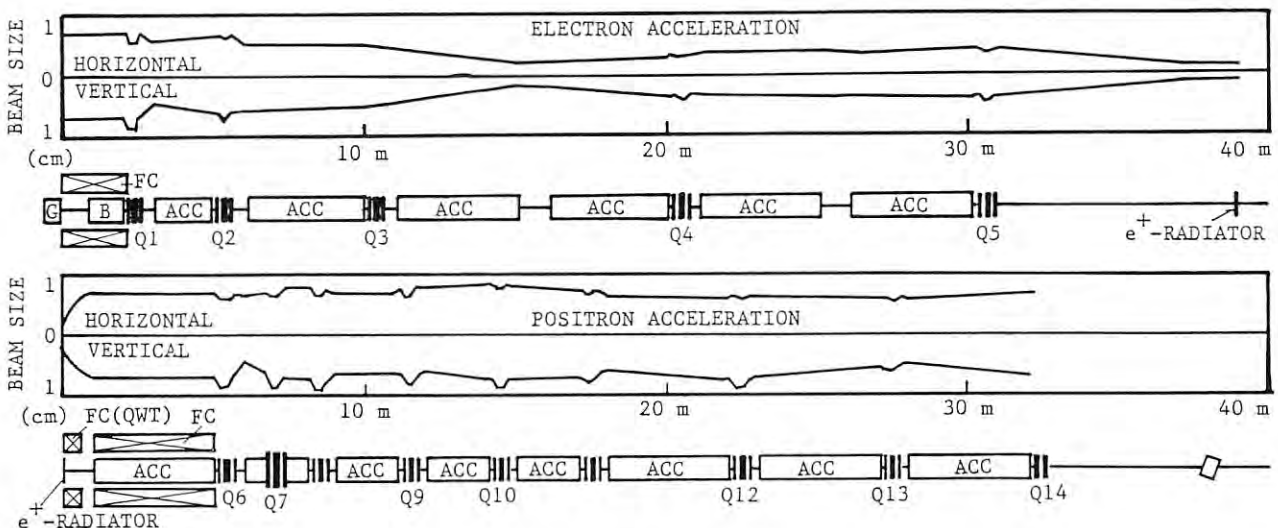


Fig. 3.6 Computed beam envelope and beam transport system.
Upper: Electron beam from the gun to the positron radiator.
Lower: Positron beam from the radiator to the end of the linac.

Positron focussing system

The positron focussing system functions as a phase space transformer between the diverging large momentum beam emitted from the radiator and the small transverse momentum beam matched to the transport system of the accelerator; this phase diagram is shown in Fig. 3.7.

In the generator the focussing system called the "quarter wave transformer" is adopted. This system consists of a high-field, short-range uniform solenoid and the following long low-field uniform solenoid. Figure 3.8 shows an example of

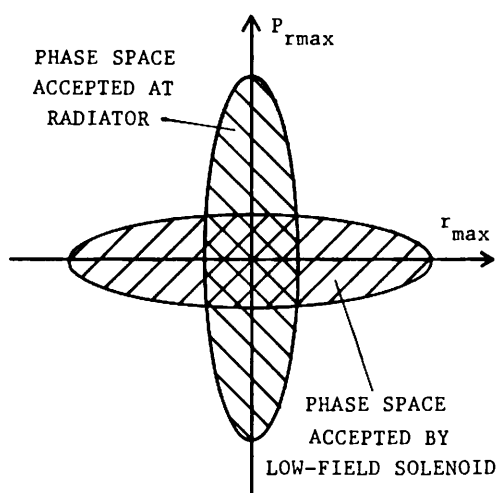


Fig. 3.7 Phase space diagram of the quarter-wave transformer; r : beam radius, P_r : transverse momentum of the positron beam.

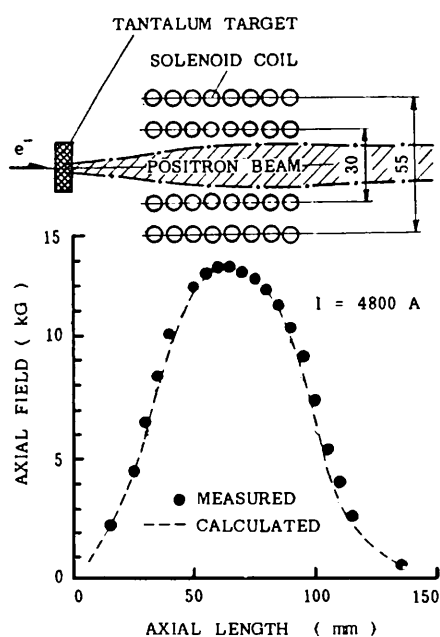


Fig. 3.8 Measured axial field strength along the beam axis, and computed beam envelope of the matched beam.

matched beam calculated for the field distribution shown in the same figure and the beam parameters listed in Table 3.2.

Momentum acceptance of the quarter wave transformer is shown in Fig. 3.9.

Positrons captured with the transformer are focussed and accelerated to about 250 MeV at the end of the positron linac; along the linac 8 sets of triplets and one doublet are placed because of the large emittance of the positron beam.

Table 3.2 Positron beam parameter.

Emittance	$0.15 \pi \cdot \text{MeV}/c \cdot \text{cm}$
Source radius	0.15 cm
Transverse momentum	1 MeV/c
Longitudinal momentum	9 MeV/c

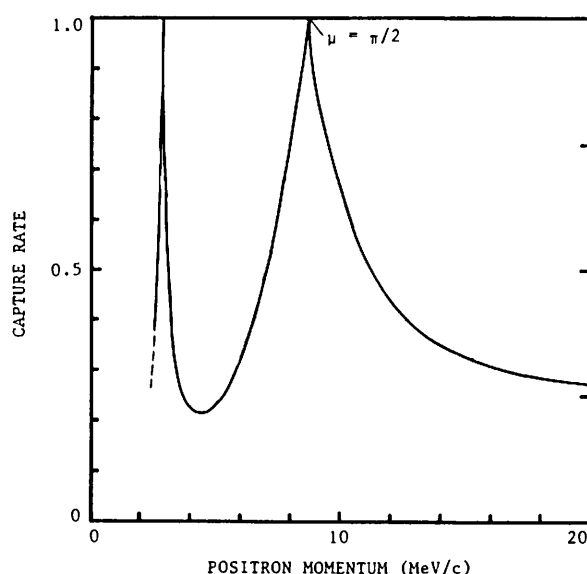


Fig. 3.9 Energy spectrum of the positron beam captured by the quarter wave transformer when the field strength is 12 kG and the effective length is 76 mm.

Beam transport between the positron linac and 2.5 GeV linac

Positrons accelerated to 250 MeV by the positron linac are transferred to the PF 2.5 GeV electron linac at the middle point of the Sector 1, where the electron beam from the gun of the PF linac is accelerated up to the same energy as the positrons. The beam transport line for this transfer is 30 m long, and is composed of two 30° deflecting magnets and quadrupole singlets as shown in Fig. 3.10, which shows also a calculated beam profile along the beam transport line.

Table 3.3 Beam switch yard parameters.

Momentum acceptance	$\pm 4 \%$
Horizontal beam size	50 mm
Vertical beam size	20 mm
Positron beam energy	250 MeV

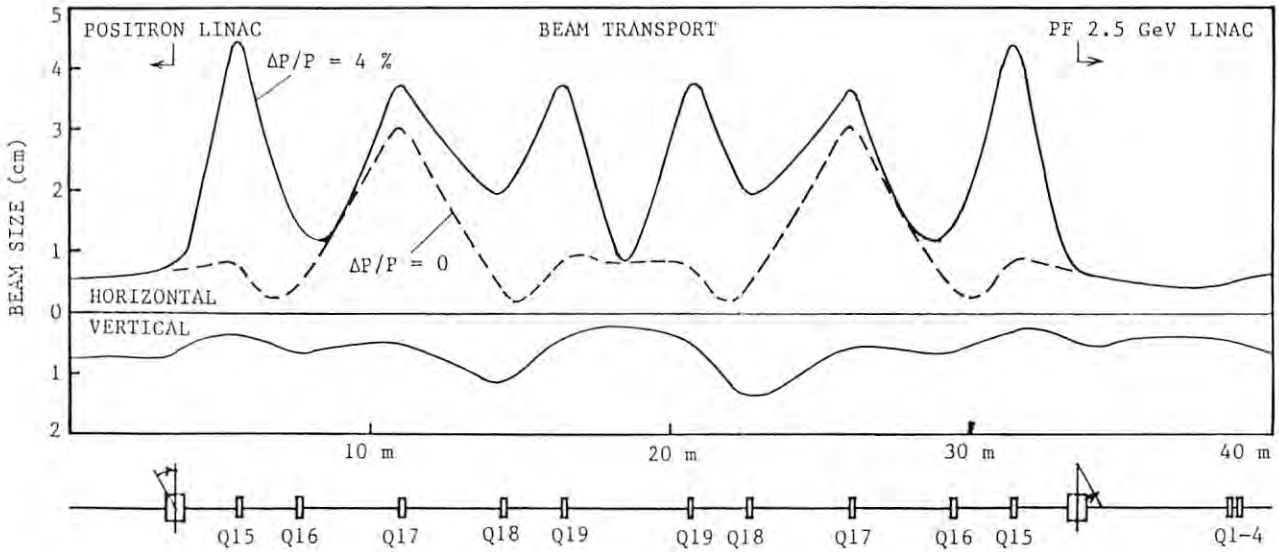


Fig. 3.10 Computed envelope of the positron beam through the beam transport between the positron generator and the 2.5 GeV linac.

Positron focussing elements

The quarter wave transformer installed in the positron generator tunnel is shown in Fig. 3.11.

Tantalum targets with the thickness of 6.2 mm (1.5 r.l.: radiation length), 8.2 mm (2.0 r.l.) and 10.3 mm (2.5 r.l.) are prepared to compare the positron yield; these targets are mounted on a movable holder and can remotely be inserted/extracted to/from the accelerator axis. Beam power loss in the target is about 200 W for the incident beam of 200 MeV, 10 A, 2 ns and 50 pps. These radiators are water-cooled; the temperature rise at the center is calculated to be about 20 degrees for a beam with a 3 mm diameter. The short-range strong field is generated by a 16-turn solenoid. A half-sine pulse of 100 μs, 5000 A is supplied to the coil through two parallel lines using 39D flexible coaxial cable.

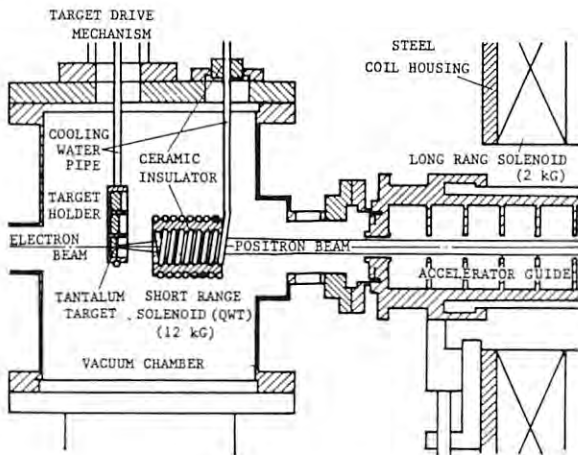


Fig. 3.11 Illustration of the positron source assembly.

The pulse power supply is illustrated in Fig. 3.12. In this power supply, the current oscillates with a frequency given by $\omega = 1/\sqrt{LC}$, where C is the capacitance and L is the load inductance. The output of the power supply is switched on by an SCR during a positive half cycle. The charges are restored slowly through a reactor and a charging diode until the next period starts. The load self-inductance is about 6 μH; therefore, the charging voltage of the capacitor is 940 V for 5000 A. It is regulated to 10^{-3} by the de-Q'ing circuit.

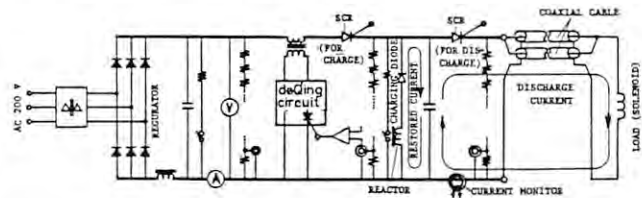


Fig. 3.12 Block diagram of the half-sine pulse generator of 100 μs, 500 A.

The strength of the pulsed magnetic field was measured by integrating an output voltage induced on a pick-up coil. The output voltage of the integrating circuit is given by

$$V(T) = \frac{1}{CR} \int_0^T \frac{\partial \phi}{\partial t}(t) dt ,$$

where ϕ is the flux crossing the pick-up coil. A coated wire of 0.2 mm ϕ is wound 10 turns around the 3.3 mm ϕ acrylic resin bobbin. The schematic diagram is shown in Fig. 3.13; the measurement was performed after the pulsed solenoid was installed in the accelerator. Effective length of the magnetic field was evaluated to be 76 mm by the measurement.

A uniform low-field solenoid with the length of 3.7 m is installed inside a S-10C low-carbon

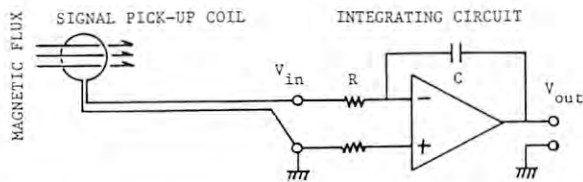


Fig. 3.13 Schematic diagram used for the field measurement.

steel cylindrical housing. The solenoid covers over a 4 m long accelerator guide. The power supply has SCRs and the current is regulated to 10^3 at the full power output: 350 V and 120A.

Beam monitor

To observe the electron and positron beams, many screen monitors and wall-current monitors were installed in the beam line. The wall current monitor is illustrated in Fig. 3.14. The signal from the monitor is amplified 5 times in voltage near the wall-current monitor and

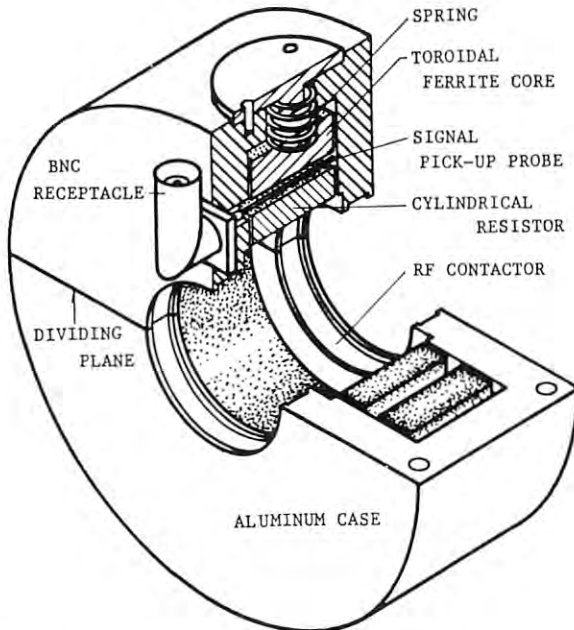


Fig. 3.14 Illustration of the wall-current monitor.

transmitted to the subcontrol station with semiflexible low-loss (13D) coaxial cable. Figure 3.15 shows the typical waveform observed at the subcontrol station for 0.4 mA electron beams.

Positron beam profile was observed by a fluorescent screen coated with zinc sulfide (ZnS). Table 3.4 summarizes the results of the positron beam observation; wall-current monitors were used at the beam pulse width of 10 ns and monitor cameras (10 lux) were used to observe a fluorescence emerged from the screen, typically at the incident beam of 250 MeV, 10 ns, 10 pps and 10 mm in diameter.

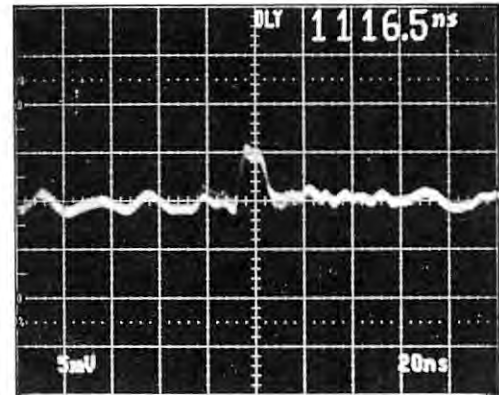


Fig. 3.15 Signal waveform of the electron beam measured by a wall current monitor, located 4.5 m downstream from the radiator.

Table 3.4 Sensitivity of positron beam monitors.

beam current	0.1 - 0.2 mA	0.5 mA	2.3 mA
Wall current monitor with amplifier	comparable to noise	output voltage 7.1 mV	output voltage 3.3 mV
Chromium activated aluminum ceramics (Desmarquest AF995R)	invisible	invisible	invisible
Fluorescent screen (zinc sulfide ZnS)	invisible	visible	clearly visible

3.3 Accelerator guides

The construction of all the acceleration units for the positron generator had completed in the end of March 1985. These units are composed of accelerator guides (9 long (4 m long) guides and 5 short (2 m long) guides), rectangular waveguides, vacuum manifolds, ion pumps, beam ducts, alignment equipment and supporting stands. Figure 3.16 shows the units installed in the tunnel. Measurements of phase errors for all of the tunnel. Measurements of phase errors for all of the accelerator guides were performed. The result is successful and the error is enough less than the allowable value. Figure 3.17 shows typical phase errors of the 4 m guides.



Fig. 3.16 Acceleration units installed in the positron generator tunnel.

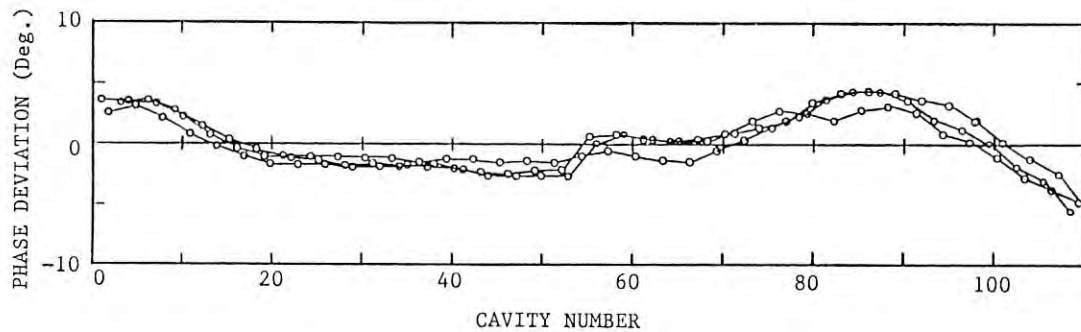


Fig. 3.17 Typical phase errors of the 4 m long accelerator guides.

3.4 Microwave source

The coaxial cables for feeding rf power to each klystron were installed in the klystron gallery of the positron generator. All the I&A units were also installed in the klystron modulators and the output power from the drive line was measured. It was enough for driving the high power klystron.

The electromagnets are used to focus the electron beam in the klystrons for the positron linac, because of the requirement of higher rf output power than that of the PF linac klystrons for which permanent magnets have been used. The electromagnet has a cylindrical shape and a total length of 474 mm with an inner diameter of 195 mm (including the space for X-ray shield of lead). This size was determined by taking account of easy assembly. The outer diameter is about 470 mm and the total weight is about 600 kg. They are composed of 9 coil segments (including the field shaping coil around the gun region), usually some of them are connected in series. They were designed so as to produce a magnetic field more than 1,200 G. They are water-cooled and their associated DC power supplies are interlocked by thermal sensors installed inside them. Figure 3.18 shows a cutaway view of the electromagnet.

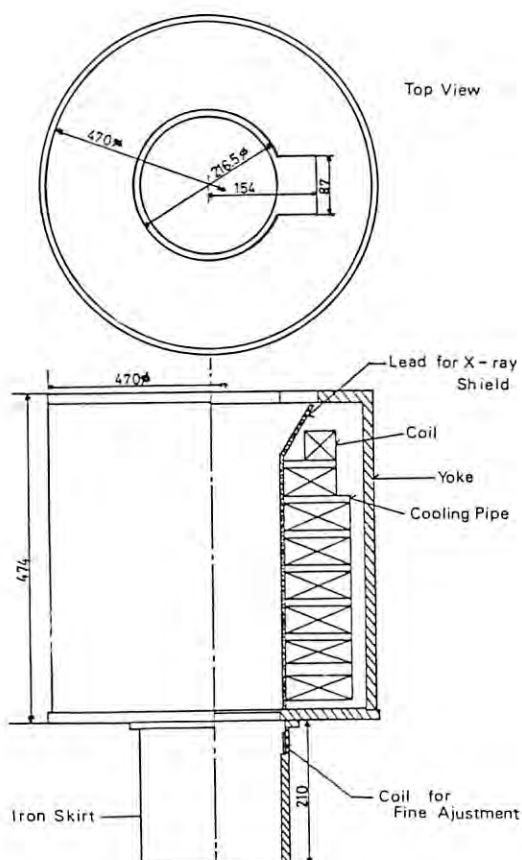


Fig. 3.18 Cutaway view of the electromagnet.

A proto-type magnet was fabricated in June 1984 and the test was made from July to August. Six electromagnets were delivered at the end of fiscal year 1984. Seven DC power supply units, which were stabilized and had remote control units, were also delivered at the same time.

Klystron performance tests using the electromagnets were done from February to March 1985. The manufacturer of the klystron had tested using only an electromagnet; on the other hand, all the klystrons for the PF linac have been operated using only the permanent magnets. Therefore, it was a good chance to compare the data measured at the KEK with those at the manufacturer. The results of the 6 klystron tests showed that the rf output powers of almost all klystrons reached to the design value of 30 MW. Slight difference between the results obtained at the KEK and the manufacturer was found at the optimum magnetic field. Although two of them showed some instabilities due to the effect of higher harmonics generation, with some adjustment of the field the instability was eliminated. Table 3.5 shows a result of the test. The average rf output power with the electromagnet (nearly 30 MW) was higher than that using the permanent magnet because the magnetic field of the electromagnet had good axial symmetry and the field could be easily adjusted during the test.

After the test six klystron assemblies were installed in the positron klystron gallery, and processing of the accelerator guides was performed in the middle of April. It took about a week.

During the test of the beam acceleration, the microwave source has worked satisfactorily without any serious troubles. Total operation time of the klystrons up to July 1985 was about 600 hours.

Table 3.5 Result of the klystron test for the positron generator.

No.	Output Power (MW)	Applied Voltage (kV)	Remarks
P1	32.7	260	
P2	31.0	260	
P3	29.0	260	Instability was observed.
P4	29.5	260	
P5	31.2	260	
P6	27.7	261	Instability was observed.

3.5 Control

Multiprocessor network

The positron generator is controlled by a distributed microprocessor network. Many microprocessor-based device controllers and a subcontrol station are interconnected through fiber optic communication loops. The communication system for the positron generator is the same as that for the PF linac; however, both subcontrol stations of the positron generator and the PF linac are much different from each other.

The new subcontrol station is composed of a system control processor and a local operator's console. A block diagram of the subcontrol station is shown in Fig. 3.19. The system control processor is constructed using a multiple single-board-computer (SBC) crate and two 8-bit SBCs connected to two CAMAC crates via auxiliary crate controllers. Each SBC executes a single task. This makes the system architecture very simple; no complicated operating system is needed. The real-time programs for SBCs are written in a PL/I-like language; the program size for each SBC is 3 - 10 kBytes. The SBCs can intercommunicate via common memories contained in the multiple-SBC crate and the CAMAC crates.

The local operator's console is constructed using five sets of personal computers (FM-11). Procedures for the positron generator control are written in BASIC and run under a BASIC interpreter. This makes change of the control procedures very flexible. Figure 3.20 shows the local operator's console.

The network service for the positron generator control started at the end of March 1985.



Fig. 3.20 Local operator's console of the positron generator.

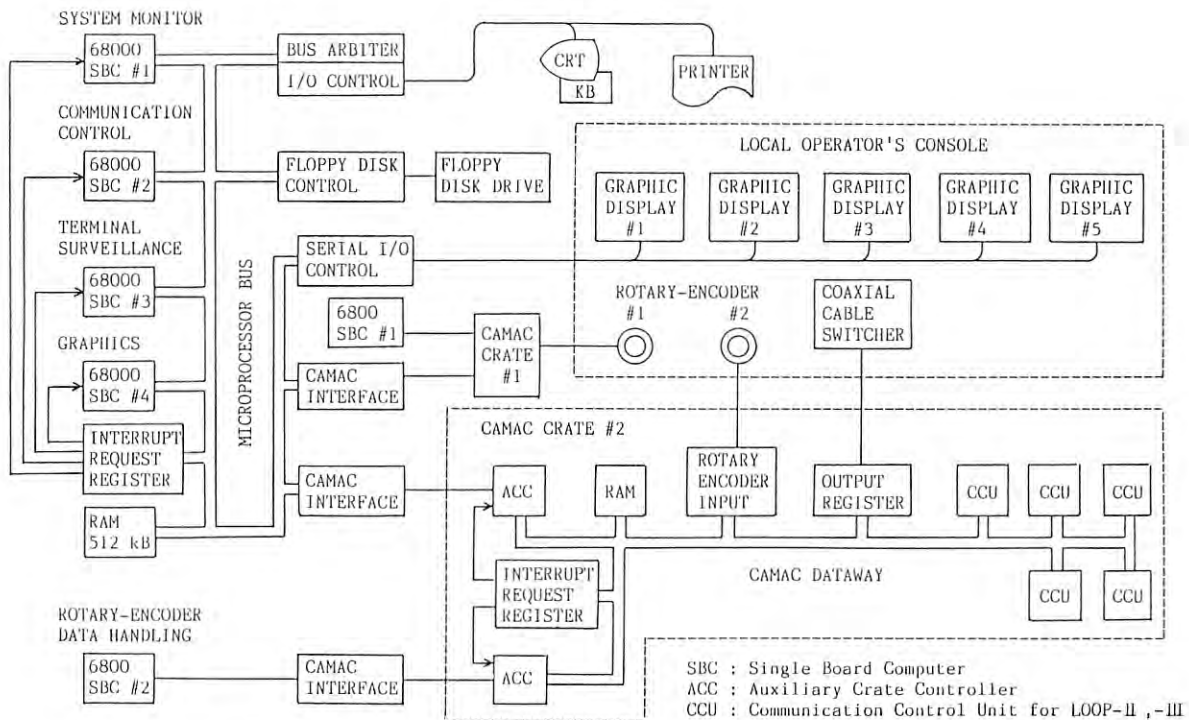


Fig. 3.19 Block diagram of the subcontrol station of the positron generator.

Safety interlock system

The safety interlock system of the positron generator works independently of the other control system. This system is composed of keep-relay modules, relay logic modules, an audible alarm generator, a control panel and a personal computer to display safety signal status. A block diagram of the system is shown in Fig. 3.21.

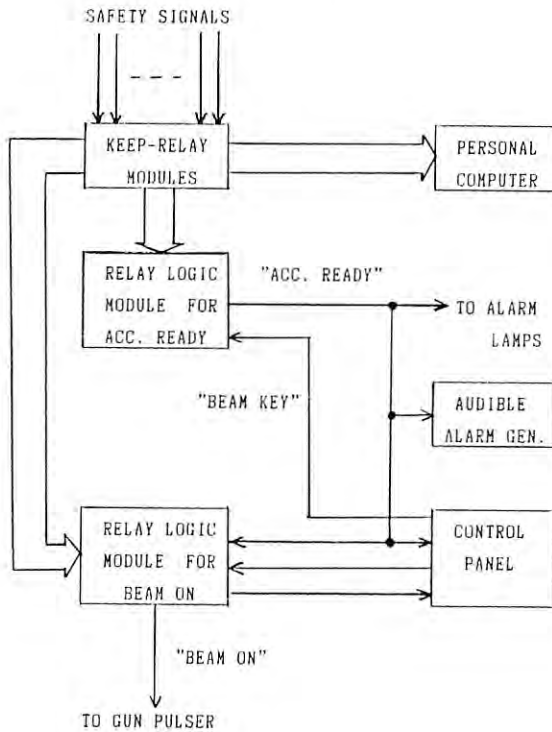


Fig. 3.21 Block diagram of the safety interlock system of the positron generator.

The safety signals are as follows:

- (1) Closing signals of 7 entrance doors to radiation areas.
- (2) Non-push signals of emergency-off buttons.
- (3) A normal signal of a radiation area monitor.
- (4) A no-stayer signal in the entry-prohibited radiation area.
- (5) A ready signal of the 2.5 GeV linac.

Only when all of these signals are normal, beam acceleration in the positron generator can be permitted.

The personal computer FM-11 reads these signals through a digital input module, and displays each status on a CRT with a color of green or red corresponding to "NORMAL" or "ABNORMAL", respectively. Any change of status is printed out with the date and time. An example of the display on the CRT is shown in Fig. 3.22.

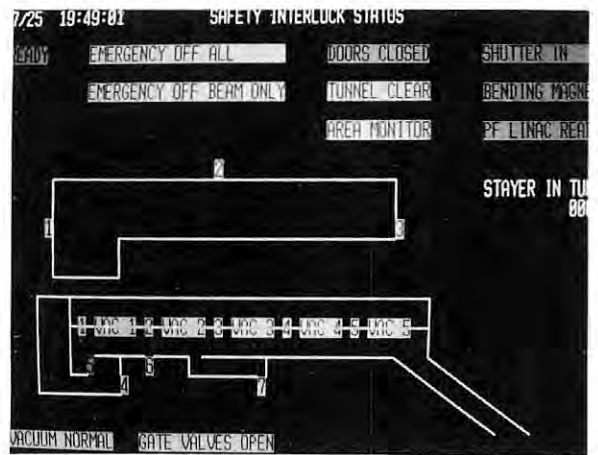


Fig. 3.22 An example of the safety signal status display on a CRT.

3.6 Test operation

The rf conditioning of the accelerator guides and waveguides began in the middle of April and finished after a week. On the way of the conditioning, an abnormal discharge occurred in an accelerator guide of the acceleration unit #4. This accelerator guide was located just downstream from the positron production target and entirely surrounded with a focussing solenoid coil. This discharge arose at the rf power of 5 MW, and did not vanish for a slight power decrease. Owing to this accident, a test operation for the positron generation could not be tried, though an electron beam acceleration was performed for a week in the end of the April.

Acceleration of electron beam

In the early stage of test operation, a long pulse beam of 0.6 μ s was used because a beam loading effect observed in the rf monitor makes the rf phase adjustment easier. The current injected from the gun was about 150 mA.

With this beam, all of the rf phases, i.e., those of the prebuncher, buncher and all acceleration units, were tuned, and the transport magnets such as focussing solenoids, quadrupole magnets, and steering coils were adjusted. As a result of the adjustment, the beam current of 60 mA was obtained at the end of the generator with an estimated energy of 370 MeV.

After the test the failed accelerator guide was removed and inspected. A damage due to the electrical breakdown was observed on an internal surface of the guide, which might be caused by a very small piece of metal left in the guide. After repairing this guide, it was installed again in early July.

Acceleration of positron beam

In July the test operation of the positron generator resumed. The pulse width of the electron beam was chosen to be about 10 ns to make the test easier, although this was wider than the designed value (<2 ns). The beam current injected from the gun was about 3.5 A; by tuning the accelerator, a beam current of 1.7 A was achieved at the positron production target. Figure 3.23 shows the beam current distribution along the linac. Most of the current decreases between the current monitor #1 located just after the gun and the monitor #2 after the buncher was caused due to the finite capture efficiency of the buncher.

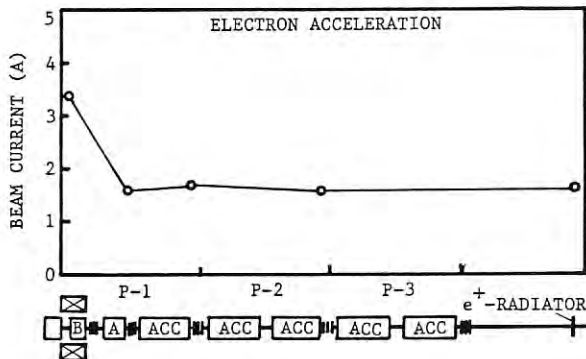


Fig. 3.23 Electron beam current distribution from the gun to the positron radiator.

Before producing positrons another test was made in the following way: The electron beam was accelerated gradually up to 250 MeV to simulate positrons. With this beam, tuning was carried out for the latter half of the positron generator and the 30° deflection beam transport line between the generator and the PF linac.

Then the positron production target was put into the beam line and positrons were searched in the following way. At first, profile monitors were used but found out to be no use. Next, a wall-current monitor was installed at the middle of the unit #5. After the wall-current monitor caught the signal of electron beams (Fig. 3.24), which were the primary beam passed through the target and the secondary one, the rf phases of units #4 and #5 were varied from the electron acceleration to the positron acceleration. Then the electron beam signal was gradually decreased according as the change of the rf phases, and the positron beam signal with an inverse sign appeared (Fig. 3.25). After tuning of the focussing and steering magnets, the positron current reached 2.8 mA at the 200 MeV incident electron beam current of 1.7 A; the ratio of positrons produced to the incident electrons was 0.16 %.

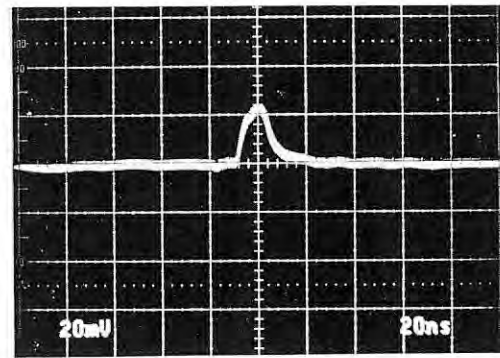


Fig. 3.24 Electron beam current signal (15 mA) from the wall-current monitor, installed at the middle of the unit #5.

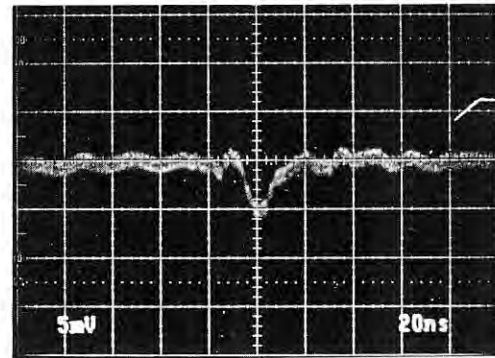
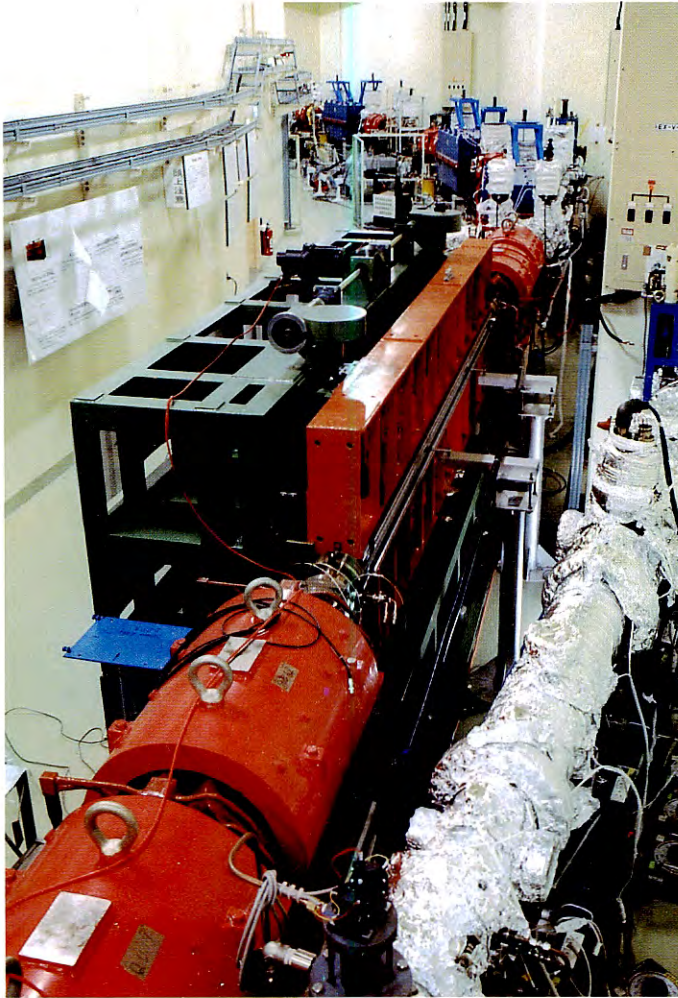
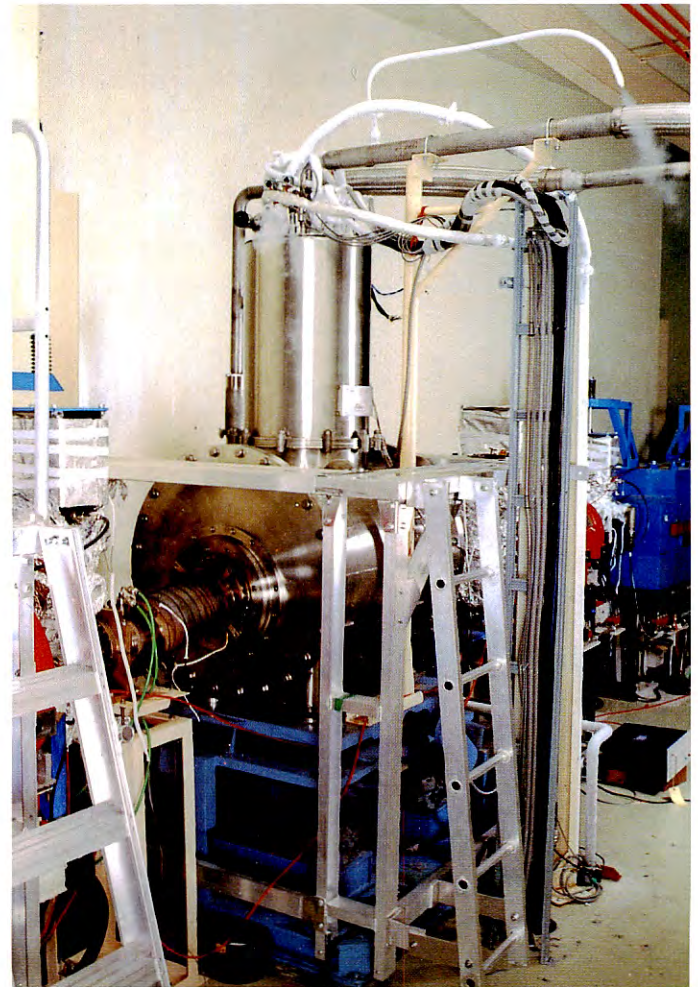


Fig. 3.25 Positron beam current signal (0.35 mA) from the wall-current monitor, installed at the middle of the unit #5.

IV. Light Source Division



Superconducting vertical wiggler. The first operation with electron beam was achieved in February 1983. The maximum operation field in user's time is of 5 Tesla.



Undulator

<i>Magnet material</i>	<i>SmCo₅</i>
<i>Length of a period</i>	<i>6 cm</i>
<i>Number of periods</i>	<i>60</i>
<i>Pole width</i>	<i>9 cm</i>
<i>Range of peak field</i>	<i>3180-190 gauss</i>
<i>Range of K parameter</i>	<i>1.78-0.1</i>
<i>Range of available photon energy</i>	<i>0.4-2 keV</i>

LICHT SOURCE DIVISION

1. INTRODUCTION

The 2.5 GeV Electron Storage Ring which is fully dedicated to the research work with synchrotron radiation was commissioned in June 1982. Since then, the Ring has been well operated over three years. The principal parameters of the Ring and achieved values are listed in Table 1.1. The initial current is still limited to 150 mA because of the heating problem of the vacuum chamber. However, the improvement of the cooling system of the vacuum chamber is progressing during this summer shut down. We are expecting much more initial current in the autumn run.

Table 1.1
Principal parameters of the storage ring

Energy	2.5 GeV
Stored current	achieved range 1.6 ~ 3.0 GeV 150 mA (aimed at 500 mA) max. achieved 250 mA at 2.5 GeV, 520 mA at 2.05 GeV
Mean radius	29.77 m
Radius of curvature	8.66 m
Critical wavelength	0.298 nm
Emitance	horiz. 4.0×10^{-7} m \cdot rad vert. 1.5×10^{-8} m \cdot rad
RF frequency	500.105 MHz
Harmonic number	312
Number of cavities	4
Radiation loss	450 keV/turn with wiggler
Insertion devices	vertical wiggler 5.0 T 60 periods undulator
No. of SR channels	15 (six under construction)
Vacuum pressure	5×10^{-11} torr without beam
Beam lifetime	30 hrs at I = 150 mA
Injection energy	2.5 GeV (Linac)
Injection rate	1 Hz
Injection time	a few minutes

2. STORAGE RING

2.1 GENERAL

In FY 1985, the operational budget is given for 2600 hours instead of 2200 hours in FY 1984. So the two-week mode operation was tried, in which the Storage Ring is operated from Wednesday morning through Saturday morning of the next week, that is, 240 hours continuous operation. During this operation time, 70 % of the time is allocated to user experiments, while the initial eight hours are used for machine tuning and the remaining 64 hours are used for the machine study on both the Linac and the Storage Ring.

2.1.1 Beam Time Statistics

The beam time statistics from FY 1982 to the end of July 1985 (run No.11) is illustrated in Fig. 2.1.1. The net time used for experiments got down to 88 % of the scheduled user time in FY 1984. This is because there was a vacuum leakage through a port of one of the four RF

cavities. The port, which will be used for the insertion of a higher order mode damper, is closed by a blank flange with a finger shaped RF contactor. This contactor was melted by the strong RF field induced in the port. This trouble lost 46 hours of the user time. On the contrary, the machine failure in the run No.11 was just one percent of the total user time, so that the percentage of the net user time increased up to 94.6 % of the scheduled user time.

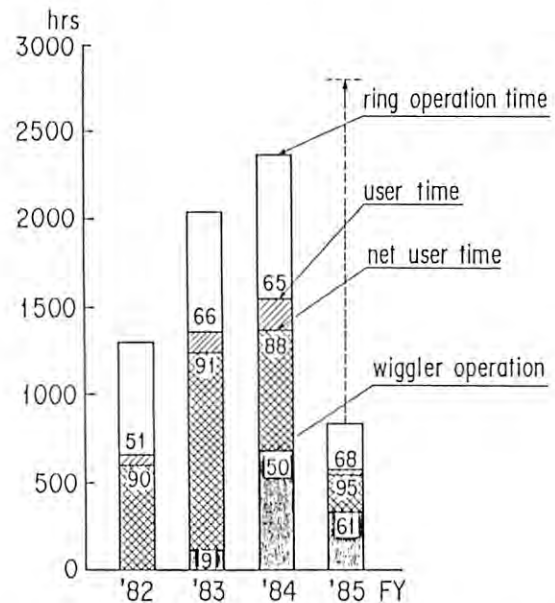


Fig. 2.1.1 Beam time statistics. The number written upper side of the graph means the user time percentage in the total operating time. The second one is the percentage of the net user time in the user time. The third is the percentage of the wiggler operation.

2.1.2 Improvement of Beam Lifetime

As illustrated in Fig. 2.1.2, the run average of the stored current during the user time did not increase through FY 1984. While the initial current was still limited to 150 mA the average stored current in the run No.11, increased up to 115 mA and the average injection interval exceeded over nine hours.

In the runs of FY 1984, we were often bewildered to see figures indicating the lifetime and the vacuum pressure averaged along the Ring, an example of which is shown in Fig. 2.1.3. Just after the injection, the vacuum pressure near the RF cavity No.1 rose up by and by to shorten the beam lifetime and reached its maximum at two hours later and, then, returned gradually to the initial value. In the normal operation, one-third of RF buckets remains empty and other RF buckets are filled nonuniformly with electrons. Such a operation mode is necessary to cure the two-stream instability caused by ion trapping. We observed that, when the filling shape was sharp, the abnormal behavior of the beam lifetime occurred even if the initial stored current reduced to 120 mA as seen in Fig. 2.1.3.

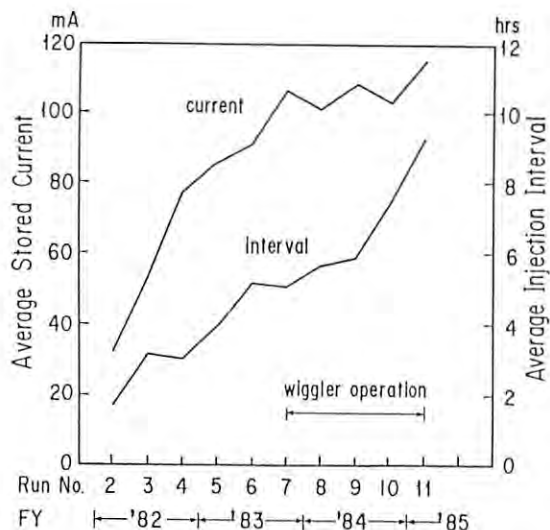


Fig. 2.1.2 Progress of the run average of the stored current and of the injection interval during the user time. The initial current is same, 150 mA, except runs No.2 and No.3.

With this observation and other bench tests of the RF cavity, we got a conjecture that the wake field generated by bunched electron beams invaded, through the narrow space between the tuner and the outer wall, into the rear part of the tuner and heated carbon contactors to cause thermal outgassing. In fact, when the tuner and carbon contactors were baked out, we observed that an amount of water vapour was desorbed. Nevertheless after baking, the abnormal beam lifetime continued. This was because, during baking of the tuner, the cavity and the vacuum chamber near the cavity were not baked sufficiently, so that water vapour again adsorbed on the surface of these parts. Before starting the run No.11, the cavity and the vacuum chamber were baked out and we had a beautiful figure of the beam lifetime and the vacuum pressure as illustrated in Fig. 2.1.4.

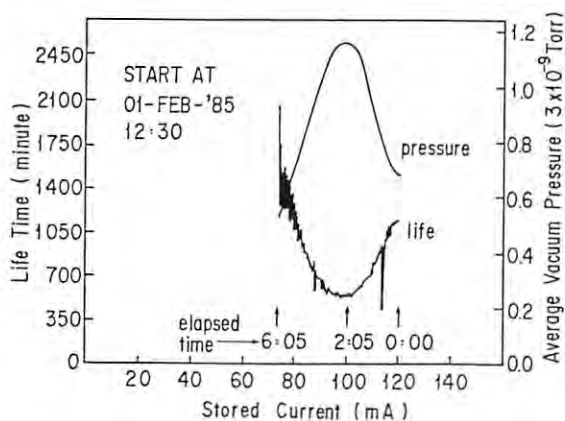


Fig. 2.1.3 An example of the abnormal beam lifetime when the vacuum pressure near the RF cavity No.1 runs over.

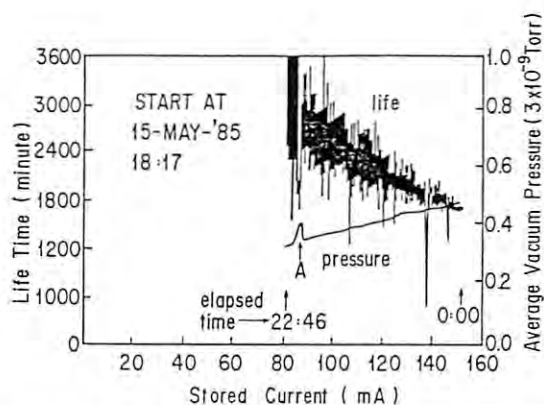


Fig. 2.1.4 The beam lifetime and the vacuum pressure after the vacuum improvement. The pressure bump at A is caused by a miss-operation of the water cooling system.

2.1.3 Low Energy Operation

In February 1985, the low energy operation was tried to study the Ring performances in the energy range from 1.6 GeV to 2.5 GeV. In this experiment a high current of 520 mA could be stored at 2.05 GeV. The current limit was due to an instability occurred in one of the klystrons. At this current the longitudinal coupled bunch instability became stronger than in the normal operating conditions, but transverse coupled bunch instabilities were not observed as expected, since the Ring was operated under transversely stable conditions. The beam size was enlarged with the beam current. It seems that the brightness of synchrotron radiation saturates when the stored current exceeds 100 mA. The beam lifetime at 450 mA was 200 minutes which was mainly due to the vacuum pressure and an effect of the large longitudinal instability.

2.1.4 Wiggler Operation

The operation system of the superconducting vertical wiggler has been computerized except for the filling system of liquid helium into a large dewar which is connected to the wiggler cryostat. The field strength of the wiggler in the routine operation was improved to rise up to 5 T, and the wiggler operating time became 61 % of the total user time. The beam lifetime during the wiggler operation has been steadily increased throughout the year, owing to continuous machine studies including a search for a proper operating point, an use of octupole magnets and a fine adjustment of the position of the wiggler. Now it is 15 hours at the stored current of 150 mA, which is about a half of the lifetime without the operation of the wiggler.

2.1.5 Summary of Storage Ring Developments

Reduction of coupled bunch instabilities: Three coupled bunch instabilities caused by higher order mode resonances of the cavity have been observed in the Storage Ring. These parasitic mode frequencies shift as cavity

temperature changes. So a new temperature regulation system of cooling water for cavities was installed to cure instabilities.

Stabilization of the transverse beam instabilities by octupole magnets: Six octupole magnets with an integrated strength of $200 \text{ T/m}^2 \cdot \text{A}$ per magnet have been installed at diametrically symmetric point of the Ring. In the routine operation, these octupole magnets are used with a current of 3 A and both of the vertical instability caused by ion trapping and the horizontal instability caused by a deflecting mode of the RF cavity has been fairly suppressed at least below 150 mA of the stored current.

Observation of bremsstrahlung: Using a lead glass Cerenkov counter, we have continuously monitored bremsstrahlung coming out of the beam position at the curved section of a bending magnet. It was found that a burst of bremsstrahlung yield was closely related to a short lifetime mode in which the lifetime suddenly became shorter though there was no change in the measured value of the vacuum pressure. There are many speculation about this phenomenon, but further study must be necessary. The two-beam instability caused by ion trapping was also studied using the bremsstrahlung measurement and we could observe the time rate of ions trapped by electron bunches.

2.2 MEASUREMENT OF BETATRON FUNCTIONS

The betatron function is one of the fundamental quantities characterizing the motion of particles in the storage ring. Therefore, measurement and comparison with theoretical values of actual betatron functions around the ring is useful to confirm performance of the storage ring.

There are two methods of measuring the betatron function; the orbit deformation method and the quad shunt method. The orbit deformation method is that the closed orbit deformation is measured at every location of position monitor, when a steering dipole is excited to produce a certain amount of deflecting angle. It is necessary, however, to assume the phase advance between the steering dipole and the position monitor, to reduce to values of the betatron function from the measured closed orbit distortions. Therefore, the orbit deformation method has not been adopted in the present experiment. The quad shunt method is the one that has been commonly adopted. If the strength of a quadrupole magnet is changed by shunting the quadrupole magnet current, the betatron frequency shifts by $\Delta\nu$ according to the following relation

$$\Delta\nu = \frac{1}{4\pi} \int \beta(s)k(s)ds,$$

where k is a perturbation of the focal constant K at the azimuthal position s with $K = (1/\beta) \frac{d^2\beta}{ds^2}$. $\beta(s)$ is the betatron function at the location of s . If we assume that the betatron function is constant over the quadrupole magnet, one can estimate the value of the betatron function at the position of the quadrupole by measuring the change in the betatron tune when the perturbation k is applied. Calibration of the integrated field gradient versus current for quadrupole magnets has been done in advance.

Ambiguity in the absolute value of calibration is of the order of 1 percent.

The shunt circuit actually used in the present experiment is the electronic shunt circuit which is commercially available as the general purpose equipment for testing power supplies. It has a capability of shunting a power loss of up to 300 W in the electronic shunt.

The measurement of the betatron function has been done at the rather small stored current of 20 mA, because the tune spread becomes wider at larger currents. Sextupole magnet currents were set zero during the experiment. But octupole magnets that are normally used for providing Landau damping were excited with 0.5 A, because the vertical instability occurs without them. For a change in the quadrupole current of 10 A, the change in the betatron oscillation frequency is about 20 kHz for $\beta \sim 10 \text{ m}$. Since a measurement error of the betatron frequency is about 0.1 kHz, the estimated error of the betatron function is around 0.1 m.

Results of the measurement are shown in Fig. 1. In the figure are also shown the theoretical values. The Photon Factory storage ring has the superperiodicity of two, and each superperiod has a symmetry point at the middle. As seen in Fig. 2.2.1, symmetry of the betatron function is preserved in the actual ring.

When the vertical wiggler is excited, however, it is expected that symmetry of the betatron function around the ring must be broken because of an introduction of local gradient error due to the wiggler magnet. As described in the Photon Factory Activity Report 84/85, the tune shift is generated when the wiggler magnet is excited. Since the vertical wiggler is essentially a set of rectangular magnets where the magnetic field lies in the horizontal direction, the horizontal tune should change when the wiggler is excited. Actually, the vertical tune also changes because of sextupole field component existing in the wiggler magnet. Effectively, there are field gradient errors in both horizontal and vertical directions at the location of the vertical wiggler. Although it is desirable to compensate the gradient error locally by additional quadrupoles localized nearby, the tune shift is at present compensated by changing the strength of the focusing and defocusing quadrupoles in the normal cells. As seen in Fig. 2.2.2, there is a large amount of beat in the betatron function around the ring. The distortion of the betatron function ($\Delta\beta/\beta$) in the existence of field errors can be estimated if the field gradient error is identified. For a localized gradient error, the curve of $\Delta\beta/\beta$ around the ring shows a pattern whose principal harmonic is twice of the betatron tune. The solid lines shown in Fig. 2.2.2 represent the theoretical curves estimated in this manner.

Effects on the beam dynamics of the distortion of the betatron functions have not yet clarified. Experimentally, the stable region in the tune diagram becomes narrower in the operation of the wiggler compared with that of without the wiggler. To identify the reason of the lifetime shortening in the operation of the wiggler, it is intended to compensate the gradient error locally by shunting the current of two nearby quadrupole magnets (Q142 and Q143).

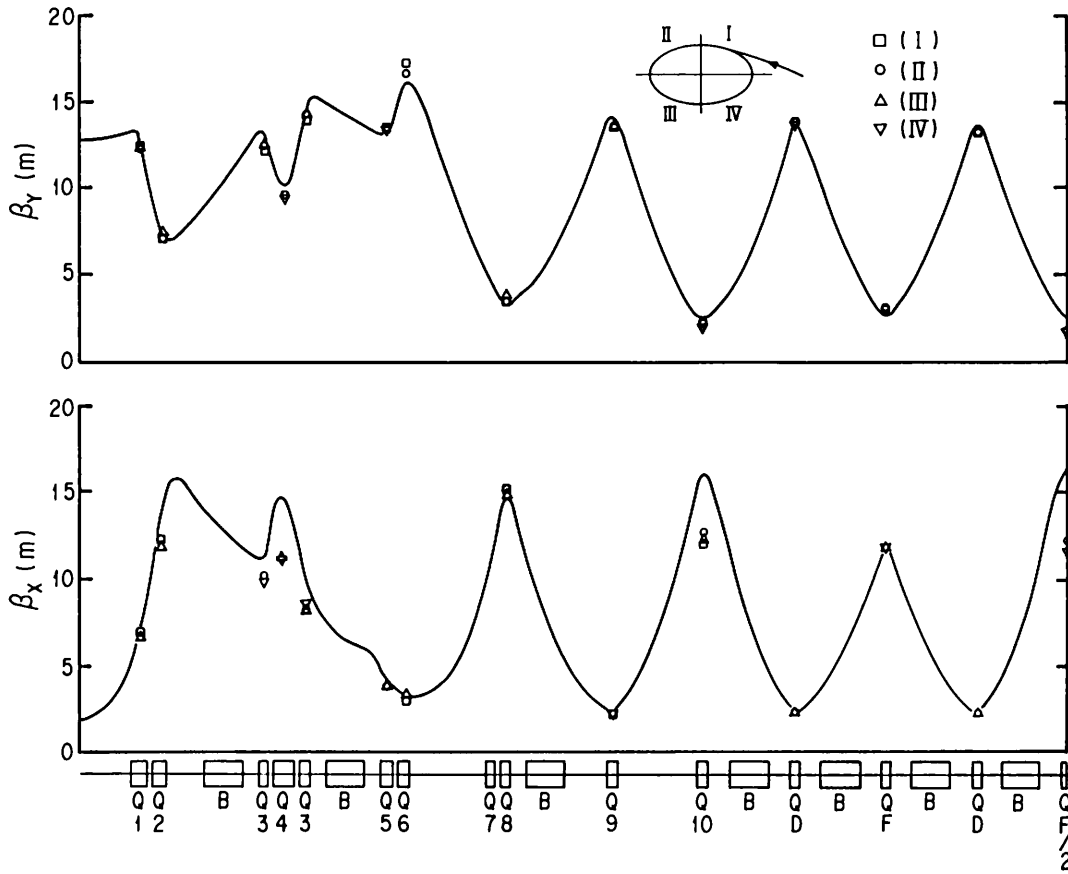


Fig. 2.2.1 Results of the measurement of betatron functions.

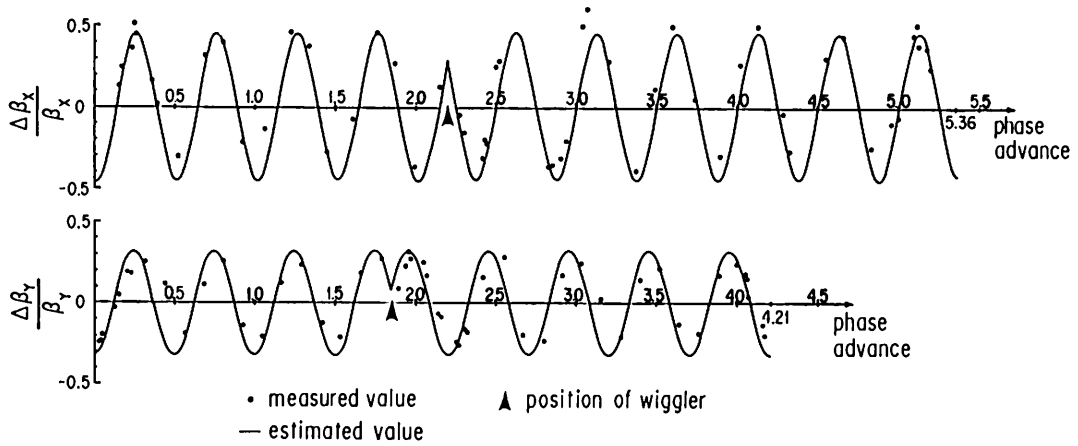


Fig. 2.2.2 Distortion of the betatron function ($\Delta B/B$) in the existence of field errors.

2.3 BEAM INSTABILITIES

2.3.1 Coupled-Bunch Instabilities and Cavity Temperature Control

As reported in the last year's Activity Report, three types of coupled-bunch instabilities have been observed in the Photon Factory storage ring. All these instabilities have been known to be caused by higher order mode resonances of accelerating cavities. Although the resonance width of each higher order mode is narrow, the resonant frequency is different for different cavities due to mechanical tolerances of each cavity. The resonant frequency also depends on the temperature of the cavity. Therefore, if the temperature of each cavity is changed independently, the frequencies of higher order modes can be shifted so as to avoid hitting resonances and to make the threshold current higher. For this purpose, a temperature regulation system of cooling water for accelerating cavities was installed during the summer shutdown of 1984. It can regulate temperature of inlet water for each cavity from 15 to 25°C with a stability of 1°C.

We have intensively studied how the resonant frequencies change with cooling water temperature, and tried to find the optimum set of temperature for four cavities. Figure 2.3.1 shows the dependence of the threshold current of the longitudinal instability on water temperature. The longitudinal instability is caused by the TM₀₁₁-like mode of the cavity with the frequency of 758 MHz. By changing temperature of each cavity and taking the dependence of the threshold current on the accelerating frequency, we could identify where the resonant frequency of each cavity is. It can be seen from Fig. 2.3.1 that, at the present operating frequency, dangerous cavities are No.2 and No.3, and the threshold current of the instability can be raised appreciably by raising the water temperature for these cavities. It should be noted, however, that this longitudinal instability does not lead to beam drop-out, but leads to horizontal blow-up. When the vertical wiggler is in operation, the lifetime becomes short, because of the narrow horizontal aperture in the wiggler.

Figure 2.3.2 shows the dependence of the transverse instabilities on water temperature. The transverse instabilities are caused by the TM₁₁₁- and TM₁₁₀-like modes whose resonant frequencies are 1070 and 830 MHz, respectively. As seen in Fig. 2.3.2, the resonant frequency for the TM₁₁₁-like mode shifts to higher values when the water temperature becomes high, while the resonant frequency for the TM₁₁₀-like mode shifts to lower values. As the results, the threshold current of the transverse instabilities at the present operating tune becomes low if water temperature for all cavities is 25°C. Since the beam current drops by occurrence of the transverse instabilities, they should be avoided

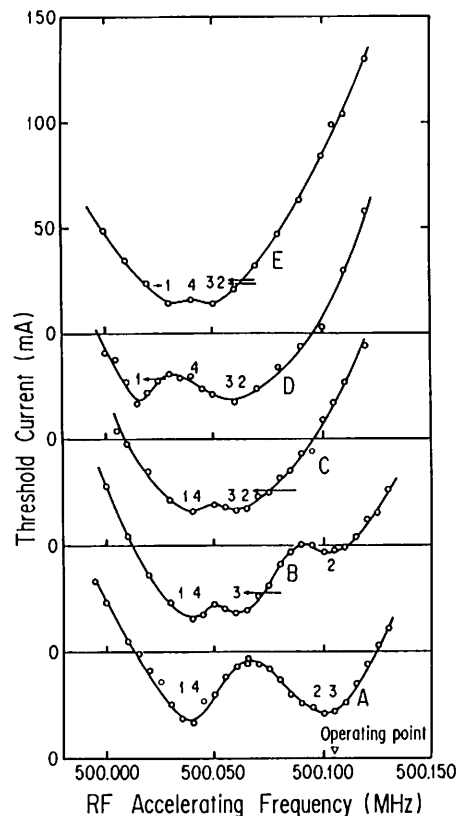


Fig. 2.3.1 Dependence of the threshold currents of the longitudinal coupled-bunch instability on the RF accelerating frequency. The threshold currents were also measured by changing water temperatures for each cavity independently. Numbers 1 to 4 represent the cavity numbers. Temperature sets for cavities 1 to 4:

- A = (20,20,20,20)°C,
- B = (20,20,25,20)°C,
- C = (20,25,25,20)°C,
- D = (25,25,25,20)°C,
- E = (20,27,27,20)°C.

by choosing proper values of betatron tune and water temperature.

As seen in Fig. 2.3.1, temperature for cavities should be high for the longitudinal instability, but low for the transverse instabilities. In actual operations to compromise between these. We choose a proper set of operating temperatures and the value of horizontal betatron tune. In this way we have avoided the transverse coupled-bunch instabilities, and made the threshold of the longitudinal instability two times higher.

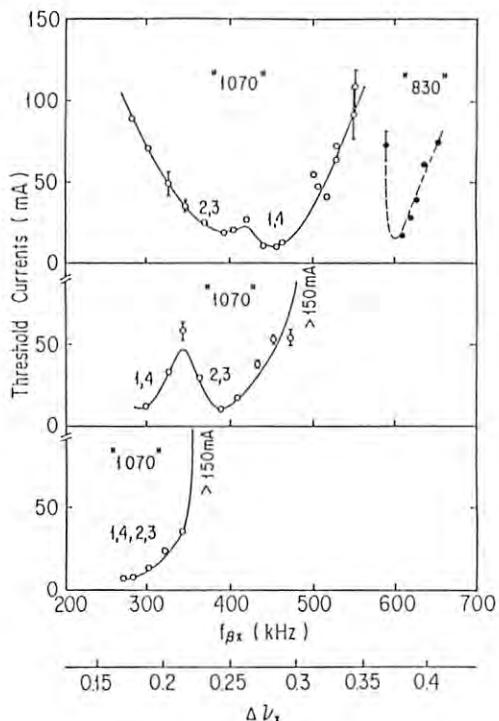


Fig. 2.3.2 Threshold currents of the horizontal coupled-bunch instabilities. Measurements were carried out at various temperature sets of cavity cooling water. From the top to the bottom in the figure, temperature sets are (25,25,25,25)°C, (20,25,25,20)°C and (20,20,20,20)°C.

2.3.2 Longitudinal Coupled-Bunch Instability and Slow Bunch Length Oscillation

Frequency spectrum of reflected power from the cavity

When the longitudinal coupled-bunch oscillation is initiated, the frequency component at $f_{161,1}^+$, which is very close to the resonant frequency of the TM011-like mode of the cavity (758.23 MHz), is observed in the frequency spectrum of the reflected power from the cavity as shown in Fig. 2.3.3. $f_{\mu,n}^{\pm}$ is the frequency characterizing the coupled-bunch oscillation and is defined as

$$f_{\mu,n}^{\pm} = nBf_r \pm (\mu f_r + m f_s),$$

where n is positive integer including zero, B the number of bunches, μ the mode number of the coupled-bunch oscillation. The strongest sideband appears at $m = 1$, indicating that the predominant mode is dipole. In contrast to the signal from the beam position monitor, no peak at $f_{161,n}^-$ is observed in the frequency spectrum of the reflected power, because the reflected power

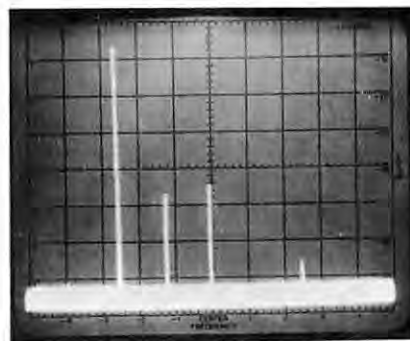


Fig. 2.3.3 The frequency spectrum of the reflected power from a cavity. The center frequency and the scan width are 1000 MHz and 200 MHz/division, respectively.

includes solely effects of the impedance of the cavity. The impedance at $f_{\mu,n}^+$ contributes to growth of the longitudinal oscillation, while $f_{\mu,n}^-$ contributes to damping.

Fluctuations of the beam width and the bunch length

In the last year's Activity Report we reported that the amplitude of the longitudinal coupled-bunch oscillation, which is the $f_{161,1}^+$ component normalized by the fundamental frequency component, grows fast at the threshold current of the instability, but saturates at the certain value. As shown in Fig. 2.3.4, both the horizontal beam size and the bunch length begin to increase at the threshold current. The reason of bunch lengthening is not a single bunch effect, since the threshold current of turbulent bunch lengthening should be higher than the present value. Instead, it is thought to be due to the dipole oscillation of a bunch in the rf bucket which leads to incoherent bunch lengthening for the sake of the non-linear property of rf fields. The horizontal beam size also grows up along with bunch lengthening because of non-zero dispersion at the source point of observed synchrotron radiation. The beam size fluctuation with a frequency of about 200 Hz, which was described in the previous Activity Report, has been recognized to be a result of bunch length fluctuation with the same frequency.

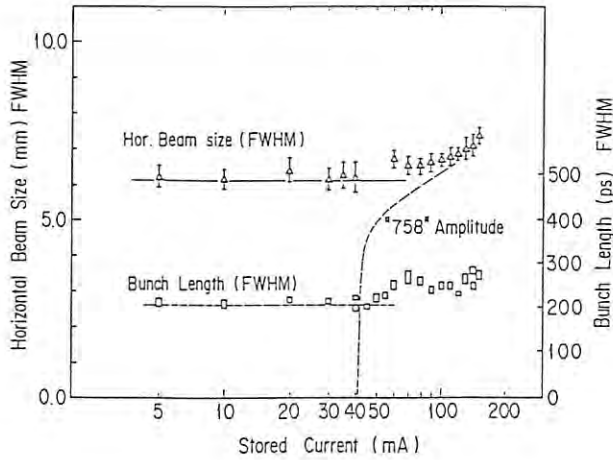


Fig. 2.3.4 Beam size and length as a function of the stored current.
 Triangles: Horizontal beam size (FWHM).
 Rectangles: Bunch length (FWHM) measured with the streak camera.
 Dashed curve: Amplitude of $f_{16,1}^+$.

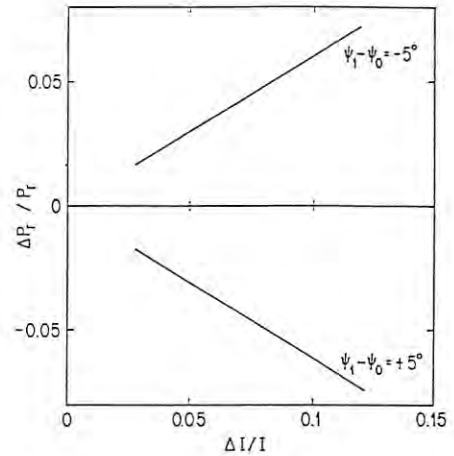


Fig. 2.3.5 Reflected power from RF cavity for two tuning angle settings.

Bunch length oscillation observed in the reflected power

The bunch length oscillation can be observed as an amplitude modulation of the reflected power of the fundamental mode (500 MHz), if it is faster than the response time of the tuner. Suppose that bunch lengthening takes place and the effective current of the fundamental mode is changed by ΔI . The reflected power of the fundamental mode is a function of the tuning angle ψ_1 of the cavity, and decreases as ΔI when the tuning angle ψ_1 is greater than the optimum angle ψ_0 for the resistive cavity, and vice versa. Figure 2.3.5 is an example of calculated values of the reflected power change in the cases of $\psi_1 - \psi_0 = \pm 5^\circ$. From these calculations it is expected that the bunch length oscillation will induce the amplitude modulation of the reflected power from the cavity.

Observation of the reflected power via band-pass filters

In order to separate the signal induced by the instability from that of accelerating mode, two bandpass filters with frequency bands of 500 ± 10 MHz and 750 ± 10 MHz were used, and signals passing through both bandpass filters were displayed simultaneously on the oscilloscope. Figure 2.3.6 shows waveforms observed in both frequency bands.

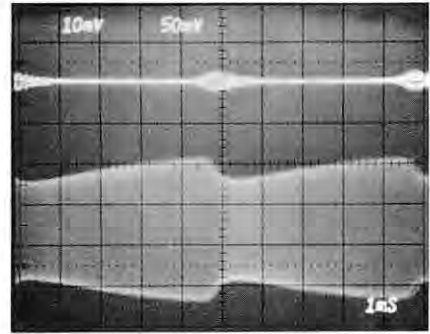


Fig. 2.3.6 Reflected signals in the frequency bands of 750 ± 10 MHz (upper trace) and 500 ± 10 MHz (lower trace).

The amplitude of 758 MHz component blows up and decays repeatedly with the repetition rate of 200 Hz. Correspondingly the amplitude modulation of 500 MHz component, which is related to bunch length oscillation, is also seen.

Phase relation of the amplitude modulation was reversed with the setting of the tuner phase angle ψ_1 . Figure 2.3.7 is an example of changing phase of the amplitude modulation when the tuner setting of the cavity #2 was varied from $\psi_1 > \psi_0$

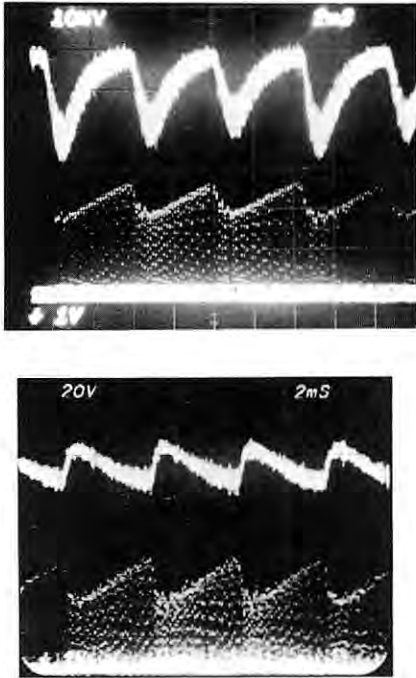


Fig. 2.3.7 Phase relations of amplitude modulation which are reversed by varying the tuning angle. Upper traces of both pictures are envelopes of 500 MHz reflection from cavity #2. Lower traces are horizontal profiles with sweeping time of 2 ms/div, indicating periodic horizontal beam broadening.

$\psi_1 < \psi_0$. In these pictures are also displayed the signal of the horizontal profile monitor as a reference, which shows the instance of the beam blow-up. The 758 MHz signal was not affected by changing the tuning angle of the tuner.

2.3.3 Improvement of the Instability Threshold by Octupole Magnets

Octupole magnets have been installed in the storage ring from October 1984. Aims of octupole magnets are to produce amplitude dependent tune spreads in the betatron frequencies and to stabilize the transverse coherent instabilities such as the transverse coupled-bunch instabilities and the vertical instability due to ion trapping. As expected, octupole magnets were proved to be effective to stabilize these instabilities, and they have been used in the routine operation of the storage ring.

Effects of octupole magnets on the transverse coupled-bunch instability have been investigated, as well as the change of the damping rate of the transverse oscillation with octupole magnet current. We have found that the measured threshold current of the instability agrees well with the calculated one which is obtained by the classical theory of instabilities using the measured damping rate and the measured value of higher order mode impedance of the cavity.

Measurement of damping rate

The transverse beam oscillation was excited by means of the RF knock-out system. The excitation field was applied to the beam with a frequency corresponding to the fractional part of the betatron tune. It was amplitude-modulated by the square-wave pulse. The excitation strength was chosen properly so as not to lose the beam. An amplitude of beam oscillation grows with the RF knock-out and saturates at a certain equilibrium value because of a nonlinear damping effect which depends on the amplitude of oscillation.

When the RF knock-out is turned off, the transverse oscillation starts to decay. The beam oscillation was observed with both the left and right electrodes of the beam position monitor and the quartered photo-diode array. Measured damping rates of the horizontal betatron oscillation are shown in Fig. 2.3.8 as a function of the octupole magnet current.

Effects of octupole magnets on the transverse coupled-bunch instability "1070"

In the measurement of the dependence of the threshold current on octupole magnet current, the operating parameters of the storage ring were set such that the operating betatron tune was just on resonance of the instability and the threshold current became minimum. Under this condition the threshold current was measured as a function of octupole magnet current. The threshold current is defined as the beam current at which a peak appeared in the beam spectrum, indicating the initiation of the coupled-bunch instability. Results are shown in Fig. 2.3.9. The minimum of the threshold current is located at octupole current of -1A, not at 0A, which indicates there is an octupole field component originally in the ring magnet system. The solid curve in the figure represents the threshold current calculated by using the following relation;

$$I_{th} \sim \frac{2\omega_{\beta} E}{\tau_x e c Z f_r} = \frac{1.1 \times 10^{-5}}{\tau_x} \quad (1)$$

with substituting the measured damping rate as τ_x^{-1} . In Eqn.(1) Z is the coupling impedance of TM11-like mode, ω_{β} the betatron angular frequency, f_r the revolution frequency. The

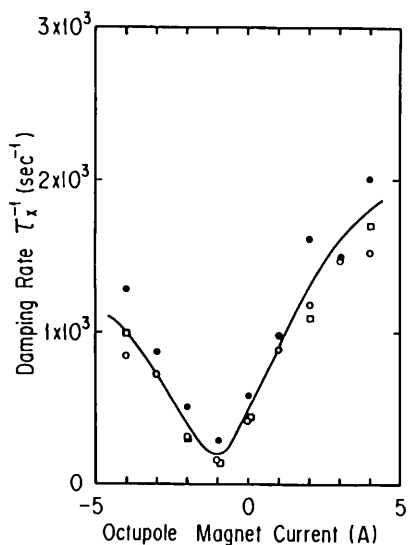


Fig. 2.3.8 Damping rates of the horizontal betatron oscillation as a function of the octupole magnet current. Horizontal and vertical tunes were 5.27 and 4.21, respectively. Temperature set of cavity cooling water was (15,15,15,15) $^{\circ}$ C, sextupole magnet currents were 0A, and stored beam current was 30 mA. The closed circles denote the damping rates measured with the beam position monitor and open circles with the quad-photo diode at $P_c = 89$ kW. The open squares are data taken with the quad-photo diode at $P_c = 116$ kW.

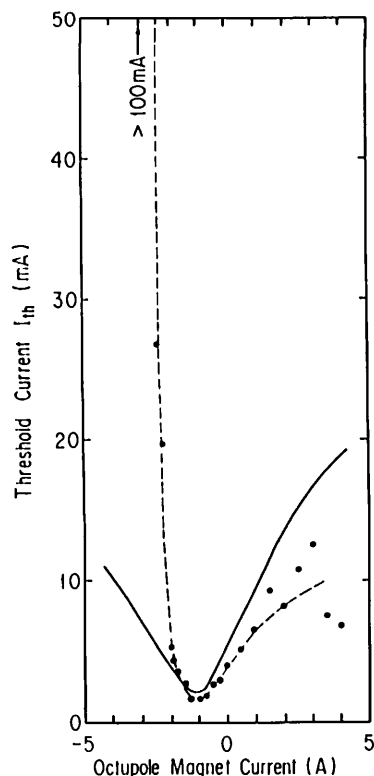


Fig. 2.3.9 Threshold current of "1070" as a function of the octupole magnet current. Betatron tunes are the same as Fig. 2.3.8. The temperature set was (23, 25,25,23) $^{\circ}$ C and $P_c = 116$ kW. Sextupole magnets were all set to 0A. The solid curve denotes thresholds calculated using measured damping rates.

impedance Z is taken to 54 M Ω /m, which corresponds to the coupling impedance for two cavities, since it is reasonable to consider from Fig. 2.3.2 that two cavities are dominant to the instability at the present conditions. ω_{β} is 5.6×10^7 sec $^{-1}$.

The calculated threshold is 2.1 mA which is in good agreement with the above measured threshold minimum. Although agreement is rather poor at large octupole magnet currents, Eq. (1) is considered to reproduce the measured threshold currents.

2.4 IMPROVEMENTS OF VACUUM SYSTEM

2.4.1 Outlines

The vacuum system of the storage ring has been well operated for three years. The average vacuum pressure of 5×10^{-10} Torr has been obtained along with the beam lifetime of 1800

minutes or more at 150 mA, the initial beam current usually stored in the ring. At beam current more than about 150 mA, however, a problem arose that some of the vacuum components were heated up because they were not cooled by water but exposed to incident synchrotron radiation. In this summer shutdown, therefore, absorbers against the synchrotron radiation were inserted into the vacuum chambers in order to shade the components and thereby to protect them from being heated up and then to reduce thermal desorption of gases.

Some other vacuum chambers were also modified to install new octupole magnets and skew quadropole magnets, which would improve the quality of the beam at higher currents.

There are 24 SR exit ports prepared for the beam channels in the ring, of which the 20 exit ports called 'normal' exit ports have the same structure while the other 4 exit ports have different structures. Most of the normal exit ports have been already occupied with beam

channels, but three exit ports among the remains were restricted with regard to the available angular width of the radiation. Therefore, to overcome this restriction, the three B-ducts (the vacuum chambers in bending magnets) were replaced with the newly designed B-ducts with wider exit port that makes available the radiations from the upstream bending magnet.

All the gate valves with elastomer seal were also replaced with metal gate valves to reduce outgassing from them in single bunch operation.

2.4.2 Improvements

Duct absorber

About eighty percent of the vacuum chambers in the ring are made of aluminum alloy and the remains of stainless steel. The aluminum alloy chambers are the extruded ones with passes of cooling water integrated in their walls, but the stainless steel chambers had neither pass nor pipe of cooling water before the improvements. Bellows and flanges were also made of stainless steel because no flange or bellow made of aluminum alloy was available at the time when the vacuum system was designed.

When exposed to intense synchrotron radiation, such a chamber or a component made of stainless steel was heated up and then became a source of thermal desorption of gases. In this summer shutdown, therefore, radiation absorbers called 'duct absorber' have been set into appropriate places so that the downstream chambers and components can be shaded and protected from being heated up by the radiation. The location of an absorber and its depth inserted into the chamber were determined by taking account of both the necessary length of the shadow to protect the incident radiation and the aperture required for the injected beam. The absorbers for the aluminum chambers were made of aluminum alloy and welded directly on the chambers. The absorbers for the stainless steel chambers were made of copper, some of which were brazed directly on the chambers while the others mounted with flanges. All of the absorbers are cooled by water.

Crotch absorbers

Each B-duct has a crotch at its downstream side. The crotch is a fork in the B-duct where the inside wall of the exit port meets the outside wall of the downstream part of the B-duct. Since the radiation intensity at the crotch is at least about eight times higher than that at any other place, the crotch was protected by an absorber mounted in front of it even before the improvement. But this absorber called 'crotch absorber' was somewhat makeshift one, being made of a copper plate that was brazed on stainless steel tubes and cooled by water. As

the beam current increased, the temperature of the copper plate rose up because thermal conductivity was low in the brazed region. Then it turned out that none of the crotch absorbers mounted along the ring were pertinent to storing a beam with much higher current. It also turned out that unnecessary photons of synchrotron radiation went down through the exit port and then impinged on the wall of the beam channel to generate photoelectrons; those generated around a gate valve in the beam channel (the gate valve serves to separate the vacuum of the beam channel from that of the ring) might damage the sealing material (Viton-A) of the gate valve and then cause a small vacuum leak through it.

New crotch absorber was designed to improve its thermal conductivity, the whole of it being made of a copper block instead of being made up of an assemble such as the old one. A water pass bored through the copper block makes it possible to cool the block directly. The new crotch absorber was also designed to reduce unnecessary radiation incident on around the gate valve in the beam channel.

Cooling water system

As many absorbers were added to the vacuum chambers, it followed that the system of cooling water was considerable improved. One of the improvements is that the flow rate of cooling water can be measured by a flow meter with a magnetic rotator, mounted on the return pass of the cooling water. All the flow meters are linked to the interlock system and also their output signals are monitored by a micro-computer.

Modification of some vacuum chambers

The bore diameter of new octupole magnets and skew quadropole magnets was chosen to be 120 mm in order to generate strong fields. At their locations to be installed, however, the chamber width was 152 mm for the stainless steel chambers and 192 mm for the aluminum alloy chambers. Therefore the vacuum chambers at their locations were newly designed to fit them to the new magnets, and installed in the ring in this summer shutdown so that the magnets can be also installed during this autumn run.

The following processes were taken to change the cross sections of the stainless steel and aluminum alloy chambers. Each of the stainless steel chambers was cut down in the middle of it, and then new flanges were welded at both the cut ends to connect a new chamber with a round cross section and its diameter of 106 mm. The new chamber has a cooling water pipe made of copper and also at both ends has transition pieces so as not to increase the chamber impedance.

For each of the aluminum chambers to be modified, a new round chamber was made of aluminum alloy. It also has transition pieces at both ends, and an extruded pass for cooling

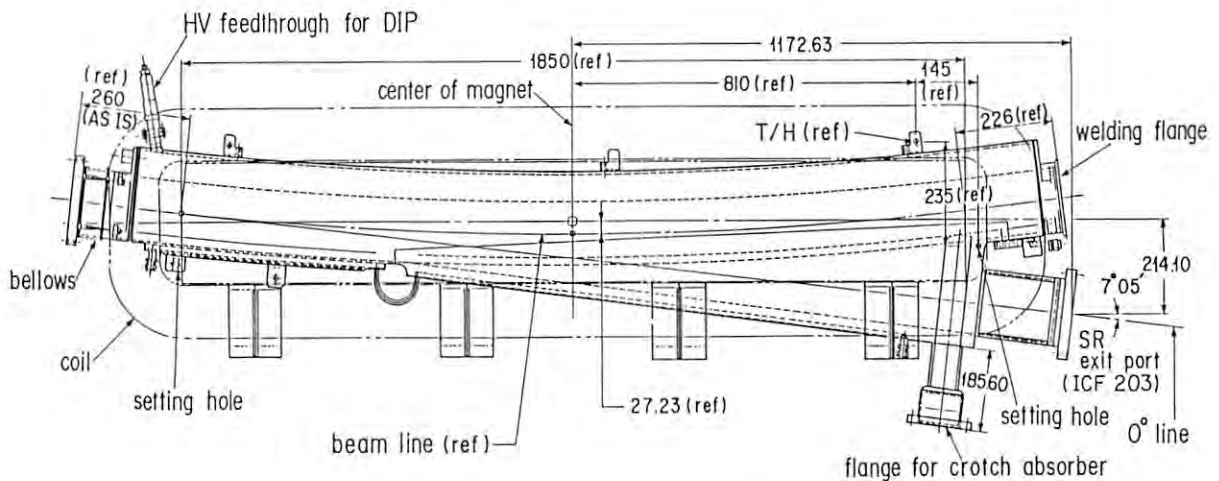


Fig. 2.4.1 New B-duct with wide SR exit port.

water. But in order to avoid the water pass to interfere with the magnet, the new chamber was designed to be set 4 mm shifted from the central orbit. Then the old chamber was cut down in the middle of it in the same manner as the stainless steel chamber, but in this case the new one was welded directly on the old one at both the cut ends.

B-duct with wide SR exit port

The center of the normal exit port is on a line called '2.5 degree-line': the line is a tangent to the central orbit at the point of 2.5 degrees downstream from the entrance of the magnet when measured in angle along the central orbit. Each of the normal exit ports can provide its beam channel with an available angular width of the radiation of about 40 mrad, and then each of the beam channels except three can provide the users with that of about 30 mrad. The three exit ports were restricted to less than 30 mrad because the quadrupole magnets downstream from these exit ports are close to the bending magnets and then also to their beam channels.

Therefore, the three B-ducts were newly designed to extend the available angular widths. A schematic drawing of a new chamber is shown in Fig. 2.4.1. The flange size of the exit ports was changed from ICF152 to ICF203, and its center was set on the '0 degree-line'. Each exit port makes available the synchrotron radiation with the angular width of 34 mrad from the bending magnet in which the exit port is put, and in addition that of 10 mrad from the upstream bending magnet.

These new B-ducts were installed in the bending magnets called B-03, B-05, B-17, respectively. Of the corresponding beam lines, BL-03 and BL-17 will use the synchrotron radiation only from bending magnet, while BL-05 will use the

synchrotron radiation not only from bending magnet but also from insertion device.

All-metal gate valves with RF shield

Until this summer shutdown, about ten gate valves were used in order to partition the vacuum of the ring into subsections. The sealing material of the gate valves was a kind of elastomer (Viton-A). In single bunch operation it was often observed that the vacuum pressure rose up around the gate valve, because the gate valves were heated up by the wake fields induced in their gaps and gasses went out from the Viton-A. Therefore, we decided that the gate valves should be replaced with all-metal gate valves with RF shield even at a large cost.

However, because the gate valves with RF shield were too expensive to replace all the old gate valves with them at the same time, we then prepared two kinds of all-metal gate valves: one is a guillotine type with RF shield and the other a pendulum type without RF shield. Four gate valves of the former type were installed at the RF-cavity sections, and another four gate valves of the latter type were distributed on the vacuum chambers outside the RF-cavity sections. Even if temperature of a gate valve without RF shield rises up in single bunch operation, clearly an amount of outgassing from it will be much little compared with that from Viton-A in the old gate valve. Since all-metal gate valves are easily damaged by either dust or stress, a great deal of attention was paid to their installation as well as to their bake-out so as not to give thermal stress.

Pumping speed at RF-cavity sections

In the latter half of FY 1984, abnormal rise of the vacuum pressure frequently occurred at the

south RF-cavity station. The pressure increased with the beam current, dependent on the filling shape of the beam. At that time, it seemed that this pressure rise was caused by outgassing from the graphite contactors attached to the tuners of the cavities, and that after the tuners were completely baked out it was then caused by the photon stimulated desorption of the molecules probably reabsorbed on the vacuum chamber near the cavities during the bake-out.

Whatever its cause was, it seemed that the pressure rise at the RF-cavity section might be kept small by the increase of the pumping speed. Therefore we designed a new chamber with larger pumping conductance and also a pumping unit consisting of an old sputter ion pump and a new sputter ion pump with the nominal pumping speed of 400 ℓ/s : it made the total pumping speed increased to 528 ℓ/s . This pumping assembly was installed close to each cavity at both the south and north RF stations.

Monitor system of synchrotron light

Visible part of the synchrotron radiation from a beam line exclusively owned by Light Source is used to monitor the beam profile. It is reflected down by a copper mirror in a vacuum and led to the monitor room through a vacuum window made of glass.

It was observed that the beam images on photodiode detectors and TV monitors moved as the beam current increased. As the mirror is on a bottom plate of the mirror holder cooled by water, we carried out an experiment to measure what amount of distance the image moved on the photodiode detector when the cooling water was stopped. From its amount, the temperature rise of the mirror surface was estimated to be 30 degrees or more at about 150 mA. As this thermal problem is more serious at higher current, the mirror and holder system was then redesigned to reduce the thermal distortion as small as possible, and it was installed in this summer shutdown.

The glass window was also replaced with new one because it was found that the glass became brown. As the change of color clearly indicates the generation of color centers in the glass, so the composition of the glass was analyzed by using a secondary ion mass spectrometer (SIMS). Indeed, an abnormal concentration of copper was observed in the surface layer. The result then implies the following process. The photons incident on the copper mirror desorbed its copper while the photons incident on the glass window induced negative charges on the window by an electric field of the negative charges, and them implanted in the surface layer of the glass.

2.5 ABNORMAL PRESSURE RISE AT THE RF CAVITY STATION

2.5.1 General Description

Vacuum deterioration at the south RF cavity station was usually observed one or two hours after the beam accumulation. It was an annoying problem for a long time because the beam lifetime decreased considerably as described in the Activity Report 83/84. The problem was finally solved by long lasting efforts through this year. It was found that the vacuum deterioration was caused by an outgassing from graphite contactors used in the cavity tuner and additionally by a desorption of gases from the wall of the beam ducts located near the cavities. It was also found that the proper procedure of bake-out, which will be described below, can completely suppress the pressure increase. The outgassing from the graphite contactors is probably due to the heating by the wake field induced by the beam. The mechanism of the desorption of gases from the beam ducts has not been understood yet.

2.5.2 Vacuum Deterioration

After the routine beam accumulation, the pressures near the south cavities gradually increased and sometimes got into the 10^{-7} Torr range with a short beam lifetime. However, the pressure recovered gradually as the stored current decreased. Figure 2.5.1 shows a typical example of this phenomenon which is characterized as follows: (1) it occurs frequently but not every time, (2) it is observed only at the south cavity station, and never at the north cavity station although they have exactly the same

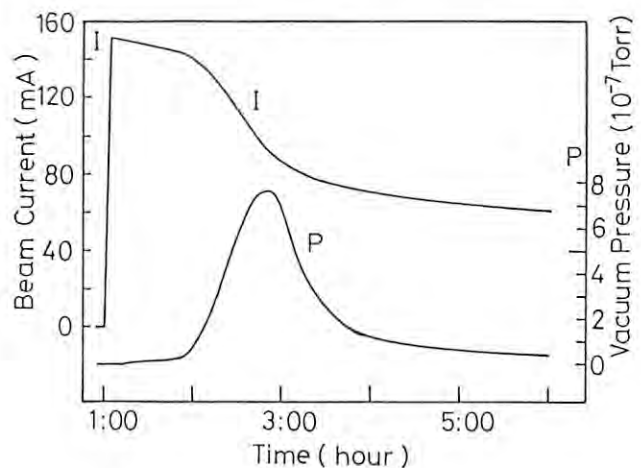


Fig. 2.5.1 An example of lifetime shortening due to the deterioration of the vacuum near cavities.

I: Beam current, P: Pressure.

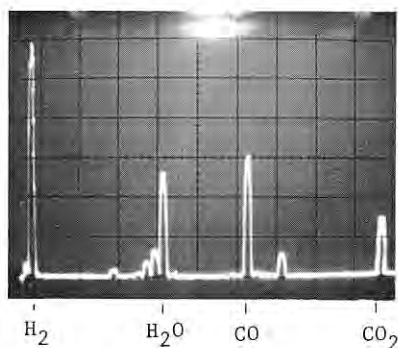


Fig. 2.5.2 A typical example of the mass spectrum.

configuration, (3) no dependence on the initial stored current ($100 \sim 150$ mA), (4) it occurs more frequently when the bunch-filling structure around the ring is sharp, (5) the main components of the desorbed gases are H_2 , CO, H_2O and CO_2 . A typical example of the mass spectrum is shown in Fig. 2.5.2.

2.5.3 Outgassing from the Graphite Contactors

The composition of the desorbed gases (Fig.2.5.2) shows that the reason of pressure rise is not a leak of air but a heating by the beam. The wake field induced by the beam is likely to heat some part of cavity or cavity-like structure. This idea can explain the dependence of the vacuum deterioration on the bunch-filling structure as well as the behavior of the pressure as shown in Fig. 2.5.1.

Several attempts were made in order to find out which components can be heated by the wake field. Finally, it was found that the graphite contactors used in the tuner were the most suspicious.

The contactors are used in order to prevent RF current from running through the bellows. Figure 2.5.3 shows the cross section of the tuner.

An outgas analysis made for various materials showed that only the graphite contactor evolves large amount of gases of both H_2O and CO_2 when heated. It was found that those gases partly change into H_2 and CO under the operation of sputter ion pumps.

Since it was recognized that the bake-out of the graphite contactors reduces the outgassing,

we tried to bake them by means of passing hot N_2 -gas through the channels for cooling water in addition to the usual bake-out procedure. In the beginning of the bake-out, the pressures increased to the range of 10^{-5} Torr, more than ten times as high as those in the previous bake-out where hot N_2 was not used. The bake-out was continued until the pressures fell to the

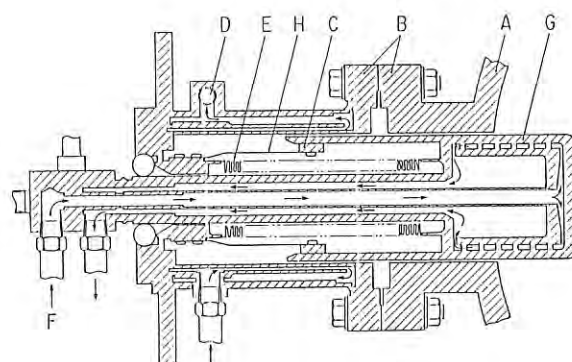


Fig. 2.5.3 Cross section of the tuner
 A: Cavity, B: Flange,
 C: Graphite contactor,
 D: Outlet of cooling water,
 E: Bellows,
 F: Inlet of cooling water,
 G: Plunger,
 H: Spring plate.
 * Arrows show the stream of cooling water.

range of 10^{-8} Torr. After the bake-out, the pressure below 10^{-9} Torr was obtained. However, contrary to our expectation, the vacuum deterioration occurred again.

2.5.4 Desorption from the Beam Ducts near the Cavities

No improvement was achieved by the graphite bake-out. Besides, after this bake-out, the vacuum deterioration occurred independently of the bunch-filling structure. This suggests that the vacuum deterioration was no longer due to the wake field. However, it should be noted that the mass spectrum was almost the same as that observed when the graphite contactor was heated.

It was considered that the gases released from the graphite contactors contaminated the wall of the beam ducts and that those gases were released again from the wall after the beam accumulation. In order to confirm this speculation, the bake-out was carried out again. The temperatures of the beam ducts were kept slightly higher than those in usual way, while the temperatures of the tuners were so controlled that the outgassing from the graphite contactors kept small. After this bake-out, the pressure of 2×10^{-10} Torr was obtained. This value is lower than before by a factor of 10. The vacuum deterioration has never been observed since this bake-out.

2.5.5 Remarks

We still have following questions: (1) Why did the abnormal pressure rise occur only at the

south cavity station? (2) What mechanism of the desorption can explain the behavior of the pressure as seen in Fig. 2.5.1? Recently it was found that one of the tuners of south cavities was set eccentrically. This tuner may resonate with one of the components of the frequencies of the wake field, caused to outgas by heating or discharging. This is probably the reason of (1).

2.6 CONTROL

So far the computer control system of PF storage ring has partly accomplished its purpose by controlling individual components of the ring and the subsystems made up of many components (the magnet system and the RF system and so on), and yet it was unsatisfactory from a point of view that the control system should interconnect the individual controls and serve as a unified system to operate the ring. Moreover the control system had not so enough flexibility as to meet the increasing requirements for it. Therefore we decided to rebuild the computer control system. In the beginning, we have been gradually replacing all of the old control computers with four 'super' mini-computers from last April. The new computer system has been working well, much better than the previous one. Presently the computer control by this system is still limited to the individual controls of the ring components and subsystems. In this autumn, however, the network system to connect the computers to each other will be in operation. With this new computer system, the control group is now encouraged to reconstruct the control system as a whole.

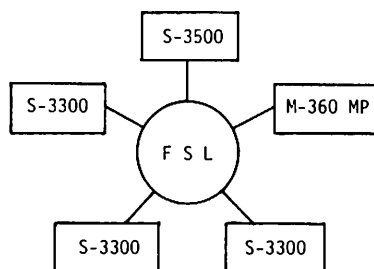
2.6.1 Improvement of Computer Control System

The reasons why the old computers (AICOM C-6) was replaced with the 'super' mini-computers (FACOM new 32-bits computers: one S-3500 and three S-3300) are as follows. (1) In order to support the old network system, PFX, the operating system of the old computer became so large that available memory region for users was decreased and also the speed of the loading and execution of application programs was slowed down, and as a result the performance of the network was reduced. (2) The reliability of the hardwares such as memory and disk was low, and then the cost of maintenance was increasing. (3) The programming language was PF-BASIC, an

interpreter language, so that the processing speed was insufficient and PF-BASIC had no means to divide a program into subprograms with reasonable size, i.e., to make a program with modular structure like the ones written in a high-level language. Thus, the maintenance of the control programs became more difficult as they became large in size.

In the April of 1985, new control computers with a new network system were installed, and also the old general-purpose computer, M-200, was replaced with M-360MP (24 MB). The new computer system is shown in Fig. 2.6.1, and a comparison between the new and old computers is given in Table 2.6.1. The new system is about 30 times larger in the processing power than the old one, and about 6 times larger in the memory capacity and about 10 times larger in the disk capacity, respectively.

Even with the increased ability of the computer system, however, there are a few problems we should take care of. It is required to develop more elaborate multi-task system for the real-time control, because the total number of computers decreased. The user manageable part of memory and disk will not be proportional to the increased total amount of their capacities because larger system softwares are required not only to manage large computers but also to accommodate to higher multiplicity of tasks.



FSL: Flexible System Link

Fig. 2.6.1 Physical connection diagram of the control computers of Photon Factory storage ring.

Table 2.6.1 Comparison between old and new computers for the control system.

	Old		New	
	AICOM C-6	FACOM S-3500	FACOM S-3500	FACOM S-3300
Computer				
Quantity	7	1		3
Memory size* (MB)	1	16		8
Processing speed (μ s)				
Floating add/subt.	27	0.36		0.99
Floating multiply	135	0.48		1.08
Disk capacity* (MB)	40	826		628

(* per one computer)

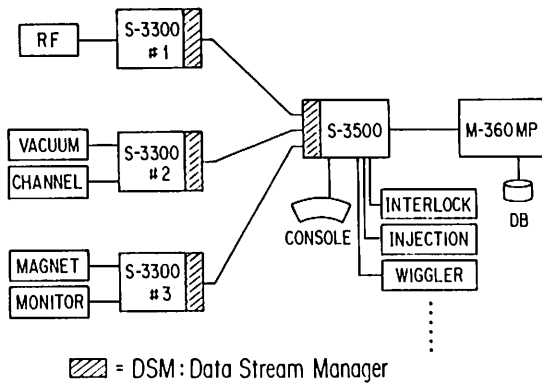


Fig. 2.6.2 Logical structure of the computer control system of Photon Factory storage ring.

The logical structure of the real-time control in the new system is shown in Fig. 2.6.2. S-3500 is the nucleus of this structure and it can communicate with other computers. Each S-3300 can almost independently make 1 - 2 processes that handle the data from various components of the ring and control the components. S-3500 controls many kinds of functions on the console and serves as a man-machine interface to all processes in other computers. It also plays a role as the center of data control. Through S-3500, data such as operational log are transferred to and stored in M-360MP. This general-purpose computer, M-360MP, can make a large calculation such as COD correction using data already sent from S-3500, and then it can automatically return the results to S-3500. In addition, S-3500 can deal with the control processes themselves transferred from S-3300.

The programming language in the new system is FORTRAN 77 that makes it possible to write a program with modular structure. All I/O processings such as CAMAC and GPIB, as well as network processings can be treated in the form of subroutine call in FORTRAN programs. An interactive debugger, TESTFORT, is prepared to test a program and it can check one line after another in a source program.

2.6.2 Network

The computers can communicate with each other through the network with a taken passing ring type, called FSL (Flexible System Link) as shown in Fig. 2.6.1. The basic specification of FSL is given in Table 2.6.2. FSL makes possible program-program communications between different computers by using the service routine, IPCF (Inter Program Communication Facility), which is callable from FORTRAN. IPCF also supports communications between two programs in different environments: one in real-time processing and the other in interactive processing.

Furthermore, we are preparing a utility software called DSM (Data Stream Manager) at the upper level than IPCF, in order to make the network system more flexible and to match the requirements to the control system. Figure 2.6.3 shows the tree-type structure of DSM, which can

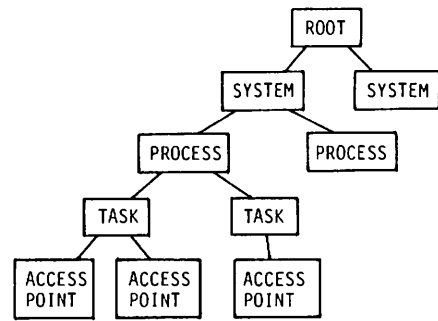


Fig. 2.6.3 Routing structure of DSM (Data Stream Manager).

transfer data between any two tasks either in the same computer or different ones. The data are transferred through input/output port called access point. There are two kinds of access points: transmitter and receiver. The input data into a transmitter are broadcasted to all of the access points defined as its correspondent receivers. A receiver sequentially stores the received data (sequential type) or holds only the latest data (update type). Each routing address can be changed interactively and independently of the other ones by using an application program.

2.6.3 Operator Console

In the old system, the functions of the operator console were almost fixed to each control section (magnet, RF, beam monitor and so on), mainly due to the fact that the old network system did not work as expected.

With higher ability of the new network system, the console with more flexibility than before will be easily reconstructed. The new console will consist of several fundamental units, each of which includes 2 displays (character/graphics) and 1 touch screen. Further a 'mouse' or a rotary encoder (knob) can be added to the unit. Each unit serves as a general-purpose equipment and can control any control section, and its assignment is easily changed. All the console units, controlled by the console computer, S-3500, can transact data and commands with the other computers through the network. For example, when a console task in S-3500 receives data for display from every other task,

Table 2.6.2 Basic specification of FSL (Flexible System Link).

Communication mode	N : N
Network topology	Dual ring
Transmission speed	10 Mbps
Transmission method	Token-passing
Transmission length	max. 192 km/ring
Cable	Optical fiber
No. of node	max. 64
No. of processor	max. 256

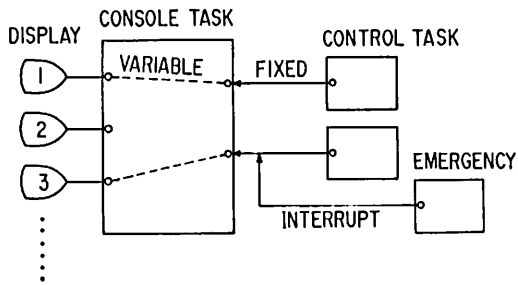


Fig. 2.6.4 Display routing function for operator console.

it dynamically sets a path to one of the displays and then delivers the data to the assigned display (see Fig. 2.6.4).

Some of the graphic displays are actually micro-computers (FACOM 9450-II) connected to the console computer by GPIB. At the application level, basic graphic plots such as bar graph, joined line graph, scatter plot and so on, can be readily depicted on the screens by using the display service utility prepared for users, free from any troublesome graphic or GPIB's routine.

Reference

- 1) Photon Factory Activity Report 1983/84, p.IV-27

2.7 BEAM MONITORING IN THE STORAGE RING

2.7.1 Introduction

The beam monitoring system has been working for three years since operation of the storage ring started. There has been made only minor changes without adding any new detector for last one year. General descriptions on the system were given in the previous reports and some new findings are discussed here.

2.7.2 Beam Position Stability

Stability of beam position was studied in several different conditions which had been suspected to be the would-be reasons for the changes of beam position. The conditions are chosen from the operation procedures usually taken during users time. The conditions used here includes simulated injection, varied beam current and excitation of the wiggler.

Analysis of position stability was carried out by taking two kinds of data before and after one procedure took place and the previous condition was resumed. In this report, the meaning of position stability is restricted to reproducibility of the initial beam position.

Effect of injection simulation

The injection procedure is effectively simulated by turning on and off the related

machine components by keeping the beam in the storage ring. It requires the following components: septums, kickers, dc bump but any real beam from the linac.

The first set of data was taken before the injection procedure was undertaken. The second set was taken when all the components necessary for the simulation were turned off and the normal storage mode was resumed. The two were compared by subtracting one from the other. The difference between them was as small as the accuracy of position monitor.

Effect of beam current variation

The beam current was varied stepwise by using the RF knockout system to check if beam position changes. The beam current was first accumulated up to 150 mA and reduced every 30 min. as 120, 90 and 60 mA. At each current value, beam position was measured.

Figure 2.7.1 shows the case when the beam current was changed from 150 to 60 mA. Between the two current values, the closed orbit distortion (C.O.D) was found to be stable within the accuracy of position monitor.

Effect of wiggler excitation

For the wiggler mode, there are several steps to be carefully differentiated. The operation of wiggler is composed of a series of procedures: (1) beam storage, (2) lowering the superconducting coil, (3) excitation of wiggler coil, (4) deexcitation, (5) raising the wiggler body to get the beam leveled to the wide gap free of magnetic field, (5) resuming the storage mode without wiggler (6) dumping the beam for fresh start, (7) storing beam for next run.

Two cases are chosen because they indicate there are some effects which must be known by the experimenters. Figure 2.7.2 shows the difference between C.O.D. data taken in procedures (1) and (3). This case shows the beam orbit is slightly changed in the vertical direction by a difference of 0.4 mm peak to peak. The difference in the horizontal direction is, however, as large as 1.2 mm peak to peak. Figure 2.7.3 shows the results of difference between data taken in procedures (1) and (7). This case shows there is a difference of about 0.2 mm peak to peak. This amount of change may bother some experimenters who use position sensitive instruments. It is suspected that the beam is affected by the remnant field of wiggler. It seems possible that

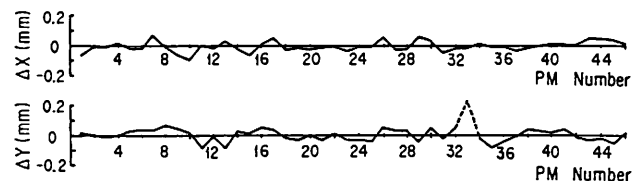


Fig. 2.7.1 Beam position deviation measured for the change of beam current from 150 mA to 60 mA. There are 45 position monitors around the storage ring.

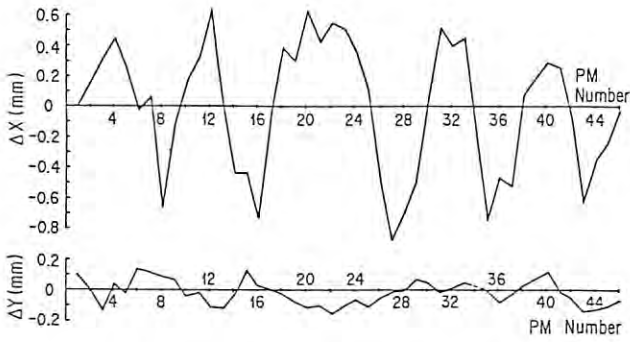


Fig. 2.7.2 Beam position deviation measured when the wiggler coil was excited.

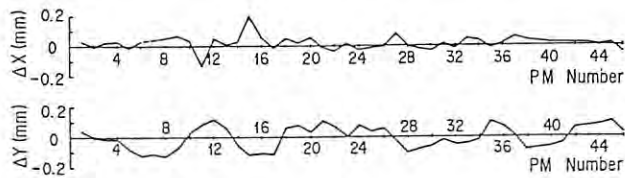


Fig. 2.7.3 Beam position deviation measured between two storage modes, one before and the other after a complete cycle of wiggler excitation and deexcitation.

the remnant field strength is strong enough to reach the center of the wide gap through the pole piece of which edge is 50 mm apart from the beam path of normal storage mode.

2.7.3 Synchrotron Light Observation System

The synchrotron light is brought down to the dark room after being reflected by a copper mirror in the vacuum duct. The light beam is then separated into different beam lines for specific observations.

Mirror cooling water and fluctuation of light beam

The present optical system is sensitive to thermal deformation of the copper mirror and also susceptible to vibrations induced by the cooling water system. The beam spot observed with a photodiode was often lost from the sight when beam current changed rapidly or injection took place. We suspected that the mirror experiences thermal bending when thermal inflow is high. The water flow to the mirror was purposely decreased to see if any obvious thermal deformation is detectable as a deflection of the light reaching the photodiode. Adjusting the water flow rate by the number of turns of the valve, we observed the thermal deformation of the same magnitude as that which had been seen in real situations. The cooling capacity of mirror is to be increased by making minor modification.

Use of the X-rays of the synchrotron is in consideration to observe the beam size and position without being disturbed by thermal or vibrational deflections of the optical path. No mirror is needed to extract X-rays. It is also easier to avoid vibrations coming from the water cooling system.

The extraction port of the synchrotron light is now in modification to monitor the characteristics of electron beam more stably and to make wider application of the synchrotron radiation for other test experiments. The port is divided into two independent lines which are extended so as to come out through the shielding wall of the storage ring. More description about the extraction port is found in the vacuum section of this issue.

Characteristics of the synchrotron light

Some characteristics of the synchrotron light were examined during the measurement of beam position and profiles.

a. Polarization of the synchrotron light

The polarization of synchrotron light was observed by using a polarizer plate. A polarizer plate was inserted in the path of synchrotron light which is the primary light beam directly coming from the copper mirror in the vacuum duct. The polarizer axis was aligned either parallel or perpendicular to the median plane of radiation. Figure 2.7.4 shows the two cases, one with the polarizer placed parallel and the other perpendicular. With the polarizer placed perpendicular, a dark band is seen in the center.

The transverse distribution of light is taken with a linear photodiode array placed behind the polarizer. Figure 2.7.4 includes oscilloscope traces of photodiode signals in the lower half. There are 32 channels of diode which give the negative signals. Each diode gain is

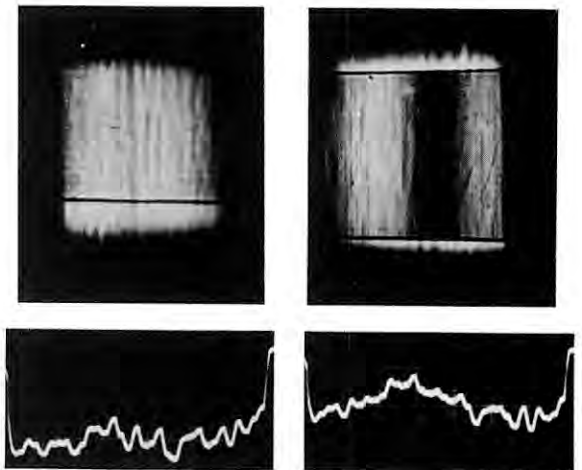


Fig. 2.7.4 Polarization of synchrotron light observed with a polarizer placed parallel and perpendicular to the plane of radiation.

adjusted to be equal for the same intensity of light. The diode signal level is almost flat for the parallel polarization. The perpendicular polarizer lowers the signal level of all the channels and makes a sag in the dark band compared to the parallel.

Granular structures were also observed in the scope traces of diode signals as well as in the pictures above. The difference between dark and bright areas is greater than the natural gain deviation from channel to channel. A pattern similar to this granular structure has been seen with the X-ray beam which is supplied to users in the experimental hall. The reason why such structures appear is still under investigation.

b. Chromatic aberration in the optical system

Chromatic aberrations are nuisance for the measurement of beam profiles. When the focused image is blurred due to aberration, measurement of beam size will produce a bigger number than it should. All the lenses in the optical system are corrected for aberration and other components which are mirrors and neutral filters are free of aberration. Nevertheless, the focused image tends to be blurred with something aberrational.

At present, we use a bandpass filter in blue region to minimize the aberration and estimate errors expected for the true value of beam size. However, there is a demerit in using a bandpass filter. The filtered light loses its brightness by an order of magnitude or more. This will cause the S/N ratio of the photodiode signal to be small at lower beam current. It is necessary to find a way to minimize the chromatic aberration without losing the brightness. Further investigation is under way to find the causes of aberration still remaining in the system.

2.7.4 Diagnosis of the Streak Camera System

The streak camera system was diagnosed under the technical assistance of the manufacturer. The streak camera has been used for observation of synchrotron light from the storage ring. The synchrotron light was brought down to the camera with a spot size of 50 μ or less. The synchrotron light comes out as a pulse train of 2 ns intervals and reflects the time structure of the stored beam.

Time axis calibration with dual light beam

There were raised some questions with the camera system during the observation:

- (1) whether fluctuations of the pulse structure really reflect the beam itself or not. This concerns the measurement of bunch length and pulse height
- (2) whether the time axis of the streak camera is linear for its sweep ranges. This concerns the measurement of bunch-to-bunch distance.

The calibration was made as follows. The synchrotron light beam was split into two beams and one was given a time delay of about 0.8 ns from the other. The two were merged into one beam line and fed to the camera one after the

other.

First, this type of test checks if the streak camera conserves the pulse shape wherever the light pulse comes in on the time axis. Figure 2.7.5 shows that the two pulses made from the same one are received by using 10 nsec sweep range. They are 0.8 nsec apart and conserve the same pulse shape. The ratio of areas under the two pulses, e.g., A/A' or B/B' as shown in Fig. 5, is constant and its fluctuation is less than 10 %.

Next, the test also gives an answer if the time difference between the two pulses stays the same along the time axis. In the figure, another two lie next to the first set of two. They are a pair made from the second pulse in the original beam and keep the same distance for the time difference of 0.8 nsec. This proves that the time difference is almost constant at these points on the time axis.

Other problems: "burnout" of photocathode, and stray lights

The diagnosis revealed two other problems that will make measurement inefficient:

- (1) deterioration of the photocathode sensitivity due to continuous exposure to intense light
- (2) disturbance of measurement by stray lights hitting directly the phosphor screen.

These problems mainly depends on the scheme of camera system including its optical alignment procedure. The camera has a slit of 30 - 100 μ fixed at the center of the photocathode. This arrangement will cause the incident angle of light to be fixed at a certain direction and the photocathode surface to be always exposed at the same spot.

First, the deterioration of photocathode sensitivity must be lessened to keep the life of

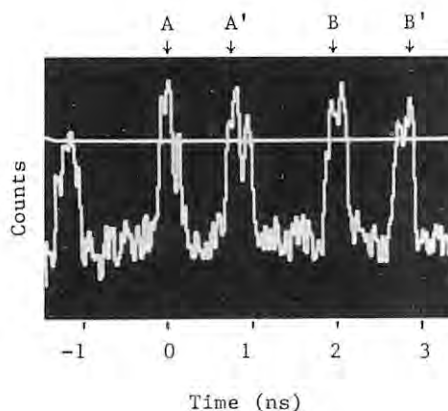


Fig. 2.7.5 Beam bunch structure observed with streak camera. The original beam is split into two and merged into one beam with a delay of 0.8 nsec between the two. Bunch A (B) is followed by bunch A' (B'), i.e., delayed A.

streak tube long. The streak camera observes only a few of the light pulses while the sweep voltage of a few hundred nsec pulse is applied every 1 msec. However, the synchrotron light keeps shining the photocathode irrelevantly to the sweep time. This continuous exposure causes the photocathode sensitivity to become poor at the spot where the light falls. The sensitivity was measured on the photocathode surface by using uniform lighting. Figure 2.7.6-a shows the "burnout" spots of the photocathode and Fig. 2.7.6-b gives its sensitivity curve. The burnt-out regions are seen as dips on the curve. It is necessary to minimize the exposure time of the photocathode.

A quick solution to this problem is now to be given to protect the photocathode from burnouts. A simple mechanical camera shutter will help decrease exposure time by a factor of 10 to 100 and make the life of the tube longer.

Second, stray lights often enhance a bright spot on the phosphor screen at the rear end of streak tube and disturb the observation. This is due to the structural reason of the streak camera. Photons passing through the photocathode can reach the phosphor screen directly through holes of MCP depending on its incident angle. Figure 2.7.7 shows a stray spot appearing at the upper left corner.

A cure to this problem is to attach a thin aluminum foil in front of the MCP so that no light directly reaches the phosphor screen. To prove this, we tried to test a tube remodeled with aluminum foil cover on MCP which was courteously provided by the manufacturer and observed no stray lights. Since replacement of the whole streak tube is quite costly, we try to avoid this problem by readjusting the axis of the incident light.

2.8 SUPERCONDUCTING VERTICAL WIGGLER

An automatic current control system using a micro-computer came into operation this year. This system controls ramping-up of currents of the main power supply and two auxiliary power supplies, and can keep the orbit distortion during ramping within an allowable level. Undesirable beam loss during ramping of the wiggler current, which had been experienced in the early date, was eliminated. Another improvement in the operation of the wiggler magnet is the completion of an automatic supply system of liquid helium. When the liquid helium level in the wiggler cryostat goes down below a certain level, liquid helium is transferred to the cryostat from a helium tank through a 12 m long transfer line by pressurizing the helium tank. Inner pressure of the tank is controlled finely by the use of a digital manometer and a micro-computer, so that transfer loss of liquid helium has been reduced.

The most remarkable progress on the operation of the wiggler is that the 5 T operation became possible in the routine operation of the Storage Ring. In addition to above-mentioned efforts to reduce instabilities, fine adjustment of the operating betatron frequencies and optimum

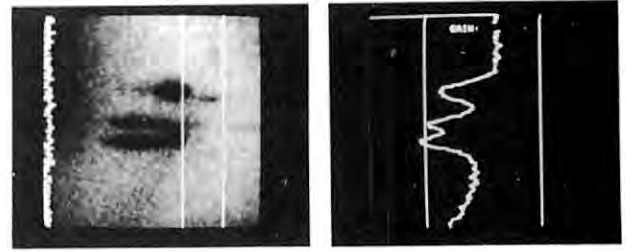


Fig. 2.7.6 Burnt out spots on the photocathode surface of the streak tube. Picture (a) shows the surface is burnt out at three spots. Picture (b) is the linear plot of photocathode sensitivity.

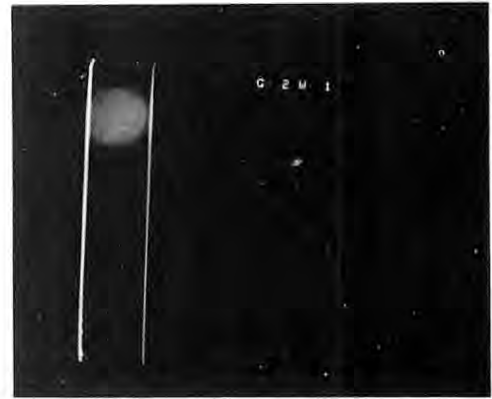


Fig. 2.7.7 Stray lights reaching the phosphor screen of the streak tube.

positioning of the wiggler magnet in the vertical direction was effective to obtain longer lifetime. As the result of the orbit bump of the electron beam in the wiggler, the electrons go through the non-linear field of wiggler magnets, which are given in lateral direction as follows,

$$B = B_0 - 49.4 B_0 y^2 - 1.9 \times 10^4 B_0 y^4$$

for outer coils, and

$$B = B_0 - 32.7 B_0 y^2 - 2.0 \times 10^4 B_0 y^4$$

for central coil. In order to minimize the effect of the non-linear field, the center of the wiggler magnet is set so as to agree with the half line of the orbit bump. In October, the beam lifetime became 1000 minutes at the excitation of 4.5 T, while it was 700 minutes in July. At the same time the operation of the wiggler magnet at 5 T became possible with sufficiently long lifetime. Figure 2.8.1 shows an example of the lifetime versus the stored beam current during the wiggler operation at 5 T. Comparing with the similar curve described in Annual Report 1983, one can see that the lifetime becomes two times longer than that obtained in the previous year.

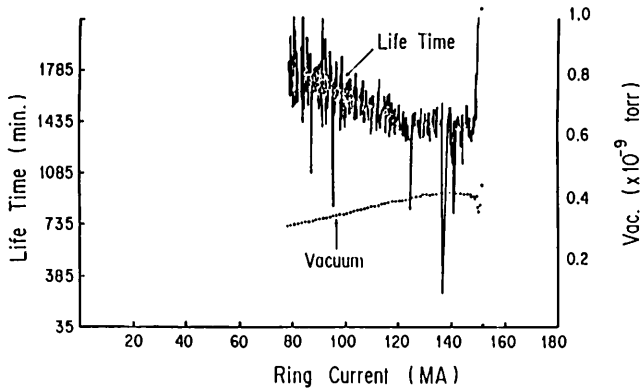


Fig. 2.8.1 Current dependence of the beam lifetime and the average vacuum pressure.

2.9 BEAM CHANNEL

2.9.1 New Beam Channels

Projects to construct eight new beam lines (BL-6,7,8,9,16,17,27; AR line) have been in progress in the fiscal years 1984 - 1985. Together with the existing eight beam lines (BL-1,2,4,10,11,12,14,15),⁽¹⁾ a total of sixteen beam lines will become operational in the near future. Table 2.9.1 summarizes the new beam lines.

Beam lines affiliated to the Photon Factory

BL-27

With the recent advent of high brightness synchrotron radiation sources, such as undulators and wigglers, mirror materials resistant to the high power load have become more and more important. A mirror test programme, in

collaboration with the Daresbury SRS, has been under way using a test port at SRS for the last two years.⁽²⁾ In order to expand the research, a project to construct BL-27 intended for mirror irradiation tests has been in progress in collaboration between the Photon Factory and Hitachi Ltd. in the fiscal years 1984 - 1985.⁽³⁾ BL-27 is also designed to allow the use of infra-red component of synchrotron radiation because infra-red spectroscopy by the use of synchrotron radiation becomes more important.

Figure 2.9.1 shows the layout of BL-27, which is being installed at the time of writing (September, 1985). The beam exit port BP-27 is located just downstream of the injection point, not permitting synchrotron radiation to enter the experimental hall, so that BL-27 is to be installed within the ring tunnel. The maximum horizontal beam divergence accepted is 24 mrad because of the size and location of the nearest quadrupole magnet. The mirror chamber for the infra-red line is designed in such a way that radiation should be deflected vertically by 90° to be conducted to the underground floor. No specifications for an infra-red monochromator have been determined as yet. The differential pumping section will produce a pressure difference of two orders of magnitude, which will protect the ring vacuum against outgassing from test mirrors. The mirror irradiation chamber will be equipped with viewing ports made of sapphire to allow evaluation of the temperature of the mirror surface struck by synchrotron radiation by measuring infra-red radiation emitted from the mirror. A TV camera will also be installed to monitor the mirror surface. All equipments are to be remotely controlled from the underground floor. BL-27 will be used for mirror irradiation tests for the time being, having provision for alternate use for infra-red spectroscopy in the future.

Table 2.9.1 New beam lines being developed in FY 1984/1985.

Beam lines	Affiliation	Source	Experimental spectral region	Status as of September 1985
BL-6	KEK-PF	bending magnet	X-ray and VUV	under construction
BL-7	U. of Tokyo	bending magnet	X-ray and VUV	completed (front end) under installation (branch lines)
BL-8	Hitachi Ltd.	bending magnet	X-ray and VUV	completed
BL-9	Nippon Electrical Corporation	bending magnet	X-ray and VUV	completed (front end) under installation (branch lines)
BL-16	KEK-PF	50 pole permanent magnet wiggler/undulator	X-ray and VUV	under construction
BL-17	Fujitsu Ltd.	bending magnet	X-ray and VUV	under construction
BL-27	KEK-PF	bending magnet	infrared and white	under installation
AR line	KEK-PF	bending magnet of AR	hard X-ray	under installation

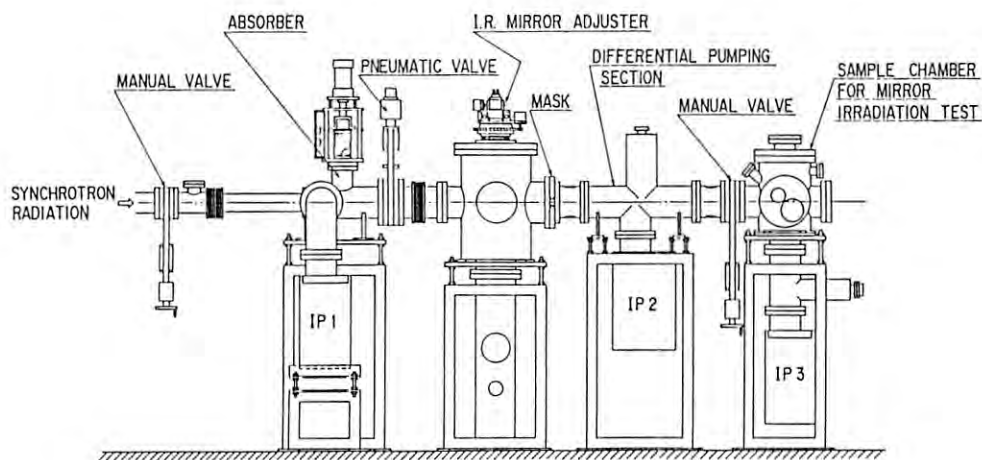


Fig. 2.9.1 Side view of BL-27.

AR beam line

A project to mount a synchrotron radiation beam line on the TRISTAN Accumulation Ring, AR, (4) has been developed with the cooperation of the Photon Factory and the accelerator department of KEK in the fiscal years 1984 - 1985. The goal of this project is to provide extremely intense radiation over a hard X-ray spectral range. The AR is a storage accelerator of 377 m in circumference, accelerating electrons and positrons to 6 - 8 GeV prior to injection into the TRISTAN Main Ring. The radius of curvature of the orbit in bending magnet sections is 23.15 m, and the critical wavelength of synchrotron radiation, λ_c , is 0.6 Å for 6 GeV and 0.25 Å for 8 GeV. The experimental hall is located on the northeast arc of AR. Proposed experiments include angiography, structure analysis at high pressures, and Compton scattering.

The layout of the AR beam line is shown in Fig. 2.9.2. The beam line will utilize a 10 mrad horizontal divergence of radiation emitted from electrons at the bending magnet section, 82B, and accommodate a single branch line in the first phase of the project. The front end consists of a manual gate valve, a water-cooled absorber, a pneumatic gate valve, a water-cooled beryllium

heat absorber, a dual beryllium window assembly, (5) (6) safety beam shutters and vacuum components. Unlike in the beam lines attached to the Photon Factory ring, a fast closing valve is not installed. All vacuum chambers are made of aluminum. The beam line will be controlled with the same interlock system as that for beam lines on the Photon Factory ring. (7) (8)

BL-6 and BL-16

The design of an X-ray beam line, BL-6, and a multipole wiggler/undulator beam line, BL-16, is currently under way in the fiscal year 1985.

BL-6 is the fourth X-ray beam line with a bending magnet source, intended to meet the increasing user needs in the X-ray spectral region. It will be used for protein crystallography (BL-6A), EXAFS (BL-6B), soft X-ray photoelectron spectroscopy (BL-6C), structure analysis at high pressures (BL-6C), and X-ray diffraction at low temperatures (BL-6C). A tandem experimental station arrangement will be employed in BL-6C, with the first station serving for soft X-ray experiments and the second for hard X-ray experiments.

The radiation source of BL-16 is a 50 pole permanent magnet wiggler which will be installed

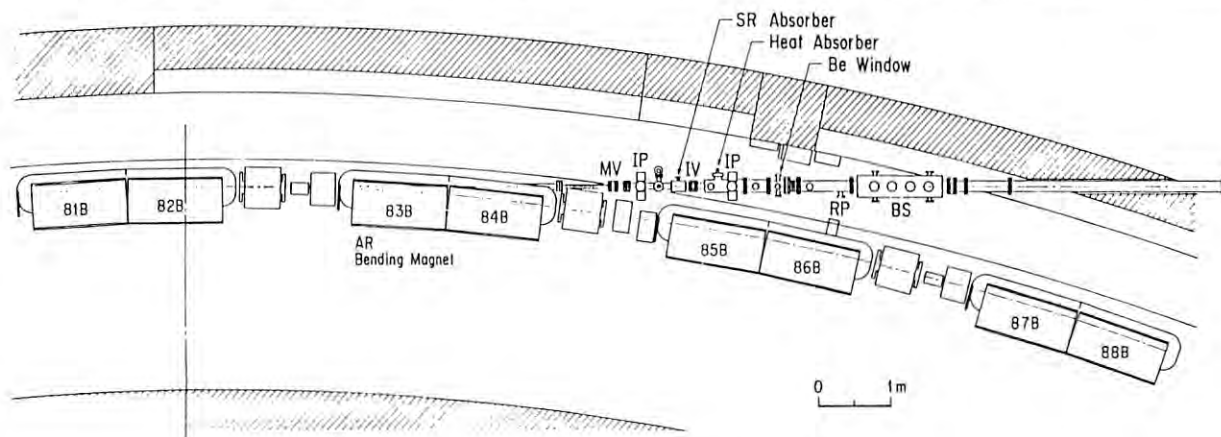


Fig. 2.9.2 Layout of the AR beam line.

in the long straight section between bending magnets, B15 and B16. It is planned to construct one hard X-ray branch line in the first stage of the project, making provision for optional installation of one more branch line. Anticipated experiments are fluorescent EXAFS, surface analysis, X-ray diffraction at high pressures etc. The multipole wiggler can be also operated in an undulator mode by varying the magnet gap. Synchrotron radiation in the undulator mode will be horizontally deflected by a mirror to be delivered to an experimental station where soft X-ray and VUV spectroscopy will be made.

Beam lines affiliated to outside groups

Projects to construct four beam lines have been in progress as a joint effort between outside groups and the Photon Factory in the fiscal years 1984 - 1985.

BL-7 and BL-8

The fabrication of hardwares as well as the design consideration of BL-7 and BL-8 begun in the fiscal year 1984.⁽⁸⁾

BL-7 is affiliated to Research Center for Spectrochemistry, The University of Tokyo. The beam line accepts a 35 mrad horizontal divergence of radiation, and is equipped with an improved fast closing valve which has a closing time of about 10 msec. The front end was completed at the end of the fiscal year 1984. BL-7 accommodates three branch lines, which are intended for use in angle-resolved photoelectron spectroscopy and photo-stimulated desorption (BL-7A), angle-resolved photoelectron spectroscopy and photo-chemical reactions (BL-7B), and various X-ray experiments (BL-7C). One of the branch lines, BL-7C, belongs to the Photon Factory and will be made open to the public. The branch lines as well as the experimental stations are being installed presently.

BL-8 is affiliated to Hitachi Ltd. The front end, which allows for a horizontal beam width of 36 mrad divergence, was completed in the latter half of the fiscal year 1984. BL-8 comprises three branch lines (BL-8A,8B,8C) in the first phase of construction and has a port for installing an another branch line (BL-8D) in the future. The three branch lines and a part of experimental stations were completed at the beginning of the fiscal year 1985. BL-8 will be used for VUV and soft X-ray spectroscopy (BL-8A), EXAFS (BL-8B), and lithography and tomography (BL-8C). First experimental activities are anticipated in the fall of 1985.

BL-9 and BL-17

BL-9 belongs to Nippon Electrical Corporation. Design studies started in the latter half of the fiscal year 1984 with completion of the front end in the first half of the fiscal year

1985. The beam line is planned to accommodate four branch lines, which will be used for lithography (BL-9A), photo-chemistry (BL-9B), and EXAFS and X-ray diffraction (BL-9C). Specifications for BL-9D have not yet been determined. The two branch lines, BL-9A and BL-9C, which are given priority, are under installation as of September, 1985.

BL-17 is affiliated to Fujitsu Ltd. The three year project for this beam line started in the fiscal year 1985. Because of the location of a RF cavity, BL-17 is designed to utilize a 6 mrad horizontal divergence of radiation from the bending magnet section, B16, as well as a 30 mrad beam from the bending magnet section, B17. The 36 mrad of radiation will be divided among three branch lines and a monitor line. Two branch lines (BL-17A,17B) will be initially implemented. Proposed experiments include lithography, EXAFS, SEXAFS and photo-excited CVD.

2.9.2 Discharge Cleaning of Carbon-Contaminated Mirrors

Carbon contamination is fatal to the efficiency of optical elements used in synchrotron radiation beam lines.⁽⁹⁾ In a search for a rejuvenation method for contaminated elements, dc glow discharge cleaning in oxygen of some carbon-contaminated mirrors has been made.⁽¹⁰⁾

In order to clarify the effect of the discharge on the roughness of the reflecting

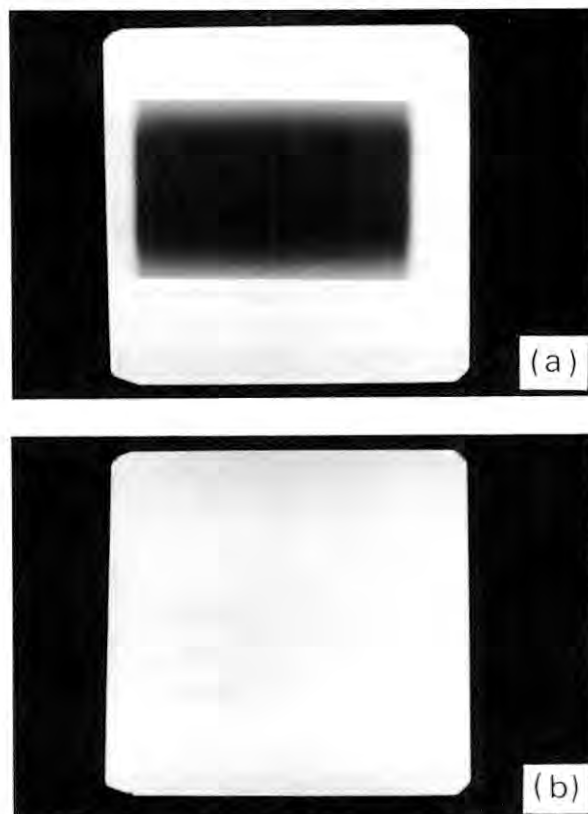


Fig. 2.9.3 Photograph of a Pt-coated fused quartz mirror (a) before and (b) after discharge cleaning.

surface, angle-resolved scattering measurements as well as reflectance measurements were made for a "clean" Au-coated fused quartz mirror before and after the discharge procedure. No change in reflectance and scattering level was observed over a spectral range of 5 - 40 eV after a discharge for 10 minutes in the arrangement in which the mirror surface did not face an aluminum cathode. This result shows that no harmful effect on the surface roughness was produced by the discharge in that arrangement.

A contaminated Pt-coated fused quartz mirror is shown in Fig. 2.9.3(a) before discharge cleaning and in Fig. 2.9.3(b) after cleaning. The mirror had been used as the second prereflector of a Seya-Namioka monochromator for a year. Carbon buildup due to cracking of hydrocarbons is clearly seen in the region where the synchrotron radiation beam struck the mirror (Fig. 2.9.3a). All visual evidence of a contaminant film was removed after cleaning for 20 minutes in the discharge arrangement in which the mirror surface did not face the aluminum cathode (Fig. 2.9.3b).

Reflectance spectra of the same mirror before and after cleaning are compared in Fig. 2.9.4(a) for near normal incidence and in Fig. 2.9.4(b) for grazing incidence. The reduction in reflectance before the discharge procedure is severe except in the energy region between 15 and 20 eV for near normal incidence. For grazing

incidence, on the other hand, no remarkable difference is observed over the range above about 10 eV, while the effect of carbon contamination is seen below 10 eV. The reflectance after cleaning is found to be largely restored for near normal incidence. The absolute value of the reflectance is slightly lower than values reported for Pt metal in the literature. However, the structures at about 10 eV, 22 eV and 32 eV, which are characteristic of Pt, can be clearly observed after cleaning. The reflectance data reported in the literature have been measured on clean surfaces prepared in situ in high vacuum environment whereas the mirror used here was exposed to air after it was coated with Pt. Therefore, the present result indicates the enough recovery of reflectance of the mirror. Other results as well as the experimental procedures are presented in reference 10.

Reflectance degradation due to carbon contamination would be most severe in the vicinity of the carbon K edge at 284 eV. The effect of the discharge on the surface roughness might not be negligible in this shorter wavelength region. We intend to extend this work to higher photon energies containing the carbon K edge by using a grasshopper monochromator. We are also planning to install in situ cleaning arrangements in a mirror chamber on a multipole wiggler line (BL-16), which is now under design.

References

- 1) Photon Factory Activity Report 83/84 (1984) p.IV-40.
- 2) A.A. MacDowell, J.B. West and T. Koide, to be published in Nucl. Instr. and Meth.
- 3) S. Sato, T. Koide, N. Kanaya, M. Niwano and I. Nagakura, to be published in Nucl. Instr. and Meth.
- 4) KEK Annual Report (1983) p.20.
- 5) I. Nagakura, KEK Report KEK-81-17, 1982.
- 6) S. Sato, T. Koide, Y. Morioka, T. Ishii, H. Sugawara and I. Nagakura, Nucl. Instr. and Meth. 208 (1983) 31.
- 7) N. Kanaya, IEEE Trans. on Nuclear Science NS-31 (1984) 957.
- 8) Photon Factory Activity Report 83/84 (1984) p.IV-43.
- 9) T. Koide, S. Sato, H. Fukutani, H. Noda, S. Suzuki, T. Hanyu, T. Miyahara, S. Nakai, I. Nagakura, A. Kakizaki, H. Maezawa, T. Ohta and T. Ishii, Nucl. Instr. and Meth. A239 (1985) 350.
- 10) T. Koide, S. Sato, T. Shidara, M. Niwano, M. Yanagihara, A. Yamada, A. Fujimori, A. Mikuni, H. Kato and T. Miyahara, to be published in Nucl. Instr. and Meth.

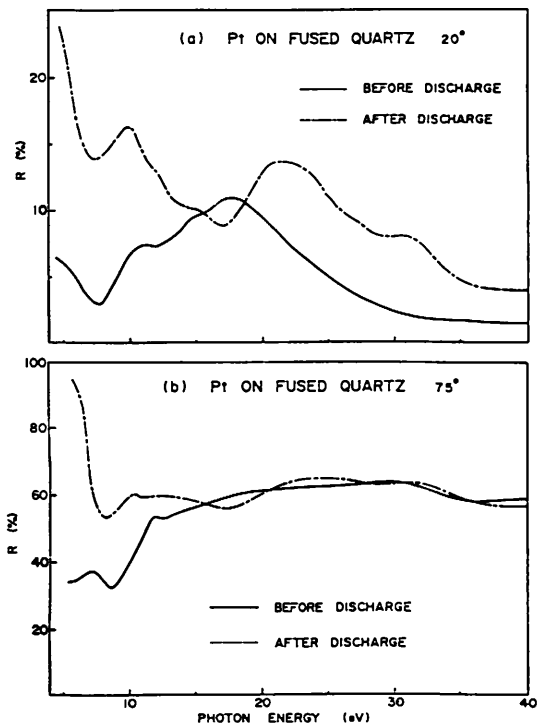
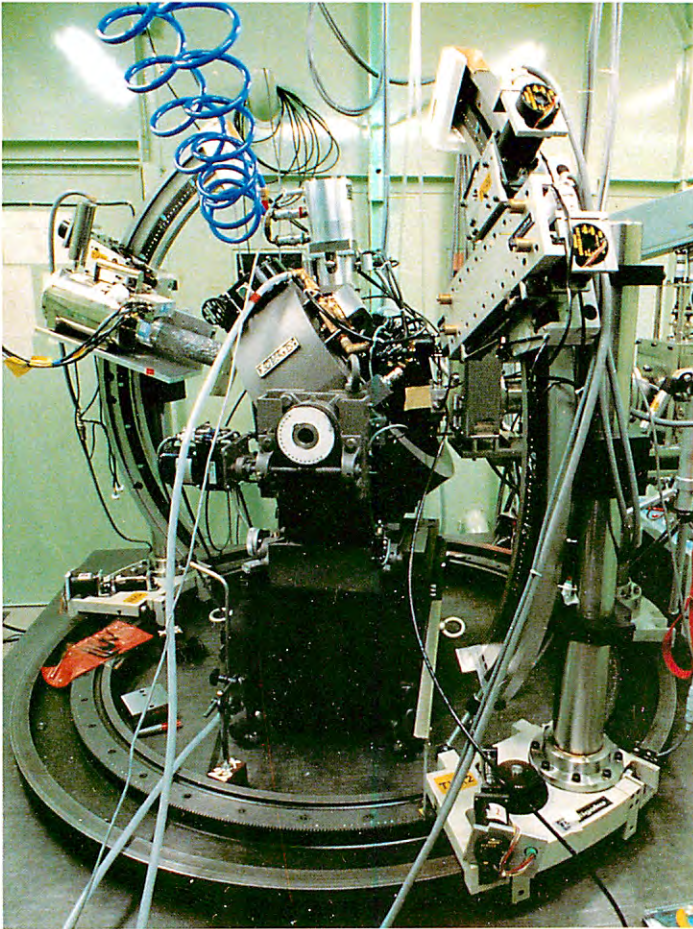


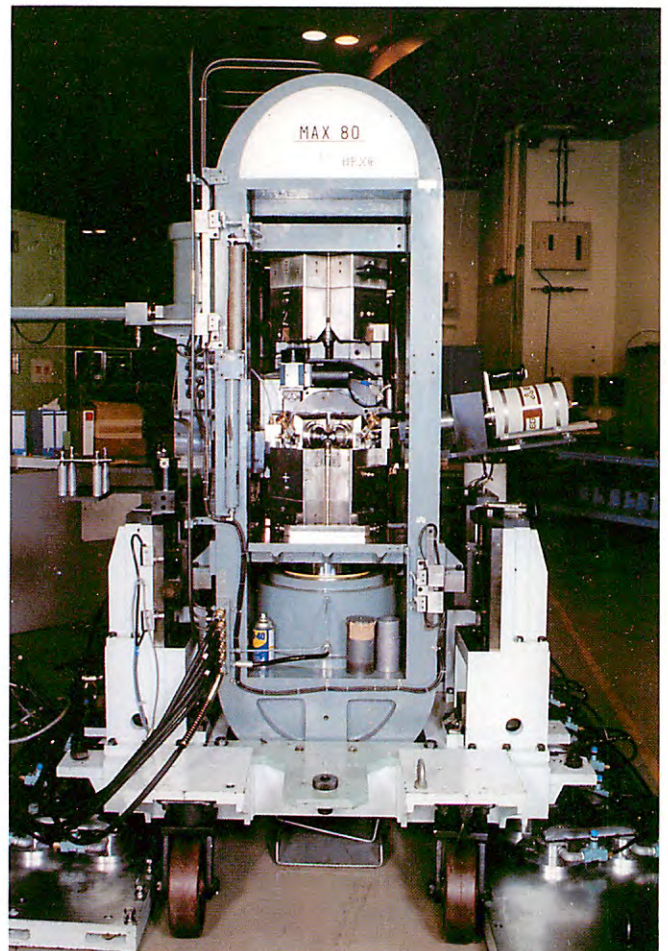
Fig. 2.9.4 Reflectance spectra of the Pt-coated fused quartz mirror before and after discharge cleaning. (a) Angle of incidence of 20°. (b) Angle of incidence of 75° and S polarization.

V. Instrumentation Division



Cubic anvil used for X-ray diffraction under high pressure (up to 130 Kbar) at high temperature (up to 1300°C).

High speed X-ray topography camera under magnetic fields (up to 12 kOe) at low temperature (down to 10 K).



V. BEAM LINES AND OPTICS

1 Beam Lines

After almost completion of eight beam lines with some branch lines, which do not exceed three in each, together with about thirty experimental apparatuses, in 1984, a lot of users from all over the universities and institutes including private companies has enjoyed a steady progress in their approved proposals. Proper financial supports by the Government mainly for the extension of new beam lines and installation of advanced original apparatuses were put off in spite of persistent requirement of them geared to users' needs and activities. Accordingly, improvements of the apparatuses, their control systems, maintenance equipments etc have been done with scrupulous care. In the past year, Research Centre for Spectro-chemistry (RCS) of Faculty of Science, University of Tokyo and Hitachi Works' group have constructed new beam line BL-7 and BL-8 based upon each research plan of their own, respectively, in collaboration with PF-KEK.

BL-21 was from the first dedicated to only one beam monitor line in PF, which has recently undergone improvements used for X-ray region beam monitor, in addition to visible region. Ideally speaking, such a beam monitor should be equipped in each beam line for examination of beam

characteristics.

Beam Line 7

For RCS of Faculty of Science, the University of Tokyo, a special budget from the Ministry of Education, Science and Culture was approved in FY 1983 and FY 1984 for the construction of a new beamline dedicated for the studies of solid surfaces. The beam port No.7 was allotted for this beamline. The design and construction of this beamline have been carried out under the collaboration between RCS-Univ. of Tokyo and PF-KEK.

The principal beam available at this beamline has the divergence of 35 mrad in horizontal and 7 mrad in vertical, which is divided into three branch lines, BL-7A, BL-7B and BL-7C. Two of them, BL-7A and BL-7B are SX and VUV lines. Another branch line which was initially planned as a free beam port for hard X-rays, is to be used by KEK-PF to construct a station for EXAFS and X-ray diffraction experiments, having a double-crystal monochromator. A fast closing valve with the work time of 10 ms and an acoustic delay-line with a simplified structure have been installed as the safety device against the accidental vacuum break-down. The beamline is now in the final stage of construction. The followings are the brief description of BL-7A and BL-7B.



An overall view of Beam Line 7.

BL-7A

This branch line has been designed so that either monochromatized radiations in the energy region of 10-750 eV or white radiations in the energy range below 1 keV can be selectively used.

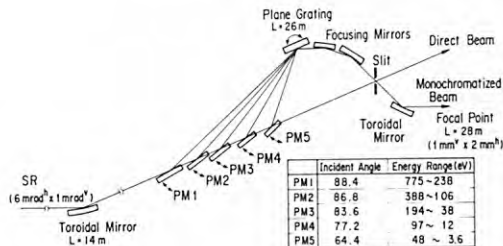


Fig. 1 Optical system of the plane grating monochromator.

Figure 1 shows the arrangement of the optical components. The radiation is first deflected by a toroidal mirror and then by one of the five plane mirrors which are placed between the toroidal mirror and a plane grating and selected depending on the required photon energy range. The plane mirror acts as a high-cut filter. A direct white beam is obtainable when all the plane mirrors are taken off from the beam path. The beam from the grating is focused onto the exit slit by means of two spherical mirrors and then focused at the sample position by use of a toroidal post focusing mirror. The beam size at the sample is expected to be $2 \text{ mm}^H \times 1 \text{ mm}^V$. This optical system has been designed to give a strong monochromatic radiation with medium resolution. All the optical parameters were determined through the ray tracing by use of the iterative method for non-linear optimization.

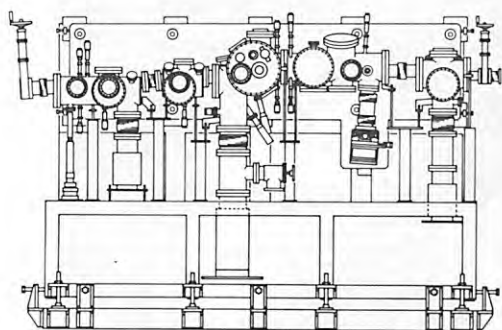


Fig. 2 Side view of the plane grating monochromator (BL-7A).

The outlook of this plane grating monochromator is illustrated in Fig. 2. The experiments which are expected to be carried out at this branch line, are the angle-resolved photoelectron spectroscopy, photo-stimulated ion desorption and so on.

BL-7B

This branch line having a 1 m Seya-Namioka-type monochromator has been designed for the experiments which require a strong monochromatic VUV radiation. The optical system is illustrated in Fig. 3.

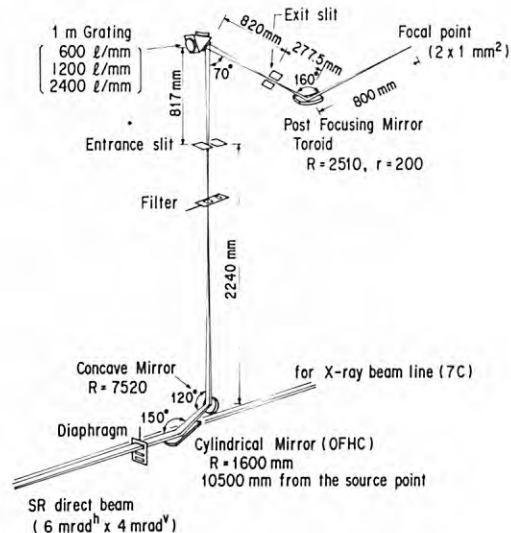


Fig. 3 Optical system of the 1 m Seya-Namioka monochromator (BL-7B).

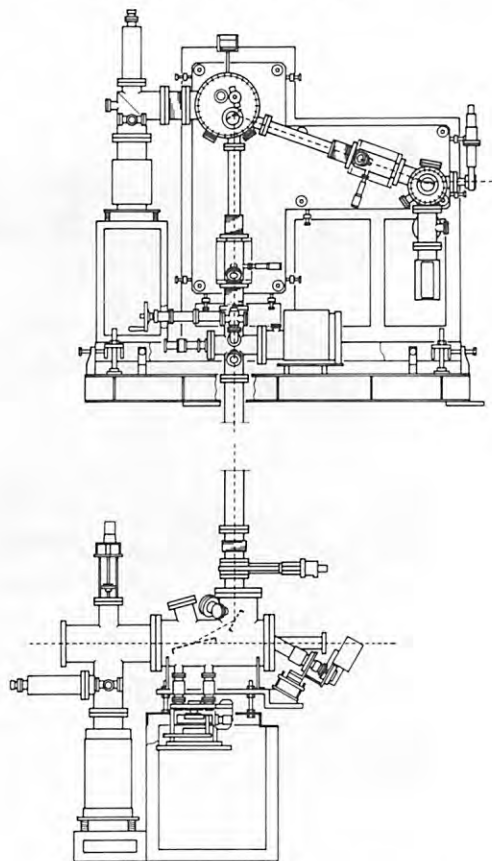


Fig. 4 Side view of the 1 m Seya-Namioka and its mirror chamber (BL-7B).

The synchrotron radiation is deflected to the vertical direction by means of the pre-focusing mirror system composed of a cylindrical mirror and a concave mirror, and then monochromatized through a 1 m concave grating. A toroidal mirror is used to focus the beam at the sample position, the expected beam size at the sample being $2 \text{ mm}^H \times 1 \text{ mm}^V$. The optical

parameters are optimized by the same method as the one used for BL-7A. Figure 4 shows the structure of this monochromator. Experiments such as photochemical reactions on solid surfaces, multi-photon excitation by use of SR and laser light and angle-resolved UPS are planned to be carried out at this branch line.



An overhead view of
Beam Line 8.

Beam Line 8

This beam line consists of three branch lines and covers the spectral range of 0.3 - 300 Å (40 eV - 40 keV). Soft X-ray spectroscopy, EXAFS, X-ray lithography and X-ray tomography stations are now under construction, and some of them will be ready for experiments in the autumn run of 1985. The arrangement of the beam line is shown schematically in Fig. 5. Out of the horizontal divergence angle of 32 mrad extracted from the source point, branch lines 8A, 8B and 8C accept 1.0, 3.0 and 5.0 mrad, respectively. Branch line 8D, which will be constructed as a VUV-line in the future, will accept 2 mrad. Characteristics of three branch lines are summarized in Table 1.

BL-8A attaches directly to the ring vacuum, and 8B and 8C have vacuum tight Be windows which separate the ring vacuum from vacuum regions of 10^{-6} - 10^{-7} Torr. The design, the construction and the check of the vacuum and interlock systems have been performed by Central Research Laboratory, Advanced Research Laboratory, Mechanical Engineering Research Laboratory, Hitachi Research Laboratory, Production Engineering Research Laboratory, Energy Research Laboratory and Hitachi Works, Hitachi, Ltd. in cooperation with PF-KEK.

Front End

The basic design of the front end follows that of BL-11. The pressure at the entrance of the front end came down to the order of 10^{-10}

Torr at the stored current of 100 mA, in April, 1985.

A new type of fast closing valve (FCV) system has been developed to protect the ring from the accidental vacuum breakdown. As a fast-responding and stable sensor, a cold cathode-gauge was tested and proved to be satisfactory for the system. The FCV is driven by a solenoid, and a spring-driven door-type plate closes the beam aperture to provide a high impedance to the shock wave. The valve plate return original position by the solenoid. The total closing time was 33 msec including the response time of the sensor.

An acoustic delay line (ADL), located upstream of the sensor, delays the arrival time of a shock wave for more than 200 msec, enough time to close the FCV. The total operation of the ADL and FCV system was tested at Hitachi Works before installation at PF-KEK.

A large pneumatic valve, having effective hole of 12" in diameter with 14" conflat flanges, has a spring return mechanism. This enables the valve to close in the event of an abrupt loss of the compressed air, and keeps high vacuum in the storage ring from an accidental vacuum breakdown in downstream.

Beam splitting section

A water-cooled mask splits the radiation into four beams and three of them are extracted to branch lines 8A, 8B and 8C.

A Pt-coated SiO_2 (or CVD-SiC) plane mirror deflects the radiation to 8A filtering out the

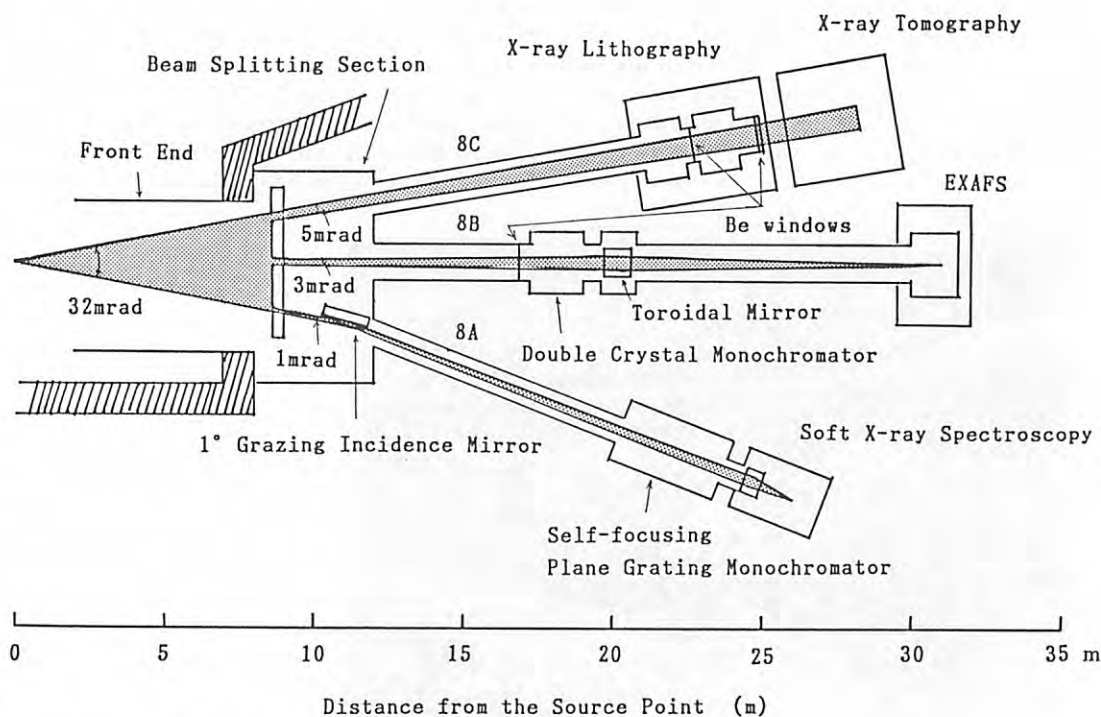


Fig. 5 Layout of BL-8.

Table 1 Characteristics of BL-8

branch line	pre-mirror	acceptance(mrad) horiz. × vert.	monochromator	post-mirror	wavelength range(Å)	resolution	typical application
8A	plane	1.0 × 3.0	self-focusing plane	bent	8-300	$\Delta \lambda / \lambda = \sim 10^{-3}$ (*)	soft X-ray spectroscopy
8B	—	3.0 × 3.0	double crystal Si(220), etc.	bent cylinder	0.4-12	$\Delta E/E = 10^{-3} \sim 10^{-4}$	EXAFS
8C1	—	5.0 × 3.0	—	cylinder or plane	2-300	—	X-ray lithography
8C2	—	5.0 × 3.0	Si(111), (220), (400)	—	0.3-2.5	$\Delta E/E = 10^{-3} \sim 10^{-4}$	X-ray tomography

(*)For 20 μm exit slit. (The entrance slit of this monochromator is defined by the source size of the synchrotron radiation.)

hard X-ray component. A horizontal acceptance of the mirror is 0.7 mrad with a grazing angle of 1°. The degradation of the reflectivity, brought about by the formation of carbon layers on the irradiated area, causes serious problems for spectroscopic measurements. To keep the good reflectivity, the mirror can be shifted to illuminate a carbon-free surface area of the mirror.

The base pressure of this section was less than 5×10^{-10} Torr without the radiation, and increased to 5×10^{-8} Torr at the ring current of 100 mA, during the summer run of 1985.

BL-8A

A self-focusing plane grating monochromator has been developed to provide a soft X-ray beam in the spectral region of 8 - 300 Å for solid-state spectroscopy. This is located at 22 m from the source point. By selecting one of two plane gratings, the wide spectral range can be covered. These plane gratings have a self-focusing property owing to varied-space grooves. The characteristics of the gratings are summarized in Table 2.

The chamber and the gratings are bakable up to 150°C, and a base pressure of less than 5×10^{-9} Torr has been achieved. During the summer

run of 1985, the optical alignment was checked and found to be satisfactory.

A bent mirror for focusing, and an appropriate filter to suppress stray and higher order beams, are planned for installation downstream of the monochromator.

Table 2. Characteristics of the gratings

type	plane(self-focusing)	
blank size (mm)	220×40×30	
ruled area (mm)	200×40	
material	pyrex	
coating	gold	
wavelength range(Å)	8-100	80-300
groove density(1/mm)	2400	800
blaze angle	1.0°	2° 18'
blaze wavelength(Å)	5	80

BL-8B

This branch line is designed for experiments on EXAFS. The station, now under construction, is located 30 m from the source point.

Optics of this line consist of a double crystal monochromator and a bent cylindrical mirror for focusing. The monochromator will cover the spectral range of 0.4 - 12 Å by selecting one of four single crystals (beryl(10T0), InSb(111), Si(220) and Si(422)). The bent cylindrical mirror will be set downstream of the monochromator. It is expected to give approximately 2:1 focusing.

A mini-computer, Hitachi E-800, is installed

to compute, for example, the radial distribution functions from the data of EXAFS experiments.

In the summer run of 1985, a preliminary experiment of X-ray topography, using white X-rays, was successfully made to check the alignment of this branch line. The test of EXAFS system will begin in the autumn run of 1985.

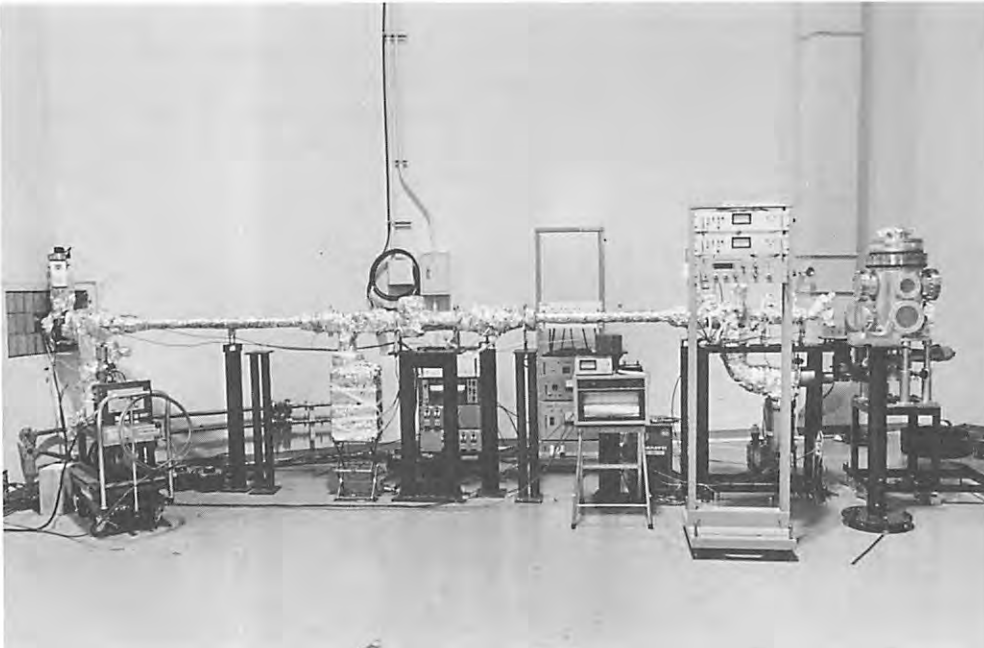
BL-8C

This branch line is under construction, and will have two stations, 8C₁ and 8C₂, located in tandem at 23 m and 28 m from the source, respectively.

8C₁ is the X-ray lithography station and will cover the spectral range of 2 - 300 Å. The radiation will be deflected vertically by an oscillating mirror system to sweep wide area of a sample surface. The vacuum of the lithography chamber, which is of the order of 10⁻⁷ Torr, is separated from the ring vacuum by a Be window to confine gaseous hydrocarbon compounds in the lithography chamber.

8C₂ is dedicated to X-ray tomography and covers the spectral range of 0.3 - 2.5 Å. A pair of Be windows, each 250 μm in thickness, will be set at the exit port of the lithography chamber. Downstream of the Be windows, three types of channel-cut monochromators (Si(111), Si(220) and Si(400)) will be set in the air. Using a monochromatized beam, three dimensional distributions of constituent elements in a sample will be obtained by adopting techniques of computed-tomography (CT). Digital radiography is also under preparation at the station 8C₂.

The test of the performance of optics and experimental apparatus for X-ray lithography and X-ray tomography will begin in the autumn run of 1985.



Side view of
Beam Line 21

Beam Line 21

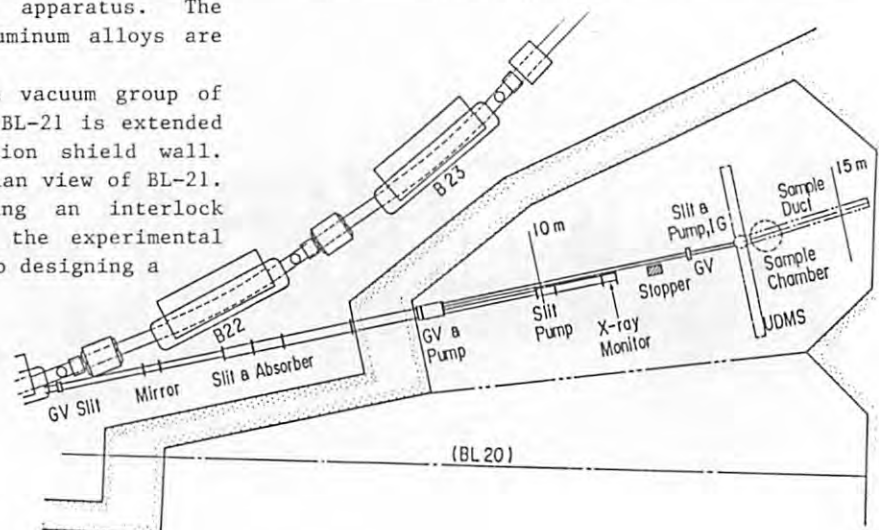
BL-21 has been used for the monitor line, which has a mirror system and visible light is reflected perpendicularly to the underground via a glass window. The mirror is made of copper and its surface is optically flat and plated by sputtered gold films. The mirror is bolted on the copper plate of the mirror holder which is cooled by water. The mirror geometry to the photon beam is adjustable for the rotation around two axes on the surface and for the heights. In the last run, we tried to confirm the temperature dependency of the image position on the photodiode detector. Because, when we stored the electron beam of 400 - 500 mA in autumn run, input power on the mirror will increase to about three times higher than the usual run and we worry about the distortion of the mirror and the shifts of the image. The mirror temperature was changed by slotting the cooling water. Just after the valve was choked, the image moved to the outside of the detector. We estimated the temperature rise as 30 degree or more. This result is important not only to the beam monitor system but to the experimental instruments.

A new mirror system is now produced to improve thermal conductivity between the mirror and the mirror holder. In this system, bottom of the copper tube will be polished and act as a mirror, which tube is a coaxial and cooling water pass through the tubes so the back side of the mirror is cooled directly. The mirror holder mechanism is similar but the holder system is tilted 45 degree to the beam. The mirror chamber is also changed to fit a new mirror system.

BL-21 has also served photons to the irradiation experiments. The photon irradiation experiments on outgassing is indispensable to understand the mechanism by photon stimulated desorption (PSD) and to improve the ring vacuum. It is clear that good vacuum gives long life time of the beam and reduces the detrimental life time by ion trapping. The photons passing through the side of the mirror were collimated by slits and brought into the experimental apparatus. The results of outgassing from aluminum alloys are published¹⁾.

The monitor group and the vacuum group of the ring have had a plan that BL-21 is extended to the outside of the radiation shield wall. Figure 6 shows a schematic plan view of BL-21. Both groups are now preparing an interlock system, a monitor system and the experimental apparatus on PSD. They are also designing a

Fig. 6
Schematic layout
of beam monitor line.



radiation shield made of iron. When the beam line is extended, the monitor group will watch the image of the beam on phosphor screen by direct X-ray without any optical systems. This simple detector system will give beam position and beam profile directly without distortion of the mirror in high current operations. The photon beam size on the phosphor screen will be limited by slits and be 7 mm in width and 5 mm in height.

The experimental methods on photon stimulated desorption (PSD) is composed of the two methods i.e., one is the ordinal throughput method and the other is a new method by using a unidirectional detector²⁻⁴⁾. The new method can be applied to small samples of aluminum, aluminum alloy, stainless steel and copper. The outgassing rates will be obtained for various conditions of pretreatments. Chemical compositions in metals will be analysed after photon irradiations.

The new method is also applied to real vacuum ducts made of aluminum alloy, stainless steel and copper. The first trial is to obtain angle resolved outgassing along the duct periphery. The next trial is to obtain the outgassing in case of grazing incidence of photons separating the outgassing by scattered photons. These experiments are necessary to design future large electron storage rings. The experiments need duct space so the apparatus will set in the experimental floor of the BL-21.

References

- 1) O. Grobner et al.: KEK Report 83-18, Oct., 1983
- 2) Y. Tuzi and M. Kobayashi: Proc. 9th Intern. Vac. Congr. and 5th Intern. Conf. Solid Surfaces, Invited Paper Vol., Madrid, 1983, p.203.
- 3) Y. Tuzi, M. Kobayashi and I. Arakawa: Proc. 14th Intern Symp. Rarefied Gas Dynamics, Tukuba, 1984, p.385.
- 4) M. Kobayashi and Y. Tuzi: Oyo Butsuri 54 (1985) 478 in Japanese.

2 Optics : DOUBLE CRYSTAL MONOCHROMATORS in BL-14B and BL-14C

BL-14B

A double crystal monochromator was installed on this beam line in April, 1985. A schematic drawings of this monochromator is shown in Fig. 7. In the followings itemized the design principles: (1) Two goniometers for the first and the second crystals are driven independently by an intelligent controller. (2) Two positions of the constant deviated monochromatic beam are available, one for 200 mm and the other for 500 mm apart from the straight line (white X-ray beam lines for Beam Line 14B and 14C). (3) The table, on which the goniometers are mounted, is isolated from the vacuum chamber in order to avoid transformation during the evacuation process. (4) The first goniometer is an ω - 2θ two axis goniometer. A lead shield (8 mm thick) on the 2θ table absorbs the high-energy scattered X-ray except toward the direction of the second crystal. (5) Both flat and sagittally focusing crystals are available for the second crystal. (6) The beam duct for Beam Line 14C pieces the vacuum chamber in order to avoid the awkward scatterings.

The Bragg angle available for 200 mm offset ranges between 4.73° and 12.73° , and for 500 mm offset 11.31° and 24.98° . If we simply assume the silicon 111 reflection, these values correspond to the value of wavelength of $0.517 \text{ \AA} \sim 1.382 \text{ \AA}$ for 200 mm offset and $1.230 \text{ \AA} \sim 2.649 \text{ \AA}$ for 500 mm offset.

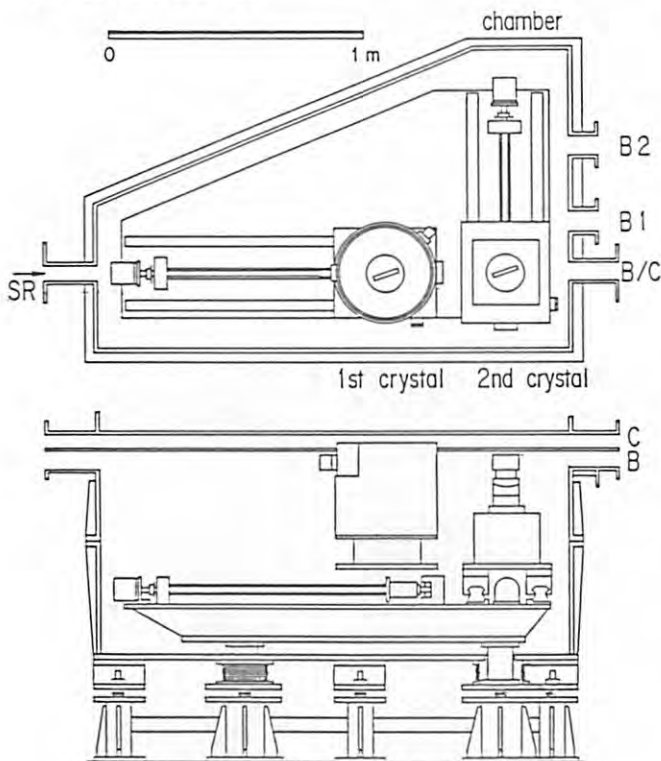


Fig. 7 Schematic drawings of BL-14B double crystal monochromator.

Unfortunately, at the site reserved for this monochromator, the crane of the experimental hall was not available. Instead, we made a lift system for the vacuum chamber using four mechanical jacks.

Test operation with two flat (111) silicon had been carried out for 200 mm offset beam line on the first two weeks of the vertical wiggler operation. Continuous scan between 0.5 A and 1.35 A was successfully made without observing change in output beam position.

After the test operation, the monochromator was released for user's experiments for four weeks until the end of the summer run in 1985.

This double crystal monochromator has an independent control system. Synchronous operation between the monochromator and the experimental apparatus can be made through a communication line between two CPU's for the monochromator and the experimental apparatus. This communication line is a standard asynchronous RS 232C of 9600 bps. All the motion of the monochromator can be controlled by simple commands of ASCII alpha-numeric codes output to the communication line by the CPU of the experimental apparatus. This makes it quite easy for users to bring their own apparatus and control system to BL-14B and making their own control software without having a detailed knowledge of the monochromator control system.

BL-14C

BL-14 is divided into 3 branch lines: 14A, 14B and 14C. BL-14C for the end station was designed for the experiments such as X-ray topography, X-ray angiography, Compton Scattering, High Pressure X-ray diffraction and others. Furthermore, a double crystal monochromator is installed into this branch beam line, and either white or monochromatic X-rays beam is available at need. Figure 8 schematically shows the layout of the fixed exit beam position monochromator. It has been installed upstream of the experimental hutch 14C. This monochromator employs two separate flat silicon or InSb crystals to be rotated and/or translated under control of a microcomputer. Figure 9 is the top view of the inside of the monochromator chamber. The monochromator consists of the following three main motions driven by stepping motors.

- 1) The rotation of the first crystal with precision of $0.2''$ per pulse. The rotation angle is read by a rotary encoder with an accuracy of $3''$ arc.
- 2) The translation of the first crystal with a step of $1 \mu\text{m}$ per pulse. Its movement is read by a rotary encoder with an accuracy of $10 \mu\text{m}$ along the total stroke of 1350 mm.
- 3) The rotation of the second crystal with precision of $0.1''$ per pulse. It is read by a rotary encoder with an accuracy of $1''$ arc.

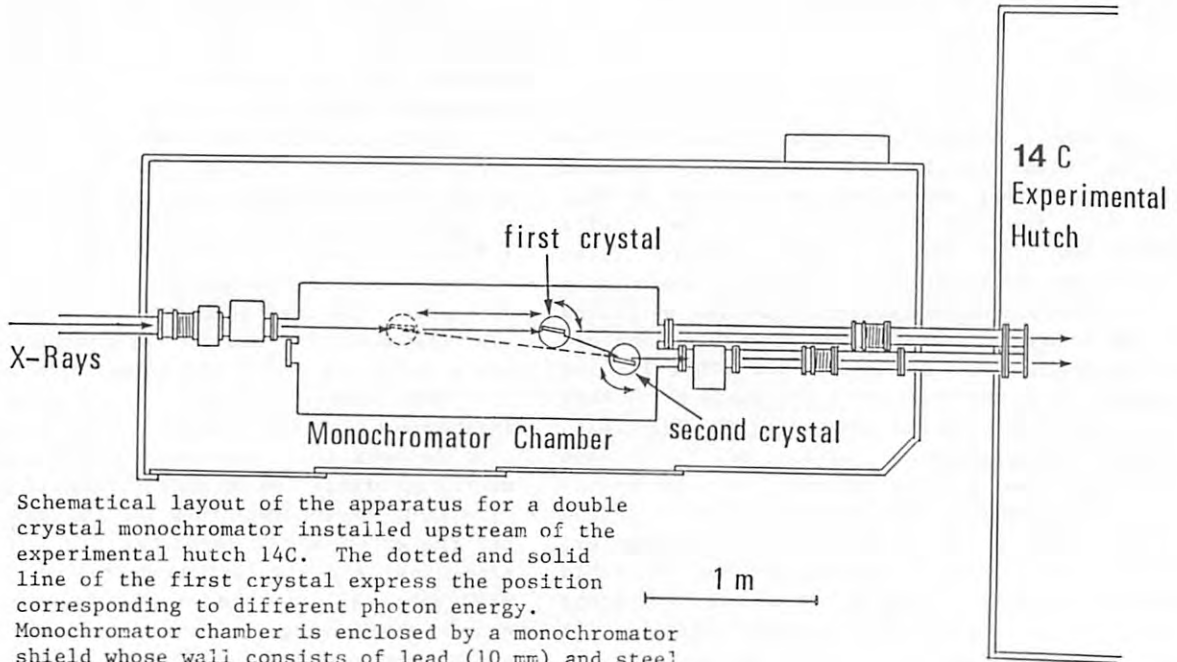


Fig. 8 Schematical layout of the apparatus for a double crystal monochromator installed upstream of the experimental hutch 14C. The dotted and solid line of the first crystal express the position corresponding to different photon energy. Monochromator chamber is enclosed by a monochromator shield whose wall consists of lead (10 mm) and steel (6 mm).

These three motions are also watched by limit switches and position sensors to avoid collisions and to get the origin of movements, respectively. Furthermore, a tilt and a fine rotation of each crystal can be adjusted by a piezoelectric translator linked to a micrometer driven by a d.c. motor. This translator has not yet been used so far, because even fine adjustment of rotation and translation of the two crystals can be achieved by three pulse motors.

The first crystal glued with In metal onto a copper plate is water cooled in order to avoid heating from irradiation of white X-rays. As the crystal angle range is $2.6^\circ \sim 25^\circ$, the energy range of monochromatized X-rays is $5.5 \sim 43$ keV by using silicon 111 reflection, and is $14 \sim 108$ keV by using 331 reflection. The typical beam size of the monochromatized X-rays has 10 mm width and 50 mm height; If used an asymmetry reflection, it can be achieved up to 50×50 mm².

Figure 10 shows a block diagram of the control system around a microcomputer. The software of the system has been prepared for some fundamental modes such as (1) pulse motor operation, (2) step scanning mode and (3) tuning mode. (1) In the pulse motor operation mode, we can drive one pulse motor only. (2) In the step scanning mode, where three motors are linked by a software, the energy of monochromatic X-rays can be automatically swept. Thus we can measure the absorption edge by using this mode and calibrate the energy value of X-rays concerned. Since the first crystal is heated by white X-rays when a shutter is opened, the intensity of monochromatic X-rays from the second crystal slightly decreases, and the time of decreasing to a half value of intensity is about several 10 min. to 1 hr. From this fact, it is necessary to tune automatically the intensity of monochromatic X-rays. Because the second crystal is not

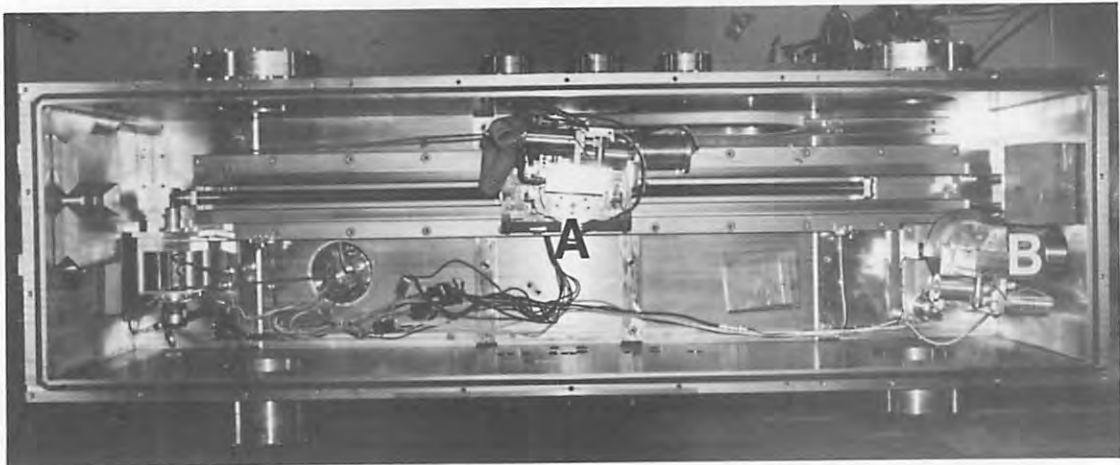


Fig. 9 Top view of the apparatus. A and B are first and second crystals, respectively.

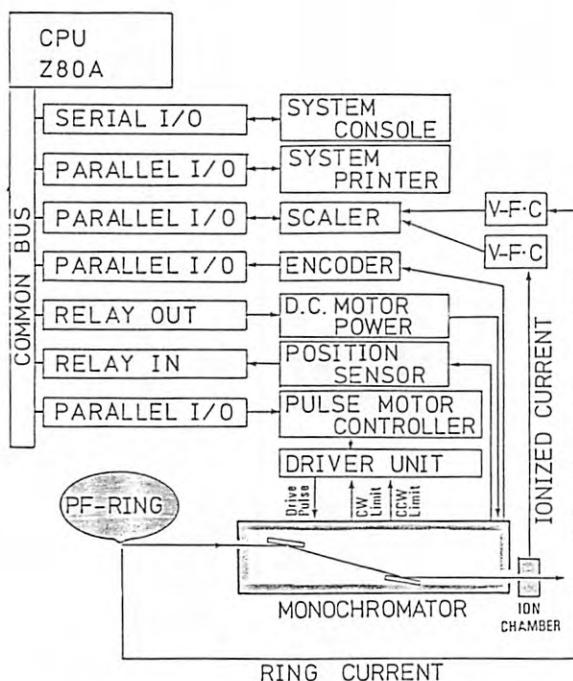


Fig. 10. Block diagram of the control system.

subject to heat, it can install a rotary encoder of 1" arc as reference and the tuning of the first crystal is necessary. The intensity of monochromatic X-rays are measured by an ion chamber. (3) In the tuning mode the peak intensity is automatically searched and is kept the peak position by controlling the rotation of the first crystal with a feedback loop of the signal. Even if the intensity is off the peak by accident, it can be recovered only by calling this mode.

As shown in Fig. 8, the monochromator chamber is enclosed by a monochromator hutch, because the high energy scattered X-ray photons from the first crystal penetrate the stainless steel of the chamber. The wall of the hutch comprises steel with 6 mm and lead with 10 mm thickness. During the experiment run of 5 T wiggler beam with 150 mA no leakage was found.



A bird's-eye view of BL-14 and 15.

Beam Line	Horizontal Acceptance Angle (mrad)	Typical Beam Spot Size (H mm × V mm)	Photon Flux at Sample Position	Monochromator (Crystal)	Energy resolution ($\Delta E/E$)	Energy range (KeV)	Mirror	Line Vacuum (Gas)
4A	6	50 × 5		none	white radiation	4 - 35	none	Vacuum
4B	4.5	50 × 5		none	white radiation	4 - 35	none	Vacuum
4C	4	50 × 5		double crystal Si (111) (sagittal focusing being prepared)	$\sim 2 \times 10^{-4}$	4 - 20	none	Vacuum
10A	1	10 × 3	1×10^9 at 10 KeV with flat Si (111)	Silicon (111) Germanium (111) Pyrolytic graphite (002) Curved Si (111) ($\alpha 8^\circ$)	5×10^{-3} $\sim 5 \times 10^{-4}$	6.5 ~ 25	none	Helium
10B	2	8 × 1	3×10^8 at 10 KeV with Si (311)	Channel-cut Si (311) Double Si (111) Double Si (220)	1×10^{-4}	6 ~ 30 3.5 ~ 15 5.5 ~ 25	none	Vacuum
10C	4	6 × 1.5	$\sim 10^{10}$ at ~ 8 KeV	double crystal Si (111) fixed beam position	$2 \sim 10^{-4}$	4 ~ 10	bent cylinder	Helium
14A	1.28	5 × 38		Double Si (111) Double Si (331) Double Si (551)	2×10^{-4}	5.1 ~ 19.1 12.9 ~ 48 21.1 ~ 78.6	Bent Cylinder for Vertical Focusing, Pt-coated fused quartz	Vacuum (line) He (mono-chromator)
14B	2.2	5 × 30		Double Si (111) Double Si (220) Double Si (311)	2×10^{-4}	5.2 ~ 57	Sagittal focusing	Vacuum
14C	1.3	10 × 40		Double Si (111)	2×10^{-4}	5.5 ~ 43	none	Vacuum
15A	2	2.6 × 1.3	9×10^{10} at 8.3 KeV (I=150mA)	Curved Ge (111) ($\alpha=8.0^\circ$)	$\sim 10^{-2}$	5.6 ~ 12.4	Cylinder, fused quartz	Vacuum and He
15B	0.14	5 × 5	3×10^4 at 10.5 KeV	Channel cut fixed exit channel cut Double crystal	7×10^{-4} 7×10^{-4} 1.5×10^{-3}	10.0 - 34.0 3.5 - 16.0	none	Vacuum
15C	2	60 × 6	White			4 ~ 35	none	Vacuum

4 Characteristics of Soft X-ray and VUV beam lines and optics

BRANCH BEAM LINES	Monochromator	Grating (Crystal)	Groove density ($\text{\AA}/\text{mm}$)	Blaze (\AA)	Resolution	Wavelength range (\AA)
B1-A	Grating/Crystal Monochromator	Au-coated original InSb(111) Si(111)	2400		$E/\Delta E \sim 2000$	2 ~ 2000
B1-B	Filtered white					
B1-C	Filtered white					
B2-A	White/2m grazing incidence (85°)	Hitachi Au-coated replica	2400	30	$\Delta\lambda=0.02 \text{ \AA}$ for $10\mu-10\mu$ slits	30 ~ 200
B2-B	Channel-cut double crystal	Beryl($10\bar{1}0$) InSb(111)	2d=15.9 \AA 2d=7.4806 \AA	—		8 ~ 16 3 ~ 8
B11-A (2GH)	Grasshopper Mark VII 2m grazing incidence Fixed incidence angle of 88°	Hitachi Au-coated replica (pyrex)	2400 1200	16.6 33.3	$\Delta\lambda=0.02 \text{ \AA}$ $\Delta\lambda=0.04 \text{ \AA}$ for $10\mu-10\mu$ slits	10 ~ 145 10 ~ 290
B11-B (DXM)	Jumbo Jr. Double crystal monochromator	Ge(111) InSb(111) Beryl($10\bar{1}0$)	2d=6.53 \AA 2d=7.4806 \AA 2d=15.9 \AA		$\Delta E=1\text{eV}$ at 2KeV $\Delta E=0.8\text{eV}$ at 2KeV $\Delta E=0.6\text{eV}$ at 1KeV	2.7 ~ 6.2 3 ~ 7 8 ~ 16
B11-C (SSN)	1m Seya-Namioka Constant deviation of 70°	B & L Au-coated replica	2400 1200	694 1300	$\lambda/\Delta\lambda=2000$ ~ 3000	400 ~ 1700 400 ~ 3500
B11-D (CDM)	2m grazing incidence constant deviation monochromator $\alpha + \beta = 154^\circ$	B & L Au-coated replica	2400 1200 600	32 116 460	$\lambda/\Delta\lambda \sim 1700$ for $25\mu-25\mu$ slits	80 ~ 150 120 ~ 300 240 ~ 600
B12-A (GSN)	1m Seya-Namioka Constant deviation of 70°	B & L Au-coated replica	2400 1200	508 536	$\Delta\lambda=0.4 \text{ \AA}$ at 500 \AA for $100\mu-100\mu$ slits	350 ~ 1000 350 ~ 2000
B12-B (6VOPE)	6.65m normal incidence off-plane Eagle mounting	B & L Pt-Coated replica B & L Os-coated replica Hyperfine Os-coated replica	1200 1200 4800	1500 5500 900	$\Delta\lambda=0.003 \text{ \AA}$ at 500 \AA for 11th order	400 ~ 2500
B12-C (10GIM)	10m grazing incidence Fixed incidence angle of 89°	Hitachi Au-coated replica (pyrex)	2400 1200	9.5 10.9	$\Delta\lambda=0.002 \text{ \AA}$ $\Delta\lambda=0.004 \text{ \AA}$ for $5\mu-5\mu$ slits	6 ~ 25 6 ~ 50

4 Characteristics of Soft X-ray and VUV beam lines and optics

(continued)

(PRE - MIRRORS)

BRANCE BEAM LINES	Type	Radius of curvature (mm)	Angle of incidence	Material	Coating Material	Dimensions (mm)	Horizontal & Vertical acceptance (mrad)
B1-A	Parabol- oidal		89°	Fused Quartz			4.0 ^h ×1.0 ^v
B1-B	Plane		88° ~ 89°	SiC			1.2 ^h ×4.0 ^v
B1-C	Toroidal		86°	Fused Quartz	Pt		2.0 ^h ×4.0 ^v
B2-A	Plane	—	88°	SiC	Pt	120 ^l ×60 ^w ×15 ^t	—
B2-B	—	—	—	—	—	—	—
B11-A (2GH)	Spherical	360000	88°	Fused Quartz	Pt	400 ^l ×170 ^w ×40 ^t	1.3 ^h ×0.4 ^v
	Spherical	28000	88°	Fused Quartz	Au	300 ^l	
B11-B (DXM)	Bending Cylinder	ρ=300 R~950000	89°	Fused Quartz	Pt	580 ^l ×140 ^w ×30 ^t	4.0 ^h ×0.6 ^v
B11-C (SSN)	Plane Concave	— 5600	77.5° 42.5°	SiC Fused Quartz	none Pt	250 ^l ×100 ^w ×40 ^t 100 ^l ×100 ^l ×20 ^t	4.8 ^h ×3.0 ^v
B11-D (CDM)	Cylindrical Plane Concave	ρ=750 — 4000	86° 86° 86°	SiC Fused Quartz BK-7	Pt Au Au	400 ^l ×60 ^w ×40 ^t 50 ^l ×40 ^w ×10 ^t 50 ^l ×40 ^w ×10 ^t	2.0 ^h ×2.0 ^v
B12-A (GSN)	Cylindrical Concave	ρ=1850 6250	80° 45°	SiC Fused Quartz	none Pt	250 ^l ×200 ^w ×40 ^t 100 ^l ×20 ^t	2.4 ^h ×1.5 ^v
B12-B (6VOPE)	Plane Concave* Concave*	— 4321 2188.5	80° 35° 45°	SiC Pyrex Pyrex	none Pt Pt	280 ^l ×100 ^w ×40 ^t 110 ^l ×20 ^t 110 ^l ×20 ^t	5.0 ^h ×3.6 ^v
B12-C (10GIM)	Plane Concave Concave	— 8903 7527	86.85°~88.83° 89° 89°	SiC Pyrex Pyrex	Pt Pt Pt	120 ^l ×60 ^w ×15 ^t 90 ^l ×15 ^t 90 ^l ×15 ^t	0.14 ^h ×0.4 ^v

4 Characteristics of Soft X-ray and VUV beam lines and optics

(continued)

(REFOCUSING MIRRORS)

BRANCE BEAM LINES	Type	Radius of curvature (mm)	Angle of incidence	Material	Coating Material	Dimensions (mm)	Beam Size (mm)
B1-A	Parabol- oidal		89°	Fuzed Quartz			
B1-B						19 mm ϕ	
B1-C						2 ^h ×10 ^v	
B2-A							
B2-B							
B11-A (2GH)	Benting Cylinder	R \sim 3000	89°	Pyrex	Pt	220 ^l ×24 ^w ×6 ^t	8 ^h ×0.3 ^v
B11-B (DXM)							8 ^h ×1 ^v
B11-C (SSN)	Toroidal	ρ =2000 R=125	72.5°	Pyrex	Au	90 ^l ×50 ^w ×10 ^t	\sim 1 ϕ
B11-D (CDM)	Toroidal	ρ =400 R=3100	77°	BK-7	Au	60 ^l ×40 ^w ×10 ^t	0.5 ^h ×0.5 ^v
B12-A (GSM)	Plane Toroidal Plane	— ρ =340 R=2000 —	80° 70° 80°	Pyrex Pyrex Pyrex	Pt Pt Pt	40 ^l ×40 ^w ×10 ^t 40 ^l ×40 ^w ×10 ^t 40 ^l ×40 ^w ×10 ^t	\sim 1 ϕ
B12-B (6VOPE)							
B12-C (10GIM)							

5 List of Apparatuses

Format

Name of apparatus

1. General characteristics
 2. Accessories
 3. Other features
 4. Typical Experiment in Act. Rept. 84/85
 5. Station used
 6. Responsibility
 7. Pages in (A) "Act. Rept. 82/83" and (B) "Act. Rept. 83/84" describing the details
- (a) Multi-purpose chamber for gas phase experiments
1. Ultimate pressure 1×10^{-7} Torr. Equipped with two turn tables notatable the incident light.
 2. Double-ion chamber.
 - 3.
 4. The measurements of absolute photoabsorption cross sections of C_3H_6 and C_4H_8 isomers.
 5. BL-12A
 6. A. Yagishita
 7. V-40 in (A)
- (b) Time-of flight spectrometer for photoion measurements
1. Ultimate pressure 5×10^{-8} Torr. Electrostatic lenses satisfying the conditions of single-field space focusing for threshold electrons and double-field space focusing for ions.
 2. Furnace to evaporate alkali-and alkaliearth-metals.
 - 3.
 4. The measurements of single-and double-photoionization cross sections of Ca and Sr.
 5. BL-12A
 6. A. Yagishita
 7. V-40 in (A)
- (c) Heat-pipe chamber for photoabsorption measurements of free-metal atoms
1. Ultimate pressure 1×10^{-7} Torr. The pressure difference between vapor column and differential pumping stage is $\sim 10^7$.
 2. Buffer gas inlet system.
 3. Heated up to about $1000^\circ C$.
 4. The measurements of photoabsorption cross sections for 3d electrons of Xe, Cs, and Ba.
 5. BL-11A.
 6. K. Ito
 7. V-41 in (A)
- (d) Gas phase angle resolved photoelectron spectrometer
1. Ultimate pressure 5×10^{-8} Torr. Equipped with a conventional hemispherical electrostatic analyzer and with a position-sensitive parallel-plate electrostatic analyzer.
 2. Sample-gas inlet system.
 3. A sample gas is confined in a gas cell.
 4. The measurements of absolute intensity and polarization of synchrotron radiation from the undulator.
 5. BL-2, BL-12A.
6. A. Yagishita
7. V-42 in (A)
- (e) VUV and Soft X-ray Reflectometer
1. Equipped with a goniometer, insuring accurate incidence angle (30 sec) Up to 89.4° incidence angle Ease of optical alignment Ease of sample exchange High vacuum (2×10^{-9} Torr)
 - 2.
 3. Equipped with ports for vacuum evaporation.
 4. Optical constants of mirror materials. Surface roughness.
 5. BL-11A
 6. T. Miyahara
 7. V-41, VI-78 in (A)
- (f) UHV experimental chamber for absorption measurements I.
1. Ultra-high vacuum (1×10^{-10} Torr) Equipped with an electron-beam gun for evaporation of samples. Equipped with a quartz oscillator capable of being cooled to LNT.
 2. Sample holder with an adjustable linear motion, capable of being cooled to LNT.
 3. Designed mainly for very reactive metal samples.
 4. Absorption measurement of alkali metals, alkali metal alloys, and rare earth metals. VI-114
 5. BL-11C, BL-11D.
 6. T. Miyahara
 7. VI-82 in (A)
- (g) UHV experimental chamber for absorption measurements II.
1. High vacuum (1×10^{-9} Torr) Mounts up to 5 samples.
 2. Gas cell (160 mm in length) Vacuum evaporater Electron multiplier (R595).
 3. 190 mm I.D.
 4. Core level absorption in alkali halides and transition metal compounds. M4,5 giant resonance absorption in $Z = 49-57$ elements. Photoefficiency of photocathodes. Lithography for resist polymer.
 5. BL-11A, BL-12C.
 6. H. Maezawa
 7. V-40, VI-73, VI-74, VI-76, VI-77, VI-79 in (A)
- (h) Vacuum chamber for performance testing of grating monochromator
1. Equipped a 160 mm length gas cell with 10 mm diameter propylene windows.
 2. A sample-gas inlet system.
 - 3.
 - 4.
 5. BL-11A, BL-12C.
 6. H. Maezawa
 7. V-40 in (A)
- (i) Focusing Weissenberg camera with multi-layer-linescreens
1. Useful for high resolution macromolecular crystallography. High signal-noise ratio. Equipped with multi-layer-line screens.

2. Cooling unit by N₂ gas.
 3. Wide range of ψ -axis rotation.
Wide 2 θ range.
 4. X-ray structure determination of macromolecular crystal (insulin, actin-DNase I complex, Plasminostreptin etc.)
 5. BL-4B, BL-4A,
 6. Y. Sakabe
 7. VI-5 in (A)
- (j) X-ray Diffractometer for gasses.
1. Equipped with horizontal ω -2 θ two-circle goniometer.
X- ϕ circle motion available.
 2. Gas cell with boiling system.
Gas cell for pressure tight experiments.
Incident beam monitor with SSD.
 3. Uses white beam for energy-dispersive method. Uses monochromatic beam for angle-dispersive method.
 4. Angle-dispersive X-ray diffraction and Compton scattering study of carbon dioxide.
 5. BL-15C, 14C.
 6. T. Mitsuhashi
 7. VI-172 in (B)
- (k) X-ray diffractometer for liquids and melts.
1. Collects intensity-data for radial distribution analysis for non-crystalline materials such as gases, liquids, melts and glasses.
 2. θ -2 θ goniometer with monochromator and analyzer.
Single-crystal monochromator with quartz and β -alumina.
Double crystal monochromator with Si(111).
Keramax furnace
 - 3.
 4. Energy-dispersive study of gas and liquid.
Angle-dispersive study of liquids, melts and powder crystals.
 5. BL-4B.
 6. K. Ohsumi
 7. V-24 in (A)
- (l) Multi anvil high pressure X-ray system.
1. Maximum pressure 13 GPa.
Maximum temperature 1700°C.
Sample volume (typical) 2 mm ϕ \times 3 mm ℓ .
Uses white X-ray.
 2. Two axis goniometer
Handy type SSD.
 3. Best quality in the world for this research field.
 4. Compressibility of Au at room and high temperatures.
Time resolved observation of Bl-B2 transition of BaS.
 5. BL-4C.
 6. K. Ohsumi
 - 7.
- (m) EXAFS Spectrometer
1. Dedicated to X-ray absorption spectroscopy.
High-resolution.
High-quality beam.
 2. Control system with a microcomputer (SORD M-223).
Closed cycle refrigerator.
Reaction chamber for catalyst.
 - 3.
4. EXAFS of catalysts
VI-58, VI-64, VI-71, VI-76,
VI-78, VI-97, VI-100, VI-101
 5. BL10B.
 6. M. Nomura
 7. V-8 in (A)
- (n) Small angle X-ray scattering equipment for solutions (SAXES)
1. Dedicated to small-angle scattering for solutions, synthetic polymers.
 2. Stopped flow apparatus.
Temperature jump apparatus.
Flash light for specimen.
 3. Uses monochromatic beam from the optics installed at BL-10C.
 4. Measurements for Bovine Serum Albumin, Lysozyme, Tobacco Mosaic Virus, Purple Membrane etc.
 5. BL-10C.
 6. Y. Amemiya
 7. V-29 in (A)
- (o) Ultra-high vacuum X-ray diffractometer
1. Ultra-high vacuum with cryo-pumping system.
Equipped with X-ray diffractometer and LEED optics.
 2. Super precision goniometer using elastic torsion mechanism.
Microcomputer control system.
NaI scintillation counter system and SSD.
 - 3.
 4. Study on Si(7 \times 7) structure.
 5. BL-10C, BL-14B.
 6. T. Ohta
 7. V-34 in (A)
- (p) Vertical-type four-circle diffractometer.
1. Used for crystallographic studies and scattering experiments.
Large X-circle (280 mm ϕ).
 2. Control system with MELCOM 70/30.
High-temperature furnace.
X-rays film cassette.
 - 3.
 4. Study on anomalous scattering effect.
 5. BL-10A.
 6. S. Sasaki
 7. V-27 in (A)
- (q) Horizontal-type four circle diffractometer.
1. Specially built, but having a conventional diffractometer configuration.
Fully computer-controlled for rapid, tunable and precise diffraction data collection.
 2. Computer-controlled alignment carriage with 5 stepping motor driven axes, on which the diffractometer is mounted.
Huber Precession/Rotation camera.
MELCOM 70/60 minicomputer with OPTRONICS film scanner.
 3. Mechanical control interfaced through IEEE-488 bus.
CAMAC and NIM measuring system.
 4. Crystal structure analysis of antibiotics, biotic metabolitos, proteins etc.
VI-145, VI-146, VI-127
 5. BL-14A.
 6. Y. Satow
 7. V-30 in (A)

- (r) Three-axes X-ray Diffractometer.
1. Equipped with three precision goniometers (Huber 410, 420, and 440).
 2. Scintillation counter. SSD with MCA. Asymmetry cut plane monochromator.
 3. Having precision of 0.36 arc sec per pulse.
 4. Phase-contrast microscopy. Development of application to medical diagnosis. VI-185
 5. BL-14C2, BL-15B1.
 6. H. Kawata
 7. V-32, V1-97, V1-98 in (A)
- (s) Time-Resolved X-ray measurement system with 1D-PSD.
1. Time resolution up to 1 msec. Either 256ch. \times 191 frames, 512 ch. \times 95 frames, or 1024 ch. \times 47 frames. Fast data acquisition up to 1 MHz.
 2. LSI 11/23 computer. CAMAC modules (Time to Digital Converter, Histogramming Memory etc.).
 3. Uses monochromatic X-ray ($\lambda=1.5\text{\AA}$).
 4. Measurements on frog skeletal muscle, purple membrane, Ribosome, etc. VI-147, VI-162, VI-158, VI-170
 5. BL-15A1, BL-10C.
 6. Y. Amemiya
 7. V-35 in (A)
- (t) X-ray irradiation equipment
1. Assembly of a circular table (Huber 410) with a channel-cut monochromator, slits and irradiation chamber.
 2. Ionization chamber for X-ray monitoring.
 3. Controls suitable biological atmosphere for samples. Wide beam acceptance (4 mmV \times 30 mmH).
 4. Biological effects of inner shell ionization on bromine-incorporated cells.
 5. BL-4C, 15-B1.
 6. Y. Satow
 7. V1-30, V1-32, V1-33 in (A)
- (u) High-speed X-ray topography Camera.
1. Equipped with two X-ray TV cameras. Maximum load of 30 kg on sample goniometer. Facilitates simultaneous observation of two different Laue spots.
 2. Microcomputer system (AIDACS-3000). Image processor TF4110. Work shutter for variable exposure time (0.1 \sim 9.9sec).
 3. 1 arc sec accuracy of θ -rotation. Ample space around the specimen position.
 4. Melting process of GaAs. Magnetization process of Fe-3% Si, etc. VI-180, VI-182, VI-183
 5. BL-15B, BL-14C.
 6. H. Kawata
 7. V-31 in (A)
- (v) Precision X-ray optics.
1. Goniometer assembly dedicated to precision diffraction study such as double-, triple-, and more than triple-crystal diffractometry and topography.
2. Microcomputer control system. NaI scintillation detector system. SSD and MCA. Ionization chamber for monitoring. Room temperature controller. Experimental table with air springs
 3. 1 arc sec accuracy for full rotation. 0.1 arc sec accuracy within 6 $^\circ$ using tangential bar system. Employs super-precision rotation mechanism with elastic torsion and PZT.
 4. Detection of polarization rotation under magnetic diffraction condition. Structure analysis of epitaxial layer/substrate interfaces with standing wave method. VI-188, VI-189
 5. BL-15C.
 6. T. Ishikawa
 7. V-33 in (A)
- (w) Low temperature X-ray diffractometer
1. Equipped with a three-axis goniometer ($\psi, 2\theta, \chi$) mainly used for low temperature (~ 0.3 K) X-ray diffraction.
 2. Some types of refrigerators and magnets.
 3. Available addendum limited to 500 kg in weight.
 4. Peiels transition in $K_0.3MoO_3$
 5. BL-4C, BL-10C
 6. T. Nakajima
 7. V-25 in (A)
- (x) Apparatus for ARPES experiment for solid state
1. Base pressure 5×10^{-11} Torr Equipped with a double-pass cylindrical mirror analyzer and with a hemispherical analyzer mounted on a two axis rotation mechanism
 2. Some equipments for sample preparation and characterization Sample bank and transfer system Sample gas inlet system
 - 3.
 4. Mainly for angle-resolved photoelectron spectroscopy (ARPES) of single crystals VI-133, VI-135, VI-136
 5. BL-11D
 6. T. Miyahara
 - 7.
- (y) X-ray fluorescence spectrometer
1. Energy dispersive type spectrometer Equipped with a Si(Li) detector Elemental analysis with very high sensitivity.
 2. X-Z scanning sample stage. Flat mirror and multilayer for wide bandpass monochromator.
 - 3.
 4. VI-24, VI-29
 5. BL-4A
 6. A. Iida
 7. V-23 in (A)

**PHOTON FACTORY
ACTIVITY REPORT**

1984/85

PHOTON FACTORY ACTIVITY REPORT 1984/85

#3

#3



NATIONAL LABORATORY FOR HIGH ENERGY PHYSICS, KEK